Investigation of electrical contact resistances in graphene-based devices by Kelvin Probe Force Microscopy

Von der Fakultät für Ingenieurwissenschaften,
Abteilung Elektrotechnik und Informationstechnik

der

Universität Duisburg-Essen

zur Erlangung des akademischen Grades
Doktors der Naturwissenschaften
genehmigte Dissertation

Von

M.Sc. Carlos Alvarado Chavarin
aus Mexicali, Mexiko

1. Gutachter: Prof. Dr. rer. nat. Gerd Bacher
2. Gutachter: Prof. Dr. rer. nat. Thomas Schröder
Tag der mündlichen Prüfung: 10.03.2017

Abstract

Graphene is a carbon atom-thick layer with outstanding mechanical and electrical properties. It has been envisioned as a promising candidate for its use as a conductive medium in polymers, a flexible, transparent and highly conductive electrode in optoelectronic devices and as the conductive channel of high frequency transistors. In the pathway to use graphene and its exceptional properties in such applications there are still open questions to be answered. One key issue always present for the fabrication of devices is that of the electrical contacting of the conductive channel. Such is the case for graphene where it is still not clarified how the oxygen content in Functionalized Graphene Sheets (FGS), the lithography process or the contact design in graphene produced by Chemical Vapor Deposition (CVD) impact the contact resistance between the metal electrode and the graphene channel. This understanding is however of utmost importance since contact resistances significantly affect the conductivity of electronic devices.

Hence, the aim of this work is the characterization of electrical contacts in graphene-based devices on ambient conditions. For a better understanding of the electrical contacts, information on the submicrometer scale is advantageous, therefore Kelvin Probe Force Microscopy (KPFM) was used as the main characterization technique. Since an improvement is expected in the resolution of KPFM by detecting the force gradient instead of the electrostatic force itself, phase modulation is implemented in the existing system and its performance is examined. A feature of less than 20 nm and 80 mV in surface potential variation could be clearly resolved in ambient conditions. In the following section, it is shown that with decreasing oxygen content in FGS, the transport mechanism of the charge carriers has a transition from predominantly hopping to predominantly diffusive transport, along with a reduction of the sheet resistance from > 400 k$\Omega/\square$ to < 10 k$\Omega/\square$. At the same time it is reported that the contact resistance changes from nonlinear, Schottky-type behavior with high resistance (> 100 k$\Omega\mu$m) to linear, ohmic behavior with low contact resistance (~ 1 k$\Omega\mu$m). In the last part of this work, the influence of the fabrication process and contact design in the contact resistance of CVD graphene is investigated. It is determined that optical lithography systematically produced devices with contact resistances up to an order magnitude larger ($\gg 1$ k$\Omega\mu$m) than e-beam lithography (< 1 k$\Omega\mu$m). It is determined that this is caused by a $3-4$ nm thick residual layer from the optical lithography process which is present between graphene and the metal electrode. An elegant solution to prevent the effect of this residual layer in contact resistance is the use of novel one dimensional contacts instead of the conventional two dimensional contacts. In the former type of contact the charge carriers transit the metal/graphene interface not vertically but horizontally. It can be shown that such novel type of contact design, even with the use of optical lithography, can reach contact resistances lower than 200 $\Omega\mu$m.

Zusammenfassung

Graphen, ein monolagiges Kohlenstoffallotrop, besitzt herausragende mechanische und elektrische Eigenschaften. Derzeit wird es u.a. als ein aussichtsreicher Kandidat für den Einsatz als leitfähiges Medium in Polymeren, als flexible, transparente und elektrisch hoch leitfähige Elektrode in optoelektronischen Bauelementen und als Kanalmaterial in Hochfrequenztransistoren gehandelt. Bis zur kommerziellen Nutzung in diesen Anwendungsbereichen müssen jedoch noch grundlegende Fragen geklärt werden. Eine zentrale Fragestellung, die immer auftaucht, sobald reale Bauelemente hergestellt werden sollen, ist die der elektrischen Kontaktierung. So ist im Fall des Graphens immer noch nicht geklärt, wie sich der unterschiedliche Sauerstoffgehalt in funktionalisierten Graphenflocken (Functionalized Graphene Sheets, FGS) und das Lithographieverfahren oder das Kontaktdesign von Graphen hergestellt mittels chemischer Gasphasenabscheidung (CVD) auf den elektrischen Kontaktwiderstand zwischen Metallelektrode und Graphen auswirken. Ein Verständnis ist jedoch von fundamentaler Bedeutung, da Kontaktwiderstände die Leistungsfähigkeit elektronischer Bauelemente erheblich beeinflussen.

Der Fokus dieser Arbeit richtet sich auf die Charakterisierung von elektrischen Kontakten in Graphen-basierten Bauelementen unter Umgebungsbedingungen. Da es für das Verständnis elektrischer Kontakte unabdingbar ist, Informationen im Submikrometerbereich zu erhalten, wurde die Charakterisierung mittels der Kelvin Probe Force Microscopy (KPFM) Technik durchgeführt. Da die Ortsauflösung eines Rasterkraftmikroskops durch die Messung des Kraftgradienten anstelle der direkten Kraftmessung erheblich verbessert werden kann, wurde die Technik der Phasenmodulation in das bestehende System implementiert und auf seine Leistungsfähigkeit hin untersucht. Es konnte eine Ortsauflösung von weniger als 20 nm und eine Potenzialauflösung von 80 mV unter Umgebungsbedingungen demonstriert werden. Im folgenden Teil der Arbeit konnte gezeigt werden, dass sich mit abnehmendem Sauerstoffgehalt in FGS der Leitungsmechanismus der Ladungsträger von überwiegend Hopping-Transport zu überwiegend diffusivem Ladungstransport verändert, begleitet von einer Reduzierung des elektrischen Schichtwiderstands von > 400 k$\Omega/\square$ auf < 10 k$\Omega/\square$. Gleichzeitig wurde nachgewiesen, dass sich der Kontaktwiderstand von nichtlinearem, Schottky-ähnlichem Verhalten mit hohen Kontaktwiderständen (> 100 k$\Omega\mu$m) zu linearem, ohmschem Verhalten mit niedrigeren Kontaktwiderständen (~ 1 k$\Omega\mu$m) verändert hat. Im letzten Teil der Arbeit wurde der Einfluss des Lithographieverfahrens und des Kontaktdesigns auf die Kontaktwiderstände bei CVD Graphen untersucht. Es zeigte sich, dass das optische Lithographieverfahren systematisch Bauelemente mit elektrischen Kontaktwiderständen produziert, die um eine Größenordnung ($\gg 1$ k$\Omega\mu$m) gegenüber denjenigen beim Elektronenstrahl-Lithographieverfahren (< 1 k$\Omega\mu$m) erhöht sind. Als Grund dafür konnte eine Residuenschicht von Photolack der Dicke 3 – 4 nm zwischen Graphen und Metallelektrode ermittelt werden. Eine elegante Methode, diese Residuenschicht zu verhindern, stellt der Übergang von konventionellen, zweidimensionalen elektrischen Kontakten zu neuartigen, eindimensionalen Kontakten dar. Bei Letzteren findet der Ladungsträgerübergang vom Metall ins Graphen nicht senkrecht zur Graphenschicht statt, sondern lateral. Es konnte gezeigt werden, dass durch solche neuartigen Kontaktdesigns selbst unter Verwendung der optischen Lithographie Kontaktwiderstände von weniger als 200 $\Omega\mu$m realisierbar sind.

Contents

Chapter 1

Introduction

With an ever growing demand of faster and more powerful cutting edge technologies for consumer electronic applications, conventional semiconductor materials are being pushed towards the borders of their physical limitations. Therefore, to continue the improvement of electronic devices and their applications, new paths must be studied, which can take the form of new and/or improved materials with outstanding properties. In 2004 scientists at Manchester University published a paper on the finding of such a new and outstanding material: graphene [1].

Graphene, is defined as a single layer of sp^2 bonded carbon atoms arranged in a hexagonal structure. Thus, this atom-thick layer is considered to have only 2 dimensions (2D). The first paradigm that graphene changed was the fact that a 2D structure can indeed exist, either suspended or supported on a substrate [2], since theoretical calculations had shown that obtaining graphene was thermodynamically not feasible [3] [4]. The 2004 paper reported that graphene′s electrical conductivity could be controlled by a perpendicular electric field which could induce charge carrier concentrations up to 10^{13} cm^{-2} with mobilities up to 10^4 cm$^2V^{-1}$s^{-1}[1]. The following year, the same team observed in graphene the anomalous quantum Hall effect, which was the evidence that electrons in graphene behave as massless Dirac Fermions [5]. Along with other properties such as ballistic transport at room temperature [6], graphene has placed itself as a competitor against established semiconductor technologies [7]. This has caused a knowledge-rush in the scientific community which the industry has followed with names such as IBM, Samsung, BASF, among others exploring different applications of graphene. For example, electronic displays mainly use Indium Tin Oxide which is a scarce and brittle material, graphene on the other hand is abundant (carbon), transparent and flexible. This

positions graphene as a competitor for its use in ordinary displays and state-of-the-art flexible displays [8] [9].

On the road to implement the above mentioned properties of graphene in off-the-shelf products, as with any other material, the establishment of low cost and large scale fabrication processes for the whole chain is needed, from raw materials to finished products. The graphene studies began with an artisanal mechanical exfoliation from graphite [1], which cannot be applied for mass production. Therefore, other means to synthesize graphene have been studied to obtain larger yields without losing the exceptional properties of this material. For this purpose, two chemical approaches have excelled in large scale production at low cost relative to other synthesis processes, namely thermochemical exfoliation of graphite [10] and carbon deposition on catalytic surfaces [11]. Once the material is available, the fabrication of graphene-based devices follows. Micrometer and nanometer devices can be fabricated by electron beam (e-beam) lithography or optical lithography [1]. Again keeping the industrial implementation in mind, the manufacturing process requires a high output production rate. Therefore, optical lithography is rather desired in industry and efforts must be made to effectively produce devices by this method. Inevitably, the operation of graphene in electronic and optoelectronic applications requires the use of electric contacts, mostly in the form of metal/graphene interfaces, to inject and extract the charge carriers from and into graphene. The most widely used methods for the electrical characterization of devices and their electrical contacts are macroscopic approaches. However, for graphene, information on the nanometer scale is very valuable for the overall understanding of this extremely thin and relative new material. As a 2D material, graphene can be considered mostly a surface. Therefore, Kelvin Probe Force Microscopy (KPFM), stands as a suitable option since it is a surface potential sensitive technique, which is based in the Atomic Force Microscopy (AFM), therefore sharing the intrinsic high spatial resolution, down to the nanoscale.

The characterization of graphene-based micro- and nanodevices could then benefit from the use of KPFM as an electrical characterization technique to deeply understand the behavior of graphene synthesized by large-scale approaches. Thus, this thesis is devoted to the electrical characterization with high spatial resolution by means of KPFM on graphene-based devices and their metal/graphene interfaces.

KPFM is an established technique at the Duisburg-Essen University's *Werkstoffe der Elektroteknik* (WET) workgroup, where these investigations were made. Here the

method is based on measuring the electrostatic force between the sample and a nanometer metallic tip. It has been reported [12], however, that the sensitivity of KPFM can be enhanced instead by measuring the rate of change of this electrostatic force i.e. the force gradient. The use of the force gradient is usually reserved for vacuum conditions where the frequency shifts are directly accessible, however, in ambient conditions, phase shifts could approximate the electrostatic force gradients, thus allowing an improvement in the current operation conditions. Hence, it is yet to be validated if the phase shifts can be implemented for the detection of the force gradient and operation of single pass KPFM in our system and whether this in fact provides an improvement in the technique. Subsequently, the results of this non-conventional technique must be compared to other established characterization methods to analyze operating devices.

One of the graphene types on which this research is focused [10], is synthesized by the oxidation of graphite and exfoliation of its (graphene) layers with a simultaneous and/or posterior thermal reduction step of the product. This process causes a functionalization of the graphene structure with oxygen species, thus referred as Functionalized Graphene Sheets (FGS). The controlled ratio of carbon to oxygen atoms in the structure can tailor the electronic properties of the materials in a broad spectrum [13]. In literature, it is proposed that the charge transport regime of the electric current in FGS devices is in function of the carbon to oxygen ratio [14]. Despite the importance of the electrical contacts on devices, the impact that this ratio and transport regime transition could have on them has not yet been studied. Thus, the influence that the carbon to oxygen ratio can have on the resistance of electric contacts and channel must be separated. This can be achieved by studying the submicrometer FGS devices with the high spatial resolution of KPFM.

The second type of graphene investigated in this work is grown on the surface of copper where carbon atoms are soluble, by Chemical Vapor Deposition (CVD) [11]. Contrary to mechanically exfoliated graphene, CVD graphene has mass production potential and has been used with outstanding results in high frequency applications [15]. However, preliminary results show that devices fabricated by optical lithography have a lower performance compared to those fabricated by e-beam lithography [16]. This suggests a process-related issue that negatively affects the operation of the electrical contacts, where investigations have not yet clarified whether this is an intrinsic change of graphene and/or the spatial coverage and homogeneity of this process-related issue. Related to this, the contact design can also impact the performance of devices.

Investigations have shown that novel contact designs can positively influence the overall performance of graphene-based devices [17]. Nevertheless, the processes reported up until now to obtain such contact architectures are laborious and hard to implement on a large scale. Colleagues from *AMO* GmbH have recently produced operating graphene devices with such novel contacts through a small modification of an already established optical lithography process. Whether such a procedure and contact design can actually improve the performance of ordinary optical lithography devices is still to be confirmed. Therefore, with the perspective of improving graphene-based electronic applications towards industry-friendly processes, the fabrication procedure and contact design influence are investigated in this work as well.
This thesis report is organized as follows,

- **Chapter 2** deals with the basic information and physics of graphene. It includes definition, structure and properties of pristine graphene. It is then followed by the definition for the different nomenclature used in literature, types of graphene and a brief description of their synthesis methods. Afterwards, the preparation and fabrication of operating devices from the two types of graphene analyzed in this work is described.

- **Chapter 3** presents and describes the main characterization techniques, AFM and KPFM. Their mathematical models, physics and operation modes are discussed, along with the experimental equipment used. Auxiliary techniques used in this research such as Raman spectroscopy and established macroscopic electrical characterization such as Transmission Line Method (TLM) and 4-point (4p) probe measurements are presented and described as well.

- **Chapter 4** reviews the working principle and presents the technical implementation required to increase the sensitivity of KPFM by the detection of the electrostatic force gradient. The cabling, signals and working parameters are presented and the relevance of the grounding for the interpretation of the results is discussed. The achievable resolution of phase modulation (PM) KPFM and a comparison of force against force gradient detection for the analysis of operational devices is reported. The chapter ends with the comparison of results of KPFM against those of standard macroscopic 4p probe to ascertain the reliability of the technique.

- **Chapter 5** reports the electrical characterization, by means of KPFM, of individual submicrometer FGS with different carbon to oxygen ratios. First, the geometries

and AFM height profiles are presented for representative samples, followed by the surface potential distribution map of the FGS devices with and without voltage applied. At the end of this chapter, the current-voltage characteristics, KPFM voltage drop analysis and results of the calculations are presented and discussed for the different types of FGS.

- **Chapter 6** is dedicated to investigating the origins of contact resistance derived from the device production processes and the impact of a novel contact architecture. First, using KPFM voltage drop analysis, the influence of optical lithography and e-beam lithography on the electrical characteristics of graphene devices is assessed. From these results, the investigation deepens in the identification of the source of the process-related influence. Afterwards, the modification used by our partners for the production of a novel contacting scheme to overcome the residual layer caused by optical lithography is described. Finally, the results and findings of the devices produced with this new scheme, analyzed by a combination of TLM and KPFM voltage drop, are reported.

- **Chapter 7** gives a summary of the results obtained in this investigation.

Chapter 2

Background physics

This chapter will review and discuss the physical properties, types and synthesis of graphene. First, graphene′s structure and characteristics will be presented. This includes the lattice cell, electronic band structure, Dirac point, electric field dependence of its carrier density and its non-zero conductivity. The chapter continues with a brief discussion of some technological applications, focusing on the fields of electronics and optoelectronics. The following section clarifies the nomenclature used in literature for the different presentations of graphene and the methods to synthesize this material. The chapter finishes by expanding the information on the two types of graphene investigated in this thesis, namely Functionalized Graphene Sheets (FGS) and Chemical Vapor Deposition (CVD) of graphene on copper. For both types, the process from synthesis to a final operating device will be reviewed.

2.1 Structure and properties of graphene

Carbon can have several allotropes such as diamond or amorphous carbon, where their properties are dictated by the bonding between its components. Among all the different structures, the allotropes based on sp^2 hybridized carbon bonds, such as nanotubes, fullerenes and, for the last decade, graphene have been intensively studied by the scientific community [18]. These structures can find a simple connection which is more commonly known: graphite. Graphite is a 3D structure which is composed of stacked layers of the 2D material graphene. Albeit with changes in the pure sp^2 network, materials with even lower dimensions can be obtained out of graphene structure, such as one-dimensional carbon nanotubes and zero-dimensional fullerenes as seen in Figure 2.1. Thus, as building blocks of other sp^2 bonded carbon materials, the understanding of the graphene structure and properties is fundamental [19].

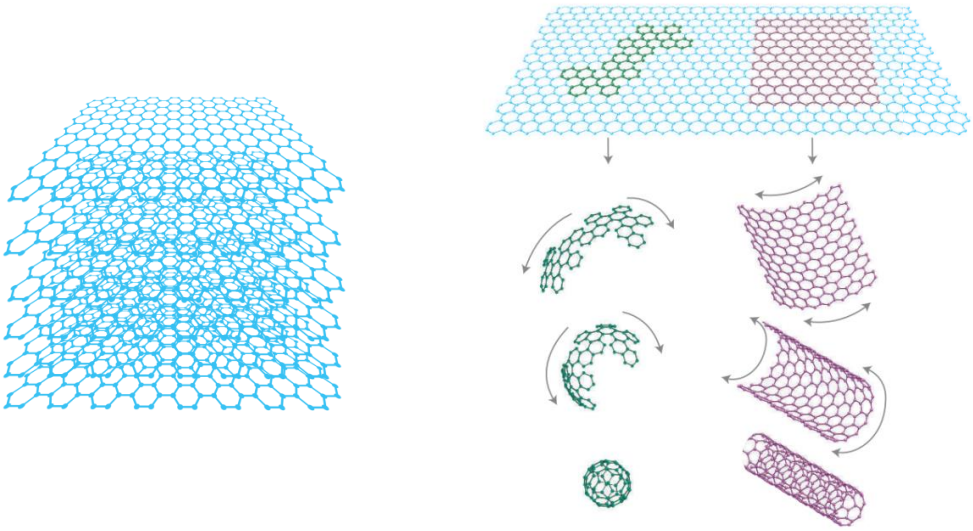

Figure 2.1: Graphite is composed of stacked sheets of graphene with weak interlayer coupling. Using graphene as a starting point, carbon nanotubes can be visualized as a rolled sheet in a cylindrical form or fullerenes in a spherical form. Adapted from [20].

The structure of pristine graphene is a planar repetitive network of six-atom rings of carbon, similar in form to benzene rings [21]. This periodicity can be represented, as any other crystal, by the unit cell which contains the symmetry information needed to repeat the structure indefinitely. The unit cell of graphene consists of two carbon atoms, which can be named A and B. These atoms are differentiated because their positions are not equivalent, i.e. their closest neighbor-atoms do not share the same surroundings. These

two atoms, along with the basis vectors $\hat{a}_1$ and $\hat{a}_2$ define a 2D triangular Bravais lattice with which the whole honeycomb network can be recovered. The basis vectors are defined as

$$\hat{a}_1 = \frac{3a}{2}\hat{i} + \frac{\sqrt{3}a}{2}\hat{j} \tag{2.1}$$

$$\hat{a}_2 = \frac{3a}{2}\hat{i} - \frac{\sqrt{3}a}{2}\hat{j} \tag{2.2}$$

where $\hat{i}$ and $\hat{j}$ are orthogonal unit vectors of the xy-cartesian coordinate system and $a = 0.142$ nm, which is the interatomic separation [22].

These definitions have the objective to calculate and study the behavior of electrons in the electronic band structure of pristine graphene. For that, it is necessary to determine its reciprocal lattice vectors and Brillouin zone. The electrons *sense* the carbon atoms in the graphene structure as a repetitive periodical potential. The behavior of electrons under such conditions can be described by wave vectors in the reciprocal k-space with k_x, k_y coordinates and $\hat{k}_x$, $\hat{k}_y$ unit vectors. The reciprocal vectors $\hat{a}_1^*$ and $\hat{a}_2^*$ are defined in Equation 2.3 and Equation 2.4, respectively. The first Brillouin zone, which are the planes delimiting the energetic borders of graphene′s primary cell, can be calculated using the reciprocal vectors. The reciprocal vectors are

$$\hat{a}_1^* = \frac{2\pi}{3a}\hat{k}_x + \frac{2\pi\sqrt{3}}{3a}\hat{k}_y \tag{2.3}$$

$$\hat{a}_2^* = \frac{2\pi}{3a}\hat{k}_x - \frac{2\pi\sqrt{3}}{3a}\hat{k}_y \tag{2.4}$$

The unit cell, hexagonal structure and vectors of the direct lattice can be seen in Figure 2.2a. In Figure 2.2b, the Brillouin zone in the reciprocal space, which has its center at the gamma point Γ, delimited at the corners by the K and $K^{'}$ points, is shown. This can be seen along with the reciprocal vectors.

The carbon atoms are covalently bonded through their sigma electrons while their pi electrons are the ones responsible for the conductivity of graphene as they can freely move in the lattice [22]. The Brillouin zone, the k-space and tight-binding approximations for the energy dispersion of the pi electrons [19] are used to obtain the general equation

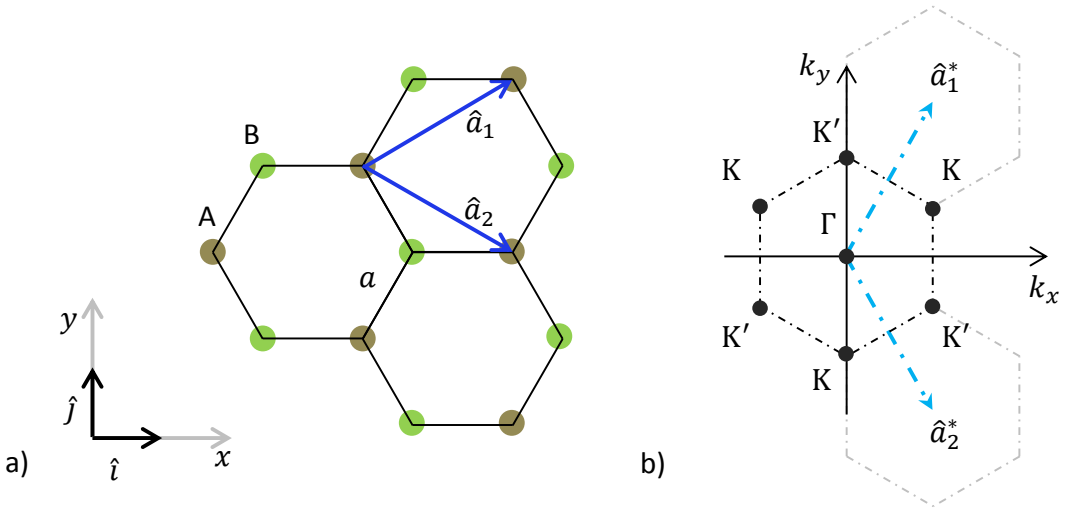

Figure 2.2: (a) Hexagonal ring structure of the carbon atoms in graphene showing its interatomic distance, unit cell and lattice vectors. (b) In the k-space the reciprocal vectors, the first Brillouin zone and the Dirac points at the K and $K^{'}$ points are shown.

for the energies (E_k) in the electronic band structure of graphene as

$$E_k = \pm\gamma\sqrt{3 + 2cos\left(\sqrt{3}k_y a\right) + 4cos\left(\frac{\sqrt{3}}{2}k_y a\right)cos\left(\frac{3}{2}k_x a\right)} \tag{2.5}$$

where γ is the hopping energy between neighbor carbon atoms.

The plus and minus sign of E_k stands for the conduction and valence band respectively, seen in the electronic band structure plot of graphene in Figure 2.3a. Solving the equation close to zero (around K point) results in a symmetric linear relation between both bands, which is represented as [19, 7]

$$E_k = \pm\hbar v_F\sqrt{k_x^2 + k_y^2} \tag{2.6}$$

where $v_F = 3\gamma a/2\hbar \cong 10^6$ m/s, known as the Fermi velocity and $\hbar$ reduced Planck constant.

The linear relation can be seen at the K and $K^{'}$ points known as the Dirac points, visible in the inset of Figure 2.3a with conical shapes facing downwards and upwards, which represent the conduction and valence bands respectively. Thus, the Dirac points show that no electronic band gap exists in graphene, as the bands *touch* each other, which in turn defines this material as a semimetal or a zero-band gap semiconductor. At larger values of E_k the symmetry between the bands is broken and linearity is lost [19].

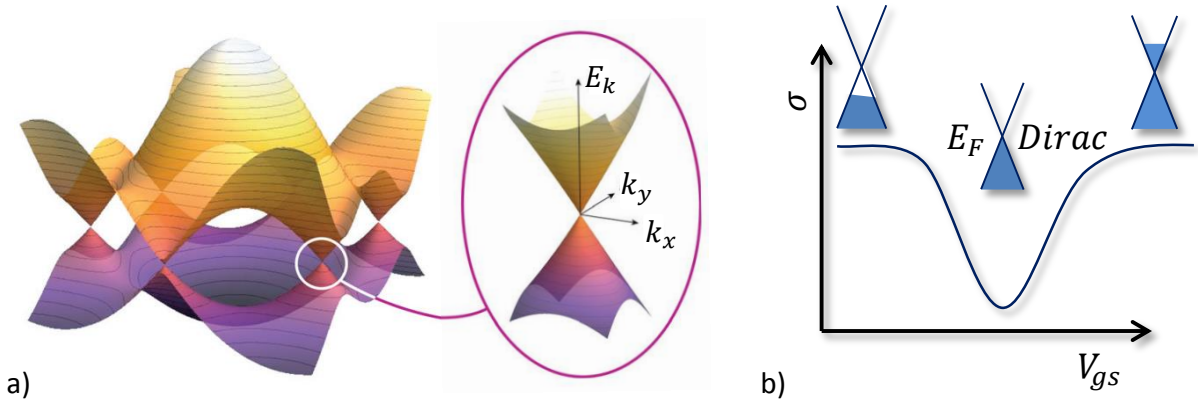

Figure 2.3: (a) Electronic band structure of graphene. Inset: the lower cone represents the valence band and the upper cone the conduction band. Adapted from [23]. (b) The electric field of a gate-source voltage induces doping on graphene which shifts the position of E_F (blue shade). Graphene exhibits a minimum σ as E_F is at the Dirac point.

At temperatures close to zero Kelvin, the carrier density at the Dirac point theoretically should be zero. Nevertheless, in practice graphene exhibits a minimum of electrical conductivity σ (Figure 2.3b) at the Dirac point despite the theoretical predictions [20]. Besides thermal occupation, its origin is thought to be the doping inhomogeneity on its surface [24, 25, 26]. As a zero-band gap semiconductor graphene′s conductivity is defined as

$$\sigma = n\mu e \tag{2.7}$$

where n is the charge carrier density, μ the charge carrier mobility and e the elementary charge.

In graphene, due to the lack of a band gap, the Fermi level (E_F) corresponds to the upmost position where carriers have populated the energy levels underneath. An electric field, normal to the direction of current, such as a gate-source voltage (V_{gs}) adds charge carriers (electrons or holes) to graphene which in turns varies the position of E_F between the valence and conduction bands (Figure 2.3b). Thus, graphene is known to be ambipolar as it can freely work with both carriers [1, 27]. The electric field induced change (ΔE_F) in graphene is defined by Kim et al. [28] as

$$\Delta E_F = sign\left(\Delta V_{gs}\right) \hbar v_F \left(\zeta \pi \left|\Delta V_{gs}\right|\right)^{1/2} \tag{2.8}$$

where ζ corresponds to the substrate gate capacitance in electron charge ($\mathrm{cm}^{-2}\ \mathrm{V}^{-1}$) of the selected dielectric substrate.

Although the control of σ by the electric field effect is the basis of modern electronics, as a result of the lack of a band gap and non-zero carrier density at the Dirac point, the modulation of graphene′s electric current renders low on-to-off current ratios which are not competitive for digital logical applications [29, 15, 30]. However, the intrinsic properties of this material such as its thinness, high current capacity [31] and outstanding charge carrier mobility [32] are promising for analog electronics and optoelectronics technological breakthroughs.

In analog electronics applications, Sire et al. obtained transistors with current gain cutoff frequencies of 2.2 GHz on flexible substrates [33], while in rigid substrates and 350 nm gates, Lin et al. reported 50 GHz [34]. Using graphene transistors Yu-Ming et al. demonstrated a radio frequency mixer operating up to 10 GHz [35]. Wu et al. reported devices with intrinsic cutoff frequencies above 300 GHz for large-scale CVD and SiC grown graphene [36], which theoretically could reach THz frequencies at sub-10 nm gate lengths [37]. Also foreseen in the THz range are bipolar transistors with vertical designs, as Mehr et al. calculated, where graphene works as the base electrode [38].

For optoelectronics Bae et al. used this material as a transparent electrode with values competitive with those of ITO both in transparency and conductivity [39]. Blake et al. demonstrated graphene electrodes in liquid crystal devices [40]. Neumaier et al. obtained a photodetector with data rates up to 50 GBits/sec [41] and recently demonstrated a graphene-based heater for silicon waveguides in photonics [42].

Several challenges need to be overcome before the advantages of graphene′s unique properties can be commercially exploited. Some of these challenges include increasing control and yield of the synthesis and overall cost reductions, as well as contact engineering to reduce the voltage drops at the metal/graphene interfaces within a device [30, 15, 43]. In the next section, the different nomenclature of graphene as well as the main synthesis processes will be discussed.

2.2 Production: Types of graphene

The first production method started in 2004 with the mechanical exfoliation, also known as the micro cleavage or scotch tape technique, where the layers of graphite were separated by a manual repetitive removal of its surface using the adhesive forces of a tape. In the last stages of the exfoliation, due to the thinness of the material, visibility became hard, however, it was overcome by the optical reflection caused on SiO_2/Si substrates (Figure 2.4a). Thus, the obtained graphene could be identified and investigated. Being easy to reproduce, cheap and with the possibility of transferring to other substrates, this method was the working horse in the beginning of graphene investigations [44], which still produces the most defect-free samples up to this date. Nevertheless, it has some obvious disadvantages. As a manual method, the production rate is very low and prone to failure i.e. the material does not attach to the surface of the substrate. Even after a successful attachment, the search of the adhered flakes by an optical microscope, which are usually a mixture of isolated graphene samples and stacks of 2 or more graphene layers (Figure 2.4a) not larger than hundreds of micrometers, is a time-consuming task. Additionally, the yield of isolated graphene samples obtained, the position on the substrate and the size of the samples are unpredictable. Nevertheless, this is still a widely used method for principle-of-proof investigations.

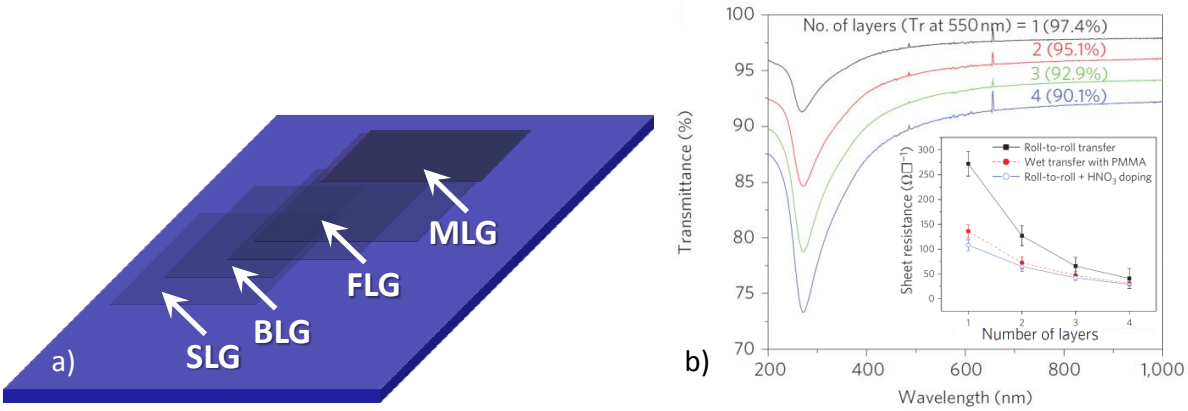

Figure 2.4: (a) Graphene's nomenclature in function of its number of layers and the reflection caused by a SiO_2/Si substrate. (b) Dependence of the optical transmission and (inset) electrical resistance on the number of layers. Adapted from [39].

Graphene is by definition a monolayer, however, it can be often found in the

literature under different terms in function of its number of layers or size. The most common nomenclatures used are Single Layer Graphene (SLG), Bilayer Graphene (BLG), Few Layers Graphene (FLG) and Multilayers Graphene (MLG), where the latter is considered as >10 layers [45]. The optical contrast in dependence of the number of layers is schematized in Figure 2.4a. Even with a difference of only one layer, BLG can have different properties than SLG. For example, BLG can show an opening of the electronic band gap up to 0.3 eV [46] and an increase in conductivity at the cost of the reduction of its optical transmission [47] as seen in Figure 2.4b. Not only the number of layers but also the size can have an effect on the electric properties. Such is the case for the so-called Graphene Nanoribbons (GNR). GNRs are defined as graphene with widths smaller than 50 nm. With these constrictions in size, the structure at the edges of graphene starts to play a role in the electronic band structure which can also open a band gap [48]. Thus, with the objective of having a controlled production of graphene types with large yields, other approaches to synthesize have been investigated.

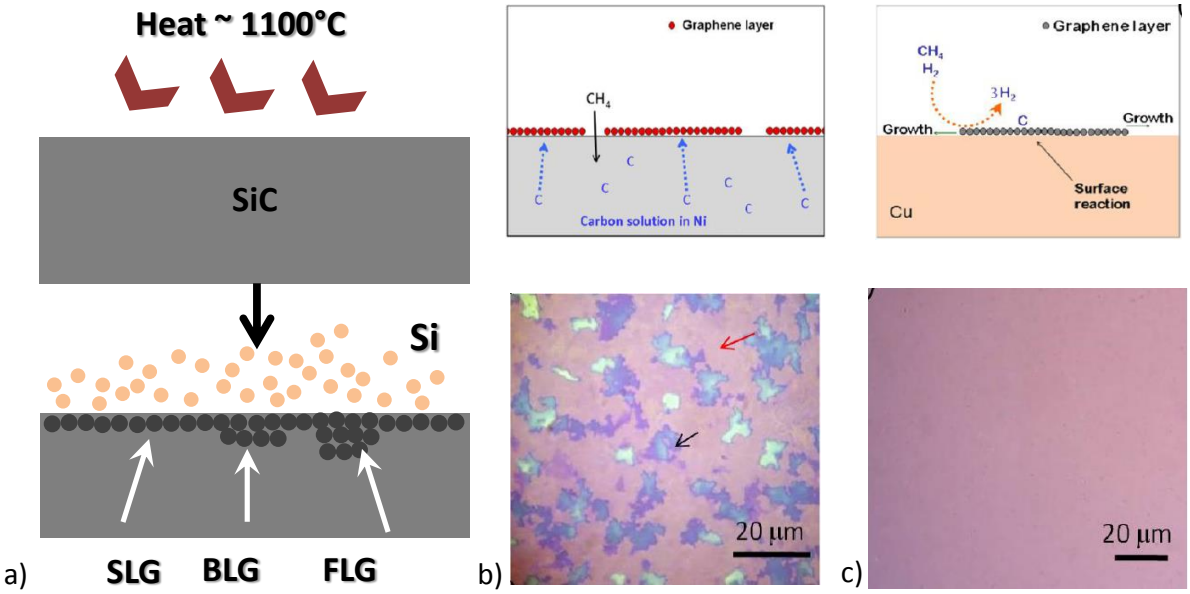

Figure 2.5: (a) Schematic diagram of the epitaxial growth of graphene at SiC surfaces. Schematic diagrams of graphene CVD growth mechanism in (b, top) Ni and (c, top) Cu and optical images of graphene transferred to a SiO_2 substrate from (b, bottom) Ni and (c, bottom) Cu. Images taken from [49].

The epitaxial growth of carbon on the surface of SiC has been investigated as a method to obtain graphene. Using high temperatures around 1100°C, in vacuum conditions or inert atmosphere, the surface layers of SiC will decompose by desorption

of Si [50]. The remaining carbon atoms will rearrange and bond to each other creating layers of epitaxial graphene (Figure 2.5a). Along with SLG, this method can also grow on its surface BLG or MLG [51]. The semi-insulating SiC substrate has the advantage that it can be structured to define graphene growth which can be used to directly produce devices in the SiC substrate [52]. Nevertheless, due to the high temperatures required, this technique cannot be directly integrated with other sensitive semiconductor devices. Furthermore, the high costs and lack of capacity to transfer to other substrates limits other applications for epitaxial graphene.

The Chemical Vapor Deposition (CVD) of graphene on metal substrates has also been extensively studied. Different metals have been investigated for its catalytic effect and reduced solubility of carbon on their surfaces such as Ni, Cu, Ru, Ir, Pt, Co, Pd, and Re [49]. The growth of graphene layers on metals such as Ni and Ru is not self-limited; due to the relative large solubility of carbon in Ni mainly mixtures of SLG, BLG and FLG are obtained as seen in Figure 2.5b [49]. The growth on Ir and Cu, being self-limited, does produce a more uniform product, yielding usually a covered area of SLG with (possible) small size areas of BLG or FLG (Figure 2.5c). Cu is more widely used due to its low price and well-established techniques for transferring the grown graphene to other substrates, which improves its large scale production potential [39]. Vertically aligned graphene or carbon nanowalls is another graphene-based material which is obtained by the plasma enhancement of the CVD process [53, 54]. Using microwaves for the plasma, the required process temperature for the synthesis can be reduced down to 500^oC, however, this out-plane graphene has not attracted much attention compared to the usual in-plane graphene.

Another approach for the production of graphene is the chemical oxidation of graphite to graphene oxide (GO) and its subsequent reduction. This method, which has different variations, can create large quantities of product with relatively little effort. For example, Schniepp et al. used thermal shock [55] for the simultaneous exfoliation and reduction of GO, while Zhu et al. used microwaves [56] and Park et al. different chemicals [57, 58] for the same purpose. All the different approaches share the same principle: the oxidation process to obtain GO separates the stacked layers of graphite at the same time it enriches it with oxygen-containing functional groups. This means that the original structure of graphene is altered and the sp^2 C-C bonds are partially replaced by sp^3 C-O bonds. To recover the original structure and thus graphene$'$s properties, the oxidized product is reduced, either chemically or thermally, thus reducing the number of

sp^3 bonds and increasing those of sp^2. Even with this partial loss of the original structure, the graphene obtained by this method has obtained a good position in a number of applications such as chemical sensors [59], capacitors [60] and conductive inks [61, 62].

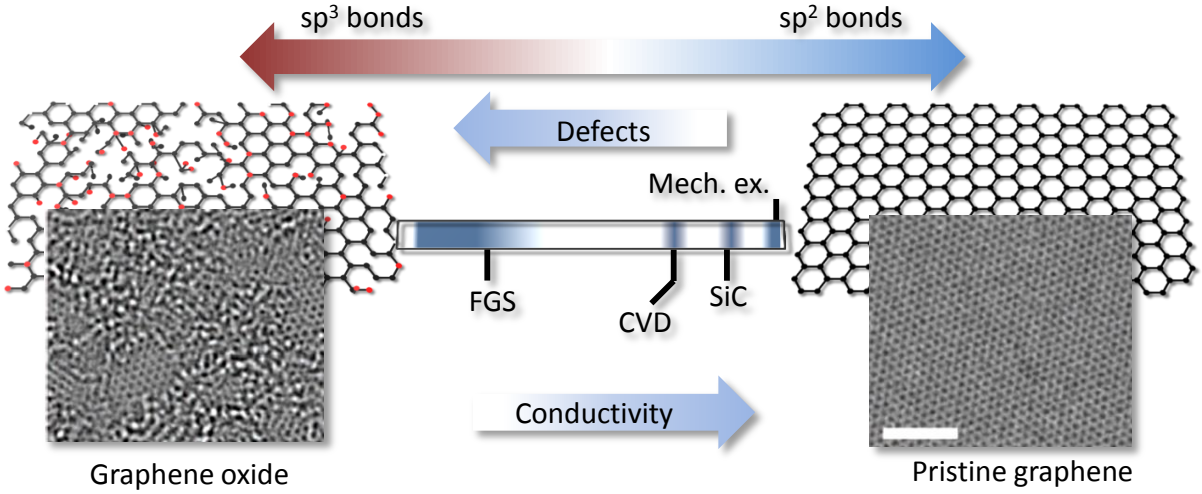

Figure 2.6: The spectrum of graphene types from GO to pristine graphene. In GO the red dots represent the oxygen atoms bonded to carbon atoms (black dots). The shades in the middle bar represents, not in scale, the ranges of crystallinity of the resulting materials obtained by the indicated techniques. Adapted from [63].

It can be seen that there is a vast range of graphene types from GO to pristine graphene as seen in Figure 2.6. In the far left of the spectrum, GO is rich in defects and sp^3 bonds (red dots). Its electrical conductivity is poor and thus considered an insulator. As soon as reduction methods are applied to GO, some functional groups are removed while others stay, partially recovering sp^2 along with conductivity. These reduced GO sheets also receive the name of Functionalized Graphene Sheets (FGS). High crystallinity and high output rate can be obtained near the right end of the spectrum by CVD, while epitaxial growth and mechanical exfoliation are close to the synthesis of pristine (defect-free) graphene, albeit with a low output rate.

FGS and CVD graphene grown on copper share the advantages of high output yield and, in comparison, more industrial-friendly approaches. Since the devices investigated in this work are based on these materials, the syntheses and fabrication of FGS and CVD devices will be explained in the next section and deepened in appendixes A.1 and A.2. An information summary of the analyzed devices on all chapters is presented in appendix B.

2.2.1 Synthesis and preparation of Functionalized Graphene Sheets samples

The synthesis of FGSs starts with the chemical oxidation of graphite by the Hummer′s method [64]. In this widely used method, graphite is mixed with $NaNO_3$ in a solution with H_2SO_4, followed by controlled variations of temperature and pressure after which $KMnO_4$ is added. Since the oxygen functional groups make GO hydrophilic [65, 66], water can be used for the dispersion of the obtained graphitic oxide flakes [64]. The synthesis of GO can also be done through the Staudenmaier process [67] which uses $KClO_3$ in the process instead. Both methods produce GO with different yields and characteristics [64] and both are used to obtain graphene flakes with sizes typically on the micrometer scale. The method of choice for the oxidation, i.e. the starting material, has repercussions on the properties of the resulting graphene material. Samples synthesized through the Hummers′ method have unique characteristics compared to the Staudenmaier process such as the presence of nitrogen in the graphene backbone [68]. From both processes, the next step is the reduction of GO. For this, the most common reduction processes are thermal [55], chemical [57] or a combination of both [69]. At this point several names have been used in literature, such as reduced graphene oxide [70], FGS [55], chemically reduced graphene oxide [57], chemically modified graphene [71], chemically functionalized graphene [72], which mainly differ from the synthesis procedure used and/or the author. The thermal reduction, as the name implies, uses heat for the removal of the oxygen species (thermal pyrolysis) on the structure of graphene. This can be done either during the exfoliation and/or afterwards. After obtaining the GO, the chemical reduction usually follows. For this purpose different compounds have been used such as hydrazine [73], hydrogen sulfide [74], sodium borohydride [75], hydrochloric acid [76].

A simplified flow chart for the fabrication of a two-terminal single flake device, obtained from GO through thermal-shock reduction, can be seen at Figure 2.7a-e. In this investigation, the GO was obtained by a modified Hummers′ method (a) [55]. The GO is then washed and dried to then be simultaneously exfoliated and reduced with a sudden increase in temperature (b). For higher levels of reduction, a subsequent thermal treatment under Ar atmosphere can be applied (c). Afterwards, the bulk material is ready to be used and/or for compositional analysis. To single out individual FGS samples from the bulk material and deposit them onto a desired substrate several approaches can be chosen. The usual procedure done in this work to obtain single flakes devices is explained next. The FGS products are suspended in ethanol for transport and storage.

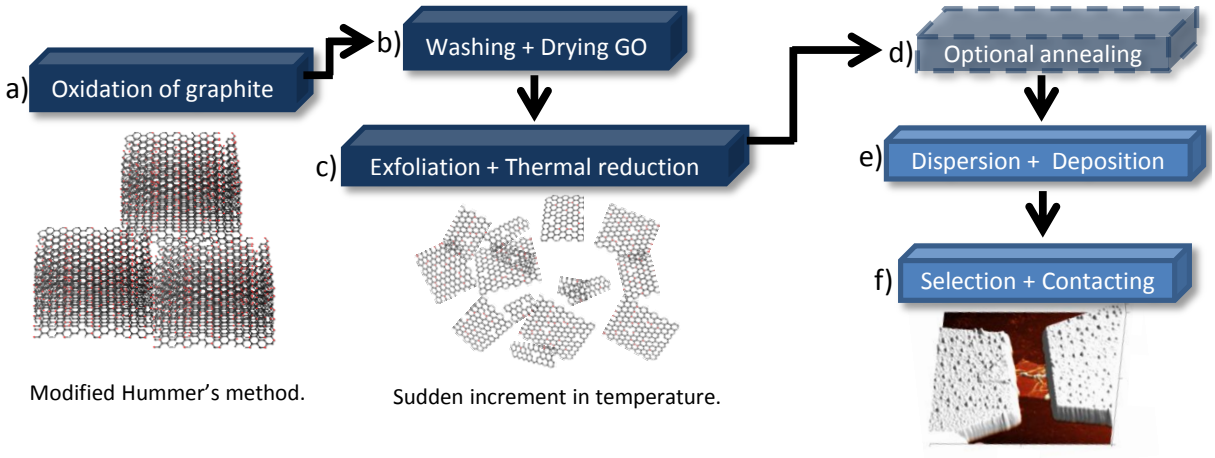

Figure 2.7: (a-c) Simplified flow chart of the production of FGS exfoliated and reduced by thermal-shock and (d-e) fabrication of a two-terminal single flake device.

The FGS-ethanol solution is dropped on a pre-patterned substrate. The flakes will be deposited after the solvent dries (d). The aleatory deposition of the individual flakes call for an optical search of a suitable sample, which is aided by pre-patterned areas over the surface of the substrate. Once the flakes are selected, the metals that will be used for electric contacts are made by e-beam lithography followed by lift-off (e). Once contacted, the single FGS can be electrically characterized. The detailed procedure for the fabrication of FGS devices is presented in section A.1.

2.2.2 Synthesis and preparation of Chemical Vapor Deposition samples

In 2009, Li and colleagues reported a method to grow large-area graphene on 25 μm thin copper foils in a hot wall furnace [11], and with it, a step forward was made in lowering the price of high-quality graphene through mass production and expanding the application spectrum. In attempts to improve the characteristics of the synthesized product, several other groups have reported variations to the well-known procedure reported by Li et al. Using Cu surface as a catalyst for the decomposition of carbon sources, conditions such as carbon source-to-diluent gas ratio, pressure and temperature [49] have been varied; carbon sources such as CH_4 [11], C_2H_4 [77], liquid [78] or solid organic matter such as cookies or grass [79] have been used. The heat source has also been varied for example using rapid heating [80], flame pyrolysis [81], cold tube wall [82] or plasma [83]. The origins of the Cu substrate used for the CVD growth also have an impact on the obtained product.

Some options are polycrystalline Cu foils [11, 84], epitaxially grown Cu with a single crystal orientation [85] or sputtered Cu films on a substrate [86]. Zhao et al. observed improved properties of graphene grown on Cu(111) compared to Cu(100) [87] and since a deposited Cu film (in principle) could be more controllable in a crystallographic context, graphene grown on Cu/SiO_2 could be appealing. However, a direct comparison shows that sputtered Cu films produced smaller grain sizes than Cu foils. Moreover, the large density of grain boundaries in Cu films increase the thickness of grown graphene while the Cu foil conserved a surface-limited growth [88]. To exemplify this, optical images (left) and AFM topography maps (right) of commercial graphene grown on a 25 μm-thick Cu foil and of sputtered Cu on SiO_2 are shown for comparison in Figure 2.8a and Figure 2.8b, respectively. In the optical image of the Cu foil a continuous surface with rippling texture is visible while in the image of the Cu film a grain-like surface with spots on the substrate uncovered by Cu (seen violet) can be observed. The AFM image of the Cu foil shows that the macrometer undulations are formed by step-like terraces down to the nanoscale. These undulations, even with hundreds of nanometers in height variations, are continuous over the foil and have no separations. The topography map of the Cu film reveals separations between adjacent grains up to hundreds of nanometers with depths larger than 100 nm. Thus, it can be expected that graphene obtained using either Cu foil or sputtered Cu film, although both produced by thermal CVD, can have evident differences which can affect the subsequent fabrication processes, e.g. during transfer. Indeed, experiments within the WET work group had also shown that the quality of the graphene sheets from thin Cu foils was always superior and relatively easier to transfer compared to Cu films. This observation is corroborated by literature, as it can be found that Cu foils-derived devices are reported much more predominantly than Cu films [89]. The commercial graphene chosen for the devices analyzed during this investigation were produced thermally on 25 μm-thick Cu foils.

The production of graphene-based devices by CVD grown on Cu-foils requires the transfer of the graphene layer to the desired substrate. The transfer has two main families of methods, namely the wet transfer and the dry transfer [90]. For the wet transfer a sacrificial layer is used, usually Polymethyl methacrylate (PMMA), which functions as a protection for graphene during transfer. This method is based on the transfer knowledge of mechanically exfoliated graphene onto other substrates [91, 92]. The flow chart of a standard wet transfer process for a Cu-CVD graphene can be followed in Figure 2.9a-j. After the CVD growth is finished (a), a PMMA layer is spin coated over the surface of

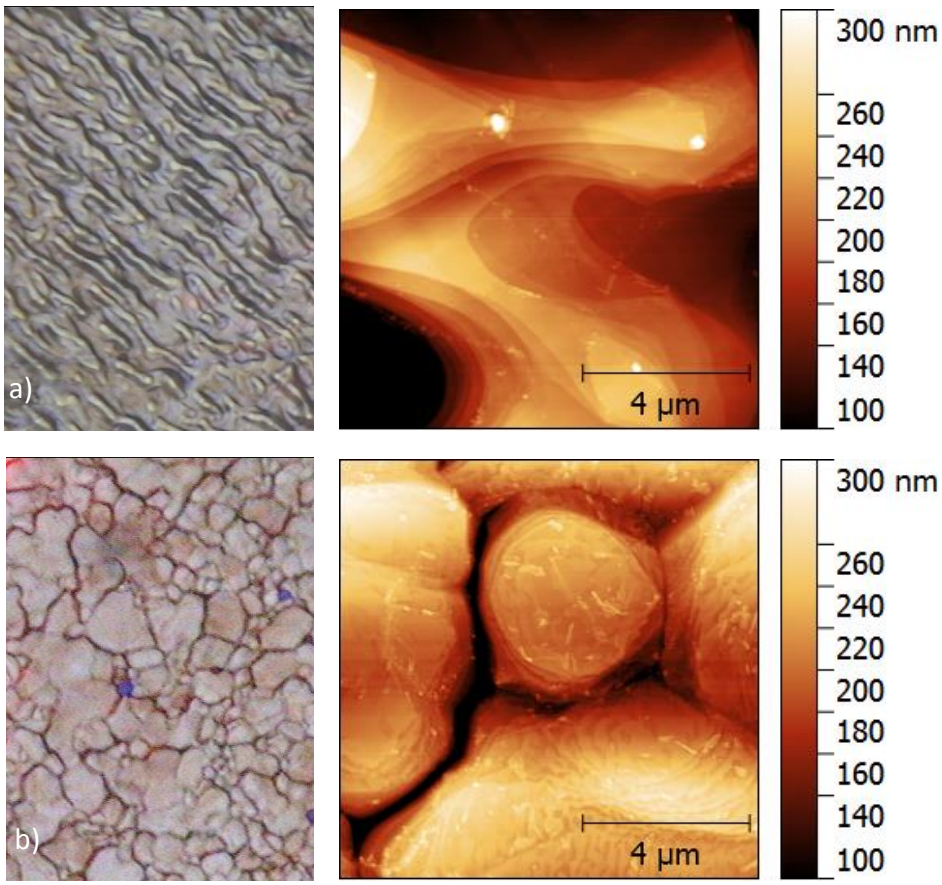

Figure 2.8: 20x optical image (left) and AFM topography (right) comparison of CVD grown graphene on (a) Cu foil (Graphenea, S.A. de C.V.) and (b) Cu film sputtered on a SiO_2 (Aixtron, Ltd) substrate.

graphene/Cu (b). Once dried, the PMMA coating will hold and protect the graphene sheet while Cu is being etched away (c). Some etchants used in literature are $FeCl_3$ [93], $Fe(NO_3)_3$ [94], $(NH_4)_2SO_4$ [95], $(NH_4)_2S_2O_8$ [90] or H_2SO_4 in electrochemical etching [96]. In this work, a $FeCl_3$ solution was used for etching the Cu. After Cu is dissolved (d), PMMA works as a temporary carrier, however, is not as rigid as the Cu foil and therefore must be "fished out" using glass (e) to place it in deionized water (DI) for further cleaning (f). The PMMA and graphene are then fished out again and placed in a different container with clean DI water to ensure Cu and $FeCl_3$ residues are removed. This last step is repeated at least three times. Once cleaned, the PMMA and graphene are fished out using the desired substrate onto which the graphene layer will be finally placed (g). The substrate is then placed on a hot plate for gentle heating (h) to remove the excess of water and ensure a firm and homogeneous adhesion of the graphene layer

to the substrate (i) before the removal of the PMMA layer. The transfer process finishes once the PMMA layer is removed with acetone (j).

The graphene layer will have a size similar to the original Cu foil and is ready for analysis or to be processed further for the production of devices using the suitable lithography procedure. This is described further in the next chapters and in detail in section A.2 for the different processes used for the devices in this work.

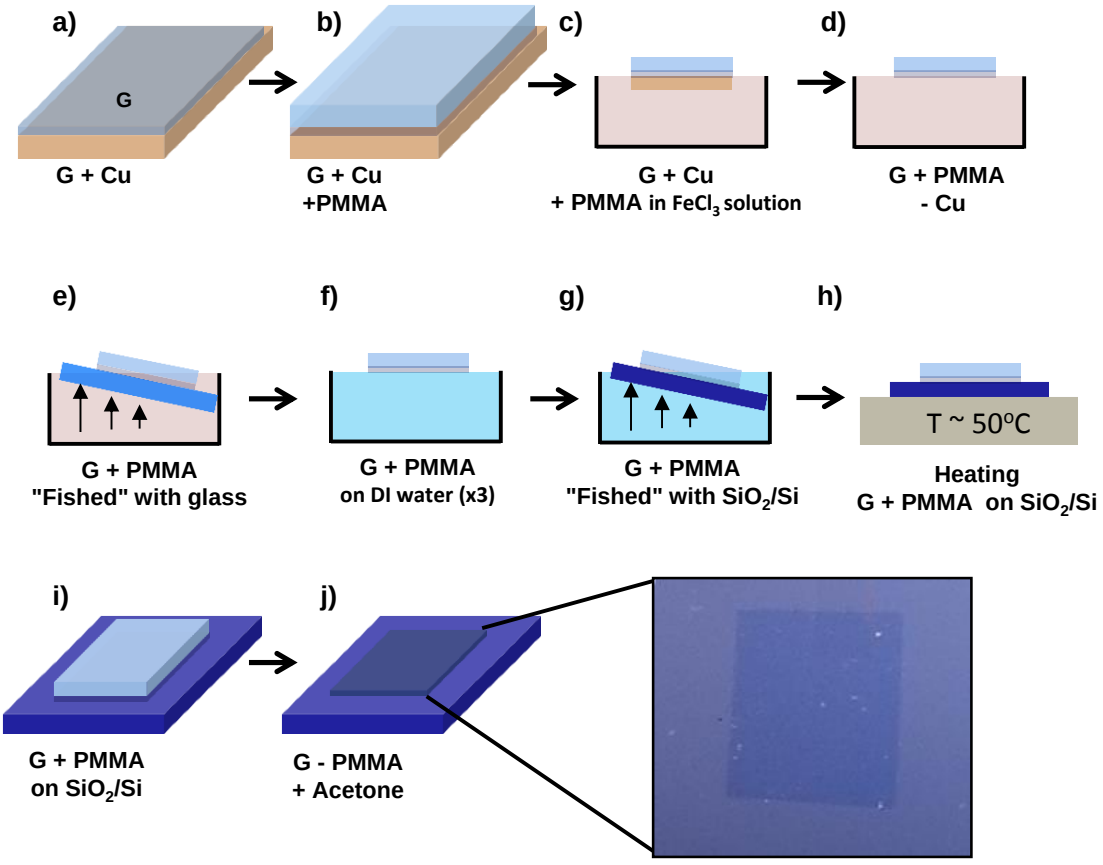

Figure 2.9: (a-j) Flow chart diagrams of the standard wet transfer process for CVD graphene grown on Cu foils with an optical image of a 1 cm^2 graphene sheet transferred onto SiO_2. G stands for graphene.

Chapter 3

Techniques for characterization

The characterization techniques used in this thesis for the analysis of graphene and graphene-based devices will be presented and explained in this chapter. First, the procedures and equipment used for the conventional macroscopic electrical characterization techniques, namely four point (4p) probe method and Transmission Line Method (TLM) will be reviewed. This is followed by the description of the interactions, mathematical models and operation modes of Atomic Force Microscopy (AFM). The chapter continues by presenting the main characterization technique of this investigation: Kelvin Probe Force Microscopy (KPFM). This AFM-derived technique is based on the macroscopic Kelvin method which will be first described, followed by its implementation on the nanoscale, the available operation modes and their attributes. Afterwards, the instrumentation used for AFM/KPFM measurements will be introduced. Finally, Raman spectroscopy principles, graphene′s Raman spectra and the equipment used for Raman measurements will be presented.

3.1 Conventional macroscopic electrical characterization techniques

The main electrical characterization of graphene and graphene devices consist on the measurement of the resistivity (ρ), the inverse of the conductivity σ (see Equation 2.7), which can be accessed by measuring the electrical resistance (R), defined by Ohm′s law as the voltage (V) divided by the electric current (I) flowing between two points,

$$R = \frac{V}{I} \tag{3.1}$$

The device′s I dependence with respect to the applied V, known as output characteristics or simply as IV curves, can be linear or non-linear. Since all devices require the use of at least two electrical contacts for the injection and extraction of charge carriers, the electrical resistance of the whole device is then a contribution of the material (device′s channel) and the contacts. Throughout this work, the electrical contact where the voltage will be applied is termed drain contact independently of the polarity applied. In the same way, the grounded electrical contact is denoted source contact (Figure 3.1a). Therefore the current and voltage between these contacts are denominated I_{ds} and V_{ds}, respectively. For a linear IV dependence (Figure 3.1b) the slope (dV_{ds}/dI_{ds}) equals the overall resistance of the two-terminal device (R_{2p}). Here it is considered that the channel and the contacts have an ohmic behavior. In the non-linear case (Figure 3.1c) a specific section of the curve can be selected and linearized to obtain the average resistance at determined voltages. As it will be seen in chapter 5, this behavior could be caused by the material itself and/or the material/contact interfaces known as Schottky contacts.

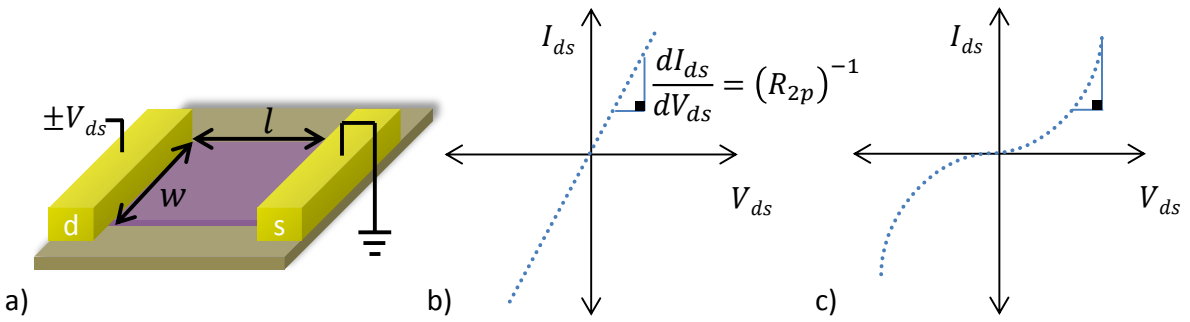

Figure 3.1: (a) Schematic diagram of a two-terminal device and illustration of its possible output characteristics: (b) linear and (c) non-linear behavior. For the non-linear case, the linearization of the operation conditions is exemplified.

This work concentrates on determining the contribution of the contact resistivity (ρ_c) and the sheet resistivity (ρ_s) to the overall resistance of micrometer and submicrometer graphene devices. In 3D materials, contact resistivity is normalized as the resistance at the contact (R_c) times the area of contact, thus reported in Ωcm^2. However, in 2D materials, such as graphene, it is usual to find ρ_c normalized just by the width (w) of contact ($\rho_c = R_c w$), hence reported in $\Omega\mu$m. In the channel, due to graphene′s thinness, ρ_s is normalized as the resistance at the channel (R_s) times its aspect ratio (Figure 3.1a), i.e. its width divided by its length ($\rho_s = R_s w/l$), thereby reported in $\Omega/\square$. Thus, the total resistance obtained by the output characteristics of a two-terminal device is known as two-point resistance (R_{2p}), and corresponds to the contributions of the drain and source contacts ρ_c, as well as the channel ρ_s,

$$R_{2p} = 2\rho_c/w + \rho_s l/w \tag{3.2}$$

In order to obtain ρ_c and ρ_s two methods are traditionally used: 4-point probe measurements (4p) and the Transmission Line Method (TLM).

3.1.1 Four point probe method

This method relies on eliminating the contact resistance contribution by using a set of four aligned probes, with a constant separation (l) between probes. Two outer probes are used to inject a current into the material, while the other two probes, the inner ones, are used as voltmeters (Figure 3.2a). Since the inner probes draw very little current, the voltage drop across the probes resistance and at the interface probe/material is very small, thus its measured resistance (R_{4p}) is approximate only to the contribution of the material′s channel [97]. In the case of graphene channels, with spacing in the order of few μm, this principle is used as an approximation to remove the R_c of the metal deposited on the material′s surface. The actual setup for a graphene device with 4p layout measurement is shown in Figure 3.2b, using one channel of a Source-Measure Unit (SMU) for the current bias and R_{2p} measurement of the outer probes, and one channel for the voltage difference and R_{4p} measurement of the inner probes. Optionally another SMU can be connected to the substrate to apply a perpendicular electric field to the channel by means of a gate voltage V_{gs} (see section 2.1).

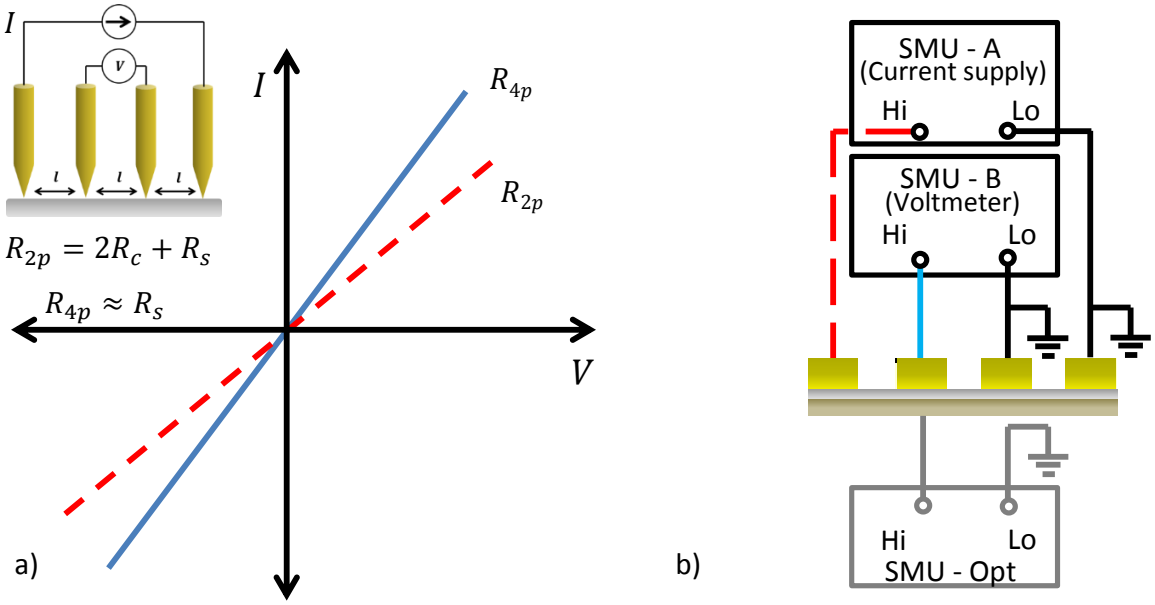

Figure 3.2: (a) Schematic of the IV curves for the 2- and 4-probe measurement and (b) connection diagram used for the 4-probe experimental analysis.

3.1.2 Transmission Line Method

This method was originally proposed by Schockley [98] to determine ρ_c for planar ohmic contacts and it relies on the assumption of a constant ρ_s along the channel, i.e. no material's variations under the contacts [99]. This method is applied to obtain ρ_s and ρ_c for graphene devices by plotting the R_{2p} times the width w of the graphene channel as a function of a variable separation of the contacts (l_n),

$$R_{2p} * w = 2\rho_c + \rho_s l_n \tag{3.3}$$

The measurement results are linearized and the slope corresponds to ρ_s while the intercept of y-axis will equal $2\rho_c$ (Figure 3.3a),

$$\frac{R_{2p} * w}{2} = \rho_c \Big|_{l=0} \tag{3.4}$$

The connection diagram and sequence for the TLM analysis in graphene is schemed in Figure 3.3b. Again, during the analysis an optional V_{gs} can be applied by means of a back gate contact.

The macroscopic characterizations presented in this work were done using a *Suss Microtec* PM5 probe station. The PM5 station uses PH110 *Suss Microtec* manual probe

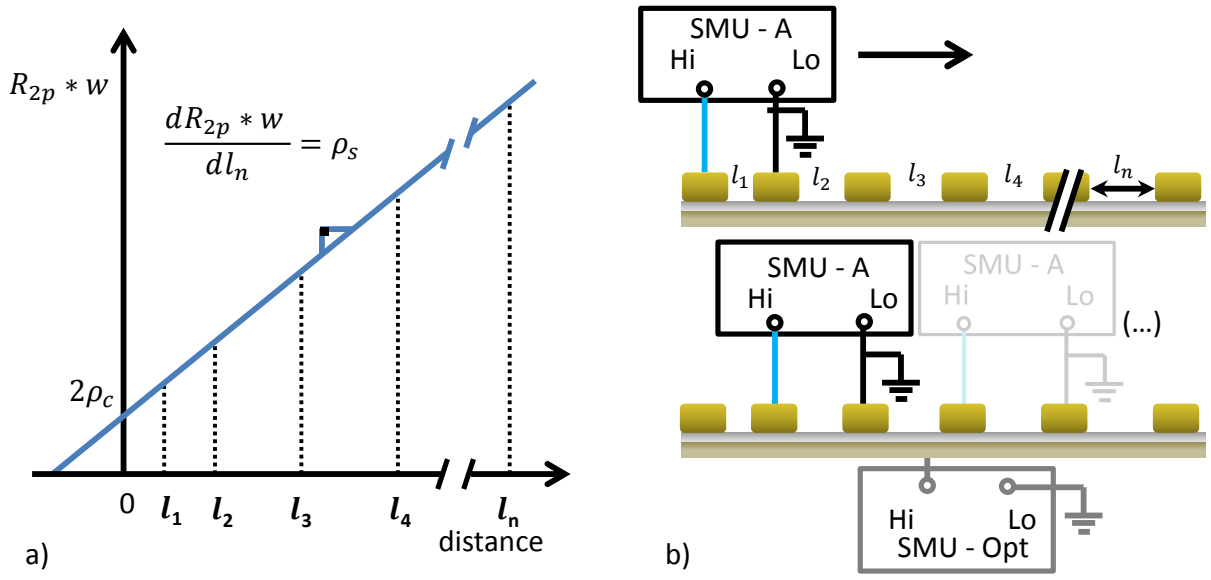

Figure 3.3: (a) Schematic of the distance vs 2-probe resistance plot and (b) connection diagram of the sequence used for the TLM experimental analysis

positioners with a *xyz*-screw resolution of 350 μm/rev and low resistance Beryllium Copper or Tungsten probes with a 6 μm radius from *American Probe and Technologies Inc.* All electric measurements were done using a two-channel *Keithley* SMU 2612.

It can be noted that these two methods rely on the use of more than a pair of contacts for the estimation of channel and contacts contribution to the total resistance. Hence, these macroscopic techniques can neither provide a direct estimation of the contact and channel contributions on operational two-terminal devices nor spatially resolved information. In the next section the use of AFM, with its intrinsic lateral resolution, will be presented as an electrical characterization technique for the estimation of the contact and channel contributions to the total resistance of two-terminal devices.

3.2 Atomic Force Microscopy

Atomic Force Microscopy (AFM) belongs to a microscopy family, known as Scanning Probe Microscopy (SPM), which began in 1982 with the work of G. Binning and H. Rohrer at IBM laboratories [100, 101, 102]. This branch of microscopy covers a wide range of imaging with spatial resolution from several hundreds of μm down to atomic bonds [103, 104]. SPM techniques separate themselves from e.g. electron microscopy, by the use of a probe, for the imaging of the sample. Therefore its operation can be not only in high vacuum but also in air or even liquids [105, 106, 107]. Within the SPM family, AFM, also known as Scanning Force Microscopy, is one of the most versatile tools for the study and manipulation of matter on the nanoscale from material engineering to biological applications [105, 106].

3.2.1 Operation principle

As part of the SPM family, AFM uses a probe to scan the sample′s surface. The probe is usually a nanometric tip made of silicon, at the very end of a micrometer flexible beam, known as the cantilever, which is attached to a millimetric carrier body, known as support chip (Figure 3.4a and Figure 3.4b). Depending on the operation mode, different forces act on the tip and cantilever, causing small deflections (Δz) of the latter (Figure 3.4c). The force $\vec{F}$ acting on the tip, causing the cantilever′s deflections, can be represented by Hooke′s law as

$$\vec{F} = -k\Delta z\hat{k} \tag{3.5}$$

where k is the spring constant of the cantilever in N/m and $\hat{k}$ the unit vector in the z-direction.

At the nanometric distances between tip and sample, with which AFM works, near field forces account for $\vec{F}$. In function of the distance, near field forces are separated in short and long range forces [108]. Characteristic of the short range forces are the repulsive forces between the electron orbitals of the tip and the sample atoms. Van der Waals and electric interactions between the tip and the sample are classified as long range and attractive forces (electric interactions can also present repulsive forces). The separation of the involved forces and their measurement diversify the applications of AFM, e.g. to analyze the electric or magnetic properties of any given sample [109, 110].

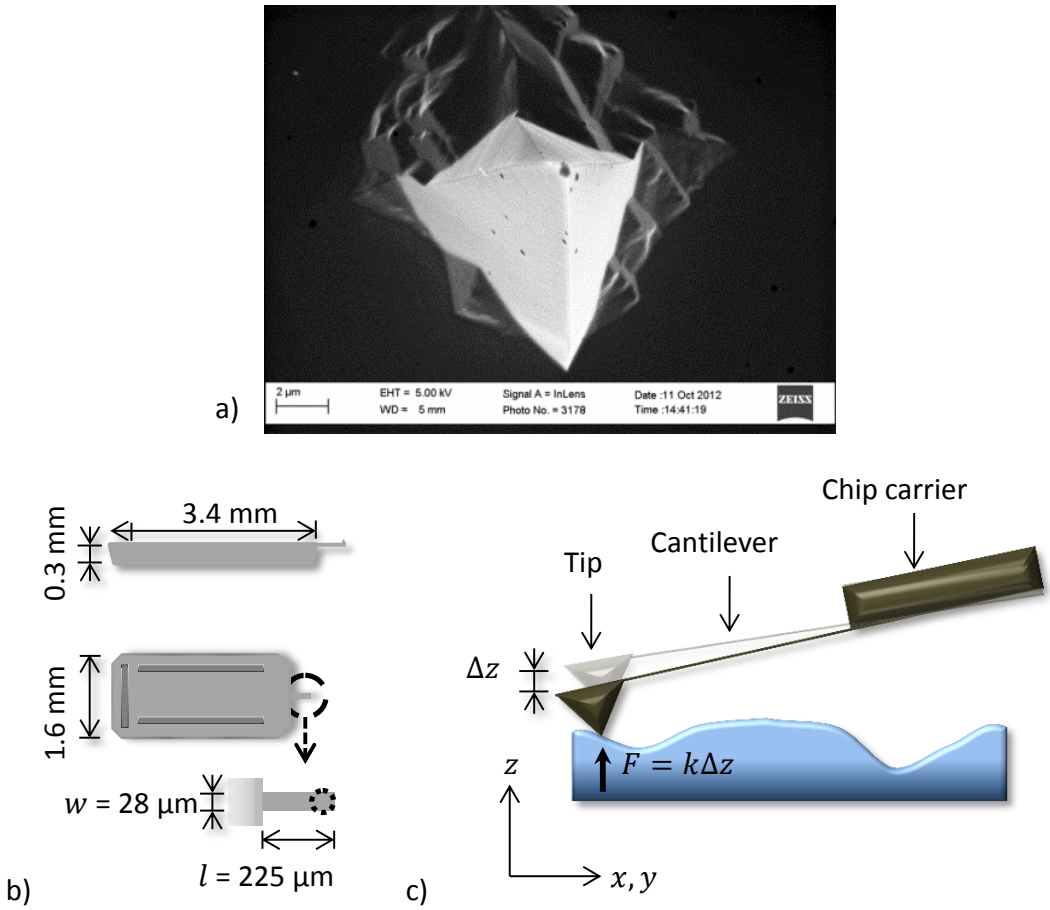

Figure 3.4: (a) Scanning electron microscope image of the characteristic pyramidal shape of the tip. (b) Diagram of the support chip and cantilever′s common dimensions. (c) Scheme of the AFM operation principle.

3.2.2 Conventional AFM instrumentation

A common setup with the core components for AFM measurements is shown in Figure 3.5 [105, 111]. The scanning of the tip over the surface of the sample in the x- and y-direction can be in steps of tenths of nanometers to tens of micrometers, while the z- direction steps can be in tenths of nanometers to a couple of micrometers. These movements are either done by the stage controller with a piezoelectric tube or by the AFM head, which holds the support chip. In the AFM/KPFM instrumentation used for this investigation (see subsection 3.2.8), the scans are done by the stage controller i.e. the tip is in a fixed position and the sample moves under it via a piezoelectric tube. The detection of the cantilever′s deflections can be either by optical or non-optical means, the former usually being the most common in all commercial AFMs. The optical detection is done by a

laser beam which is directed to the cantilever′s back and reflected towards a mirror. The mirror angle can be adjusted in order to center the reflected laser on a Quadrant Photo Diode (QPD). The QPD photocurrent signal is a measure of the tip-sample interactions at different positions. This signal is sent to a detection unit to extract the corresponding deflections. The amount of deflection is then compared to a set point on a Proportional, Integral and Derivative (PID) controller. The calculated error of the PID is used by the piezoelectric tube as feedback for the height control, therefore known as z-controller. For the dynamic operation modes (see subsection 3.2.4), a piezoelectric dither, which is in direct contact with the support chip, creates mechanical oscillations of the cantilever at a specific frequency (f).

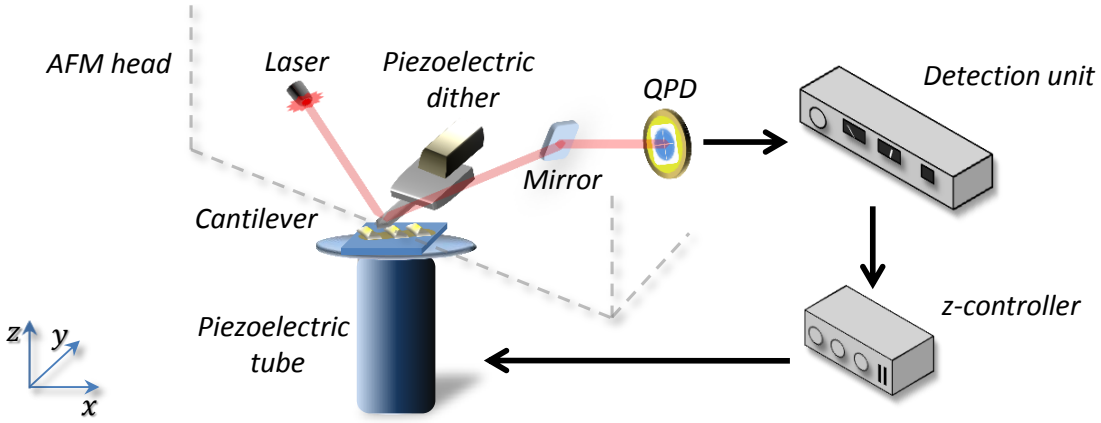

Figure 3.5: Simplified diagram of a conventional AFM setup with the core components for the optical detection of the cantilever/tip deflections.

3.2.3 Relevant tip-sample forces and operation modes

There are basically two modes of operation for AFM: contact and dynamic modes. Dynamic modes consist of non-contact and intermittent mode [112, 113, 114] differentiated by its cantilever/tip-sample interactions. The tip-sample force, $\vec{F}_{ts}$, causing the cantilever′s deflections is the sum of repulsive ($\vec{F}_{rep}$), attractive ($\vec{F}_{attr}$), electrostatic ($\vec{F}_{el}$) and magnetic forces ($\vec{F}_{mag}$),

$$\vec{F}_{ts} = \vec{F}_{rep} + \vec{F}_{attr} + \vec{F}_{el} + \vec{F}_{mag} \tag{3.6}$$

Without the specific coating, the tip will have no electrostatic and/or magnetic interactions with the sample. The attractive and repulsive forces are, however, always present and will be described next. At distances of less than 1 nm, the deflections of the

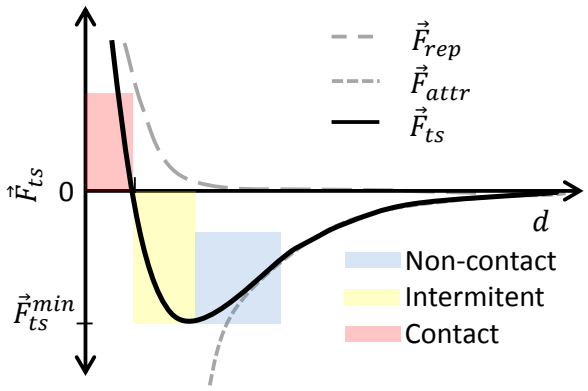

Figure 3.6: Diagram of the resulting force exerted to the AFM tip as a sum of repulsive and attractive forces by variations in the tip-sample distance. The AFM modes of operation are delimited in color shades.

cantilever arise from the overlap of the electron orbitals and the repulsion of the tip and sample atoms, as stated by the Pauli principle. The repulsive force is stated as

$$\vec{F}_{rep} = \left(\frac{\sigma_{rep}}{d^{13}}\right)\hat{k} \tag{3.7}$$

where d is the tip-sample distance and σ_{rep} is a case-specific proportional constant.

At tip-sample separations above 1 nanometer, the attractive forces, also known as van der Waal forces, start to be relevant [115]. Up to 100 nm in distance these forces can still effectively cause tip-sample interactions. The attractive force has the form

$$\vec{F}_{attr} = -\left(\frac{\sigma_{attr}}{d^{7}}\right)\hat{k} \tag{3.8}$$

the negative sign is a convention which represents the work exerted by the atoms due to attraction, while $\vec{F}_{rep}$ has a positive sign since work must be provided to force the overlapping of the atom′s electron orbitals.

Finally, using Equation 3.7 and Equation 3.8 the tip-sample interactions for an uncoated tip has the form

$$\vec{F}_{ts} = \left(\frac{\sigma_{rep}}{d^{13}} - \frac{\sigma_{attr}}{d^{7}}\right)\hat{k} \tag{3.9}$$

which corresponds to the derivative of the Lennard-Jones potential model [108] and is represented in Figure 3.6.

The operation mode regions can be described in function of the tip-sample distances. At large separation distances, say hundreds of nanometers, there is no interaction, and

the force $\vec{F}_{ts}$ is close to zero. As soon as the tip gets closer to the sample ($d \rightarrow 0$), $\vec{F}_{attr}$ experiences a polynomial growth ($\sim d^7$). This is the beginning of the dynamic modes, specifically, non-contact mode of operation (blue shade, Figure 3.6). By further reducing d, $\vec{F}_{ts}$ reaches a minimum ($\vec{F}_{ts}^{min}$) which corresponds to the distance at which $\vec{F}_{rep}$ start to be relevant. By decreasing the distance even more, the non-contact mode is left behind, to then enter the intermittent (tapping) mode (yellow shade, Figure 3.6) operation region. When the tip has made actual contact with the surface the forces are zero, ($\vec{F}_{ts} = 0$). This is the end point of the intermittent contact mode and the beginning of the contact mode operation region (red shade, Figure 3.6). By further decreasing d, the tip will press against the sample thus flexing the cantilever. The end of the contact mode operation region would be basically exceeding the stiffness of the cantilever to the point of damage.

Along with the operation modes, the types of tip, cantilever and coatings diversify the measurement capabilities of AFM. As mentioned before, the electric or magnetic properties of a sample can be analyzed, by coating the silicon tip with the respective materials, i.e. with Conductive AFM (CAFM), Electric Force Microscopy (EFM) or Magnetic Force Microscopy (MFM), respectively. In Table 3.1 a few examples are presented as an insight into the differences in properties of commercially available tips. Usually, the most important characteristics are the type of tip, the spring constant k, the fundamental mechanical resonant frequency f_0 and the coating materials. The cantilevers can then be produced with different aspect ratios and/or are coated with different materials for different purposes such as to increase the cantilever′s reflection (of the laser) or to improve hardness for contact mode.

Commercial name	k (N/m)	f_0 (kHz)	**Coating**	**Application**
Contact-G	0.2	13	None	AFM
ContAl-G	0.2	13	Electric (Al)	AFM, CAFM
MagneticMulti 75	3	75	Magnetic (Co, Al)	AFM, MFM
ElectriTap 300	40	300	Electric (Pt, Ir)	EFM, KPFM

Table 3.1: Examples of commercially available AFM tips, properties and applications.

3.2.4 Dynamic modes

To measure the tip-sample interactions in dynamic modes, both in non-contact and intermittent modes, it can be selected whether the cantilever amplitude is modulated (AM-AFM) or the cantilever frequency (FM-AFM). The selection of either modulation is

dependent on the analysis conditions. In vacuum conditions, FM-AFM is advised [116], while for air and liquid conditions [106, 114] AM-AFM is suitable. Since the experiments in this work are performed in ambient conditions, the focus will be on AM-AFM.

The cantilever′s amplitude (A) is a function of the frequency used for the oscillation. The frequency at which the amplitude has an absolute maximum (free-amplitude) corresponds to the fundamental mechanical resonant frequency f_0. The value of f_0 depends on the cantilever properties itself such that,

$$f_0 = \frac{1}{2\pi}\sqrt{\frac{k}{m^*}}$$

or

$$\omega_0 = \sqrt{\frac{k}{m^*}} \tag{3.10}$$

where m^* is the effective mass of the cantilever and ω_0 the angular frequency, where $\omega = 2\pi f$.

To experimentally obtain f_0 the piezoelectric dither vibrates the cantilever (see subsection 3.2.2), far away from the sample, over a range of frequencies as the QPD records the amplitude. The small amplitude obtained from the QPD photocurrent is then amplified to match a user-specified value of A_0. The bandwidth of the QPD provides the range of frequencies at which the cantilever′s oscillations can be detected, therefore allowing or preventing the use of specific cantilevers with high resonant frequencies. After f_0 and A_0 are established, the system selects an operation frequency $f_0^{'}$ close to the resonant frequency (hundreds of hertz) and readjusts to 0^o the phase between the signal send to the piezoelectric dither and that of the cantilever/QPD signal response.

To interact with the sample, d is reduced, such that $\vec{F}_{ts}$ with a larger attractive component will start to affect the properties of the cantilever. By considering this interaction as a weakly perturbed harmonic oscillator with small amplitudes and small force gradients [113], the perturbed resonant frequency ($\tilde{f}_0$) is caused by a change of the spring constant ($\tilde{k}$). This, in turn, is caused by the changes of the interactions forces as

$$\tilde{k} = k - \frac{\partial \vec{F}_{ts}}{\partial z} \tag{3.11}$$

The shift of the fundamental mechanical frequency due to the tip-sample interactions causes a reduction of A_0. This will continue until the amplitude equals the selected amplitude for set point (A_{sp}). This stage of operation is known as engaged or landed. During operation, valleys (peaks) in the sample′s topography would cause an increase (decrease) in the value of A_{sp} (Figure 3.7a). These changes in amplitude will be controlled by the z-controller to match A_{sp} again, as seen in Figure 3.7b.

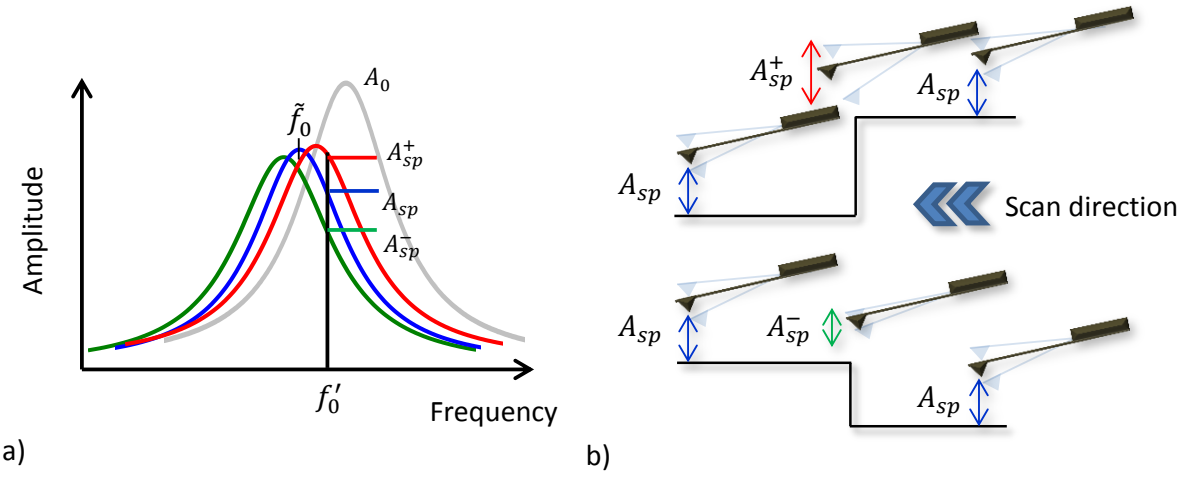

Figure 3.7: Diagram of the (a) free amplitude reduction due to the tip-sample interactions and reduction or increase in amplitude relative to A_{sp}. (b) Response of the tip oscillation amplitude to topography features.

The topography map is seen as a contrast image of the z-controller corrections due to the amplitude variations tracing the topography of the measured sample. Usually, the amplitude and phase variations are recorded along topography, extending the available information of the AFM analysis. With the use of the correct coating for the cantilever tip, the $\vec{F}_{el}$ and $\vec{F}_{mag}$ components will interact as well, and could be observed in the relative changes of the phase channel [114].

3.2.5 Electrostatic force in AFM

As mentioned in subsection 3.2.3, a metallic coating on the tip enables electric interactions with the sample, i.e. $\vec{F}_{el}$ becomes relevant for tip-sample interactions and is described as follows. The apex of the metal-coated tip and the sample can be considered as a parallel plate capacitor with energy E_{el},

$$E_{el} = \frac{1}{2}CV^2 \tag{3.12}$$

where C is the capacitance, V is the voltage between tip and sample.

The cantilever′s oscillations will cause a variation of the capacitance. The electrostatic force $\vec{F}_{el}$ between the capacitor plates is the derivative of E_{el}. Thus, considering a very sharp tip, where only the forces acting normal to the sample surface, i.e. z-direction, are relevant, the electrostatic force will have the form

$$\vec{F}_{el} = \nabla E_{el} = -\left(\frac{1}{2}\frac{\partial C}{\partial z}V^2 - CV\frac{\partial V}{\partial z}\right)\hat{k} \tag{3.13}$$

Considering a constant voltage in respect to the distance ($\frac{\partial V}{\partial z} = 0$), the electric force is then

$$\vec{F}_{el} = -\frac{1}{2}\frac{\partial C}{\partial z}V^2\hat{k} \tag{3.14}$$

Thus, the capacitive gradients are a function of the tip-sample distance, but also, as $\vec{F}_{el}$ are long range forces, of the geometrical form of the metallic tip apex, the cone and the cantilever as shown in Figure 3.8. Here it can be seen that surrounding areas (1-4) with different work functions (gray and black areas) can have capacitive contributions not only from interactions with the tip apex but also from the tip cone. Therefore, to improve the sensitivity and resolution to $\vec{F}_{el}$ it is desired to reduce the n contributions from other areas other than those underneath the tip apex.

Even more, the relative tilt of the tip/cantilever over the sample can have an influence, thus an analytic determination of all the capacitance acting on a tip can be specific for every case and complicated. The usual approximation used is that of a system of parallel plate capacitors, with individual contributions C_n at specific heights z_n, such that

$$\frac{\partial C}{\partial z} = \sum_{1}^{n}\frac{\partial C_n}{\partial z_n} \tag{3.15}$$

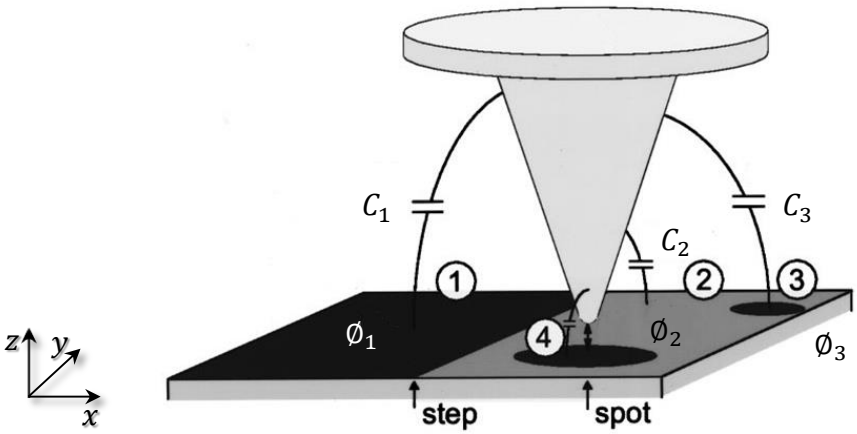

Figure 3.8: Capacitance system model of the KPFM setup. The measured F_{el} is a weighted average of the different contributions over the tip apex, cone and cantilever. The sample′s contrast represents different materials. Adapted from [117].

3.2.6 Principle of the Kelvin method

The principle of the Kelvin method for the measurement of the contact potential difference (CPD) between two metals is a macroscopic analysis established in 1898 by Lord Kelvin [118, 119]. To clarify the principle, in Figure 3.9a, two different metals are shown with work functions ϕ_A, ϕ_B and Fermi levels $E_{F,A}$, $E_{F,B}$ being separated by a gap and without any electrical contact (open circuit). In such conditions, the vacuum energy levels E_{vac} are leveled, while the E_F have different positions.

If the materials achieve an electrical contact (close circuit) as shown in Figure 3.9b electrons will flow from the material with a larger Fermi level (A) to the material with a lower Fermi level (B), to level their E_F position. This diffusion of charge carriers causes also a polarization of the surface of the materials and a shift in E_{vac} as well. This new equilibrium position generates an electric potential V_{CPD}, which is proportional to the difference of the material′s work functions [120],

$$V_{CPD} = \frac{\Delta\phi}{e} = \frac{(\phi_B - \phi_A)}{e} \tag{3.16}$$

The polarization of the surface caused by the CPD creates an electric field in the gap between the materials with a force $\vec{F}_{el}$. This force can be nullified by applying a voltage V_k (Kelvin voltage) to the circuit, of the same magnitude but different polarity than $(\phi_B - \phi_A)$, such that the position of the E_F and E_{vac} returns to the initial conditions.

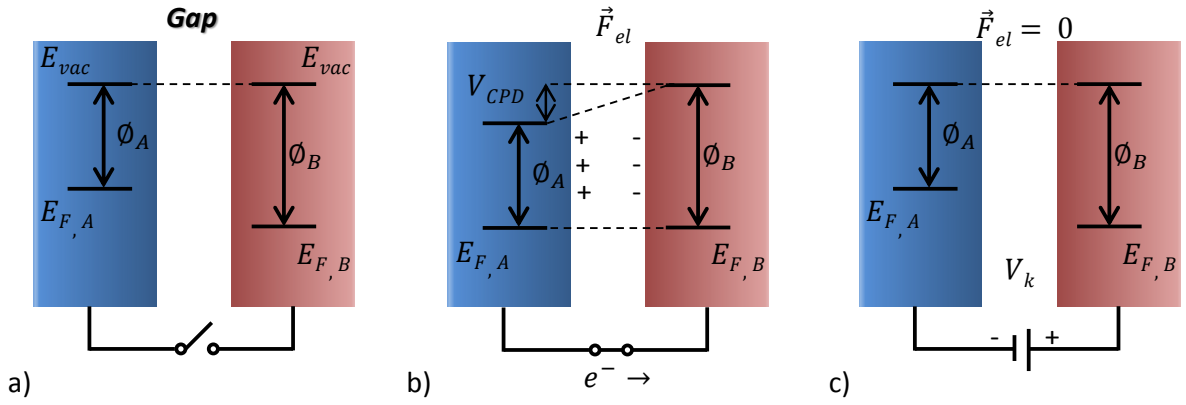

Figure 3.9: Diagram of the Kelvin method principle for two metals A and B separated by a gap. (a) Without any electric connection, both E_{vac} are aligned. (b) An electrical connection levels the position of the E_F due to electron migration, causing in turn a potential V_{CPD} and a polarization at the surfaces. (c) Applying a voltage V_k will compensate V_{CPD} and the polarization, leveling anew the E_{vac}.

The relevance of Equation 3.16 with respect to the grounding of the technique will be studied in subsection 4.2.1.

3.2.7 Kelvin Probe Force Microscopy

The measurement of the CPD at the nanoscale in Kelvin Probe Force Microscopy (KPFM) is based on the electric field created between the tip and the sample. Using the same considerations of a parallel plate capacitor as in Figure 3.8, the objective of KPFM is to nullify $\vec{F}_{el}$, caused by V_{CPD}, by applying the correct V_k during the mapping of the sample. The electrostatic interactions are sensed by applying a modulating AC signal of amplitude V_{ac} and frequency ω_{ac}, ($\omega_{ac} = 2\pi f_{ac}$) to one material while the other remains grounded. Hence, in KPFM measurements the voltages involved are,

$$V = V_k + V_{CPD} + V_{ac} sin\left(\omega_{ac} t\right) \tag{3.17}$$

Thus, V can be substituted in Equation 3.14, such that

$$\vec{F}_{el} = -\frac{1}{2}\frac{\partial C}{\partial z}\left[V_k + V_{CPD} + V_{ac} sin\left(\omega_{ac} t\right)\right]^2 \hat{k} \tag{3.18}$$

The binomial expansion of Equation 3.18 can also be written by separating its spectral components as $\vec{F}_{el} = \vec{F}_{dc} + \vec{F}_{\omega_{ac}} + \vec{F}_{2\omega_{ac}}$, where,

$$\vec{F}_{dc} = -\frac{\partial C}{\partial z}\left[\frac{1}{2}\left(V_k + V_{CPD}\right)^2 + \frac{V_{ac}^2}{4}\right]\hat{k} \tag{3.19}$$

$$\vec{F}_{\omega_{ac}} = -\frac{\partial C}{\partial z}\left[\left(V_k + V_{CPD}\right)V_{ac}sin\left(\omega_{ac}t\right)\right]\hat{k} \tag{3.20}$$

$$\vec{F}_{2\omega_{ac}} = \frac{\partial C}{\partial z}\frac{V_{ac}^2}{4}cos\left(2\omega_{ac}t\right)\hat{k} \tag{3.21}$$

where $\vec{F}_{dc}$ is a contribution to topography, $\vec{F}_{\omega_{ac}}$ is used to calculate the CPD and $\vec{F}_{2\omega_{ac}}$ is related to the capacitance of the material. It can be deduced from Equation 3.19 that the amplitude of the modulation voltage is desired to be as low as possible to reduce cross-talk between electric and topography measurements.

KPFM can be done parallel or subsequently to topography measurements, namely as single or double pass. In single pass measurements the amplitude variations of the cantilever′s mechanical oscillations at $\omega_0^{'}$ are measured along with the electrostatic interactions at ω_{ac} using two dedicated detection units, where $\omega_{ac} \neq \omega_0^{'}$. In double pass measurements, a topography line is measured first. Once finished, the piezoelectric dither and z-controller are turned off and the tip retraces again (double pass) the topography information. To prevent damage to the tip and/or sample the tip is retracted from the surface of the sample. During the second pass the electrostatic interactions are measured using a modulation AC signal which is directly applied to the tip, usually at $\omega_{ac} \approx \omega_0^{'}$. Due to the retraction, double pass techniques are usually time-consuming and the separation used, often >10 nm, causes an intrinsic loss of resolution as well. In this work, only single pass KPFM measurements are used.

AM-KPFM

The established technique at the Duisburg-Essen University′s WET workgroup, where this investigation was done, is the Amplitude Modulation KPFM (AM-KPFM). In AM-KPFM, the amplitude of the signal at ω_{ac} is proportional to the $\vec{F}_{\omega_{ac}}$ component of $\vec{F}_{el}$ and is used to determine the CPD by means of V_k (see Equation 3.20). To measure this in single pass AM-KPFM, the interactions at the ac-frequency ω_{ac} are measured by a lock-in amplifier (LIA-II) in parallel with the lock-in amplifier for topography (LIA-I) as seen in Figure 3.10.

The amplitude of the AC signal is then proportional to the in-phase component of LIA-II, X_{II}, such that,

$$X_{II} \propto \left|\vec{F}_{\omega_{ac}}\right| \tag{3.22}$$

$$X_{II} = 0 \iff (V_k + V_{CPD}) = 0 \tag{3.23}$$

The AM-KPFM setup uses the sensitivity of the second resonant frequency of the mechanical oscillations, ω_1, as ω_{ac} [121]. Therefore, $\omega_0^{'}$ can be applied to the dither for topography and, simultaneously, ω_1 ($\omega_1 \sim 6.3\omega_0$) direct to the tip for the potential profiling. For specificity, as both AFM and KPFM are working with AM, the setup can be referred as AM-AM-KPFM. Operationally speaking LIA-I and LIA-II have as input the deflection signal from the QPD. LIA-I has as reference signal (Ref) the mechanical oscillations at $\omega_0^{'}$ while LIA-II has ω_{ac} as Ref. The signal ω_{ac} can come from the LIA-II itself or from an external signal generator. Since this mode usually requires voltages V_{ac} > 1 V_{p-p} [12, 112], and due to specifications of the LIA, an external generator is used in this setup.

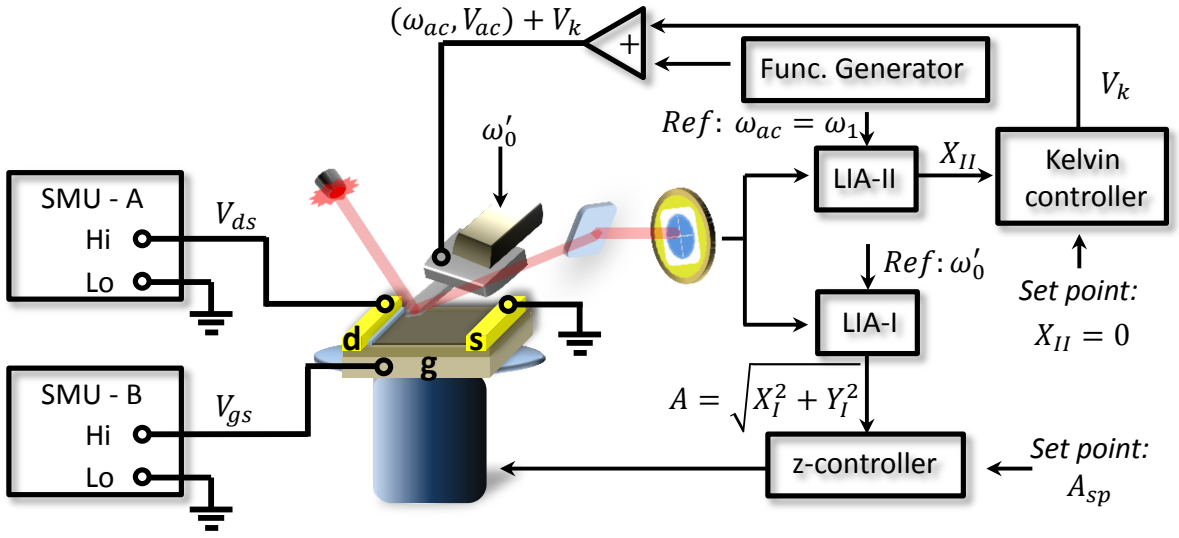

Figure 3.10: KPFM amplitude modulation setup at the second resonant frequency for the analysis of operating devices. Drain, source and gate contacts are indicated as d, s and g, respectively.

AM- versus FM-KPFM

KPFM can also be operated in frequency modulation (FM) mode. Here, the gradient of the electrostatic force component at ω_{ac} ($\partial\vec{F}_{\omega_{ac}}/\partial z$) is detected instead of the force $\vec{F}_{\omega_{ac}}$ itself, by means of the frequency shift of the fundamental resonance frequency Δf_0 caused by the modulating AC signal [12], as seen in Equation 3.11. Thus, the frequency shifts are related to the force gradient as,

$$\Delta f_{0(\omega_{ac})} \propto \left| \frac{\partial \vec{F}_{\omega_{ac}}}{\partial z} \right| = -\frac{\partial^2 C}{\partial z^2} \left(V_k + V_{CPD}\right) V_{ac} sin\left(\omega_{ac} t\right) \tag{3.24}$$

In a common FM-KPFM setup this is detected by a LIA using ω_{ac} as the reference frequency and as input Δf_0. In Figure 3.11a simulations of the tip apex, cone and cantilever contributions to the first order of capacitance gradient ($\vec{F}_{\omega_{ac}}$ in AM) and in Figure 3.11b for the second order of capacitance ($\partial\vec{F}_{\omega_{ac}}/\partial z$ in FM) are shown as a function of distance of a mechanical oscillation amplitude (solid lines). [122].

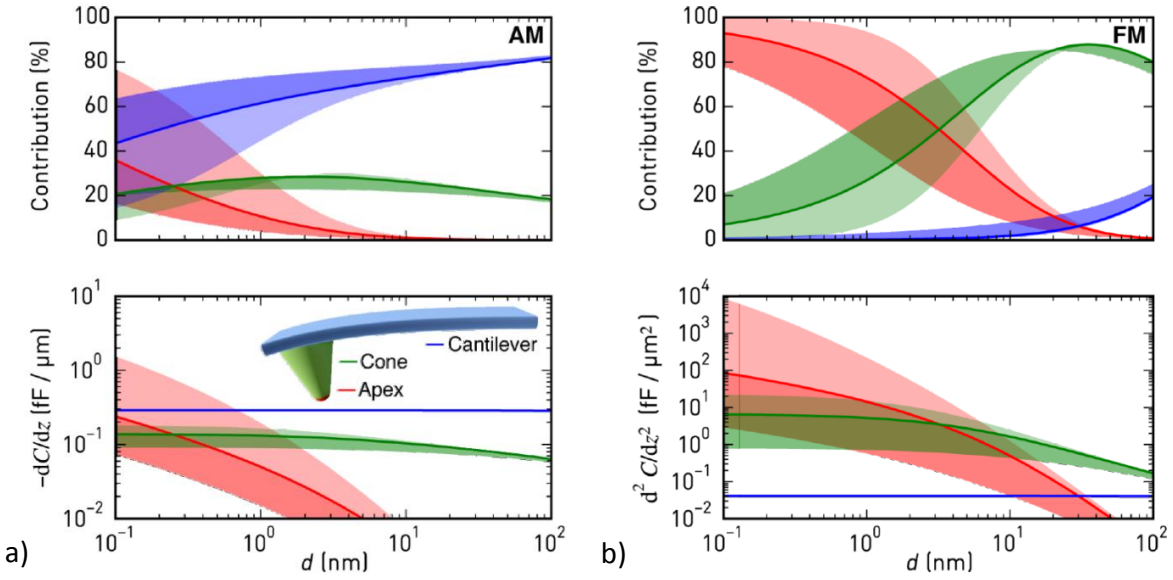

Figure 3.11: Calculated contributions of the tip apex, cone and cantilever for (a) AM and (b) FM operation modes as a function of distance. The shaded areas represent variations of the mechanical amplitude. Image taken from [122].

In these simulations, it can be noted that for AM-KPFM at the range of tip-sample distances with which intermittent contact (tapping) mode works, i.e. fractions of nm up to tens of nm, a large contribution percent comes from the cantilever and cone. For FM-KPFM this contribution is drastically reduced and the main contributor at small

d is the tip apex. Hence, the advantage of the gradient force measurement instead of the electrostatic force measurement is clear. However, the direct implementation of FM-KPFM has the requirement of the Δf_0 which is obtained by the instrumentation of FM-AFM setups, usually operating at high vacuum conditions [116]. As it will be seen in chapter 4, a solution for the measurement of the electrostatic force gradient in ambient AM-AFM operation is the detection of the phase shifts of the cantilever's oscillation frequency. To clarify, while KPFM can be operated in vacuum conditions using both amplitude and frequency modulation [12], the use of AM-AFM in vacuum conditions is not advised due to the slow response of the change in the cantilever oscillation imposed by the decrease of damping in the cantilever [116].

KPFM voltage drop analysis of operational devices

This non-conventional electrical characterization technique has been applied to study the voltage distribution in light emitting diodes [123], lasers [124] [125], silicon nanowires [126], organic electronic devices [127] and perovskites solar cells [128]. This analysis is based on mapping the surface potential of the device under operating conditions, and comparing it to the values at zero voltage bias. The calculations of ρ_s and ρ_c from KPFM voltage drop analysis are described next.

First, the components of the device (drain, channel and source) are defined as resistors in series, and thus all resistances share the same amount of I_{ds}. It is then expected that a corresponding drop of the applied V_{ds} along the device would correspond to variations in conductivity. To determine the voltage drops KPFM analysis are done at $V_{ds} = 0$ V and $V_{ds} \neq 0$ V. The KPFM information of the device at zero bias voltage (intrinsic ϕ) is an offset incorporated in the KPFM map of the device analyzed at V_{ds} and must be subtracted. It is assumed that although changes in the dielectric substrates potential, reacting to the applied V_{ds} can be seen, these do not contribute to the conductivity of the devices. Thus, out of the KPFM map, information is extracted in the form of line profiles (Figure 3.12), e.g. fixing a vertical position y and extracting the horizontal information along x. By subtracting the line profiles without bias voltage ($V_k^{0V}(x)$) from those done under voltage bias ($V_k^{ds}(x)$) , the offset (material information) is removed and only the voltage drop along the specified selection remains such as

$$V_{drop}(x, y) = V_k^{ds}(x, y) - V_k^{0V}(x, y) \tag{3.25}$$

The local voltage drops at the channel and contact interfaces, which correspond to R_s and R_c, are then defined by comparison with the corresponding topography information. The height profile, which is taken simultaneously in single-pass KPFM, can be extracted in a similar fashion. The voltage drops profiles can be then related to the device′s components by comparing directly against the topography profiles. Using Ohm′s law and normalizing by device′s geometrical dimensions, ρ_s and ρ_c can be obtained for graphene devices as

$$\rho_s = R_s \frac{w}{l} = \left(\frac{V_{drop}(x_n, y) - V_{drop}(x_{n+m}, y)}{I_{ds}} \right) \frac{w}{l} \tag{3.26}$$

$$\rho_c = R_c w = \left(\frac{V_{drop}(x_n, y) - V_{drop}(x_{n+m}, y)}{I_{ds}} \right) w \tag{3.27}$$

Due to technology constraints the devices′ nominal dimensions might deviate from the real measured ones, thus AFM measurements provide more precise information for the calculations. Furthermore, the visualization of the device at such a scale can provide information such as integrity of the channel, extent of electrode/material connection over its width, visualization of damaged areas and/or debris over the contact or channel, which might be responsible for the device behavior. Thus, voltage drops can be identified along the length (l) and width (w) of the device with a nanometric spatial resolution without the need of more than a pair of contacts.

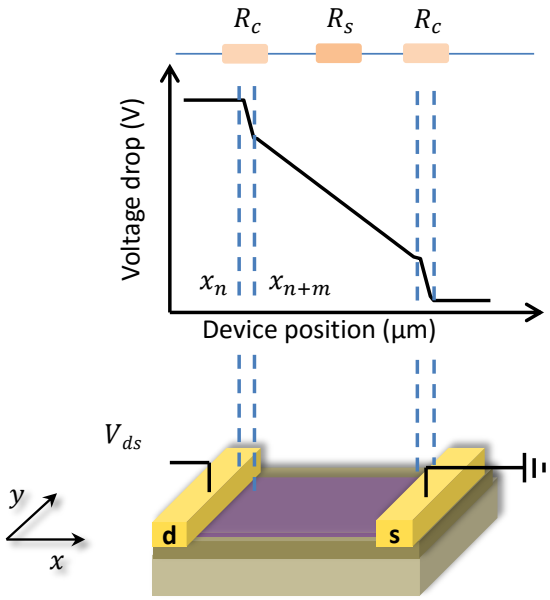

Figure 3.12: Diagram of a basic device (bottom) configuration seen as three resistors in series (top) each having a corresponding voltage drop (middle) along the contact interfaces and device channel.

3.2.8 AFM/KPFM instrumentation

For the AFM/KPFM measurements in this work, two different systems were used, namely the *Veeco Innova* SPM system and the *NT-MDT Ntegra Spectra* SPM system. Both instruments have differences from its commercial counterparts, as they were customized to meet the requirements of this workgroup. The *Veeco Innova* is delivered with built-in measurement and control units for KPFM. However, this was modified to extract the necessary signals for the measurement and control, with external dedicated units, of AM-KPFM. The *NT-MDT Ntegra Spectra* SPM system, as it will be seen later, is capable of stand-alone optical measurements as well as simultaneous AFM/optical analysis.

Veeco SPM system

In Figure 3.13a the *Innova* SPM system from *Veeco* instruments (now *Bruker*) can be seen. It has a scanning range area of 100 μm x 100 μm and 7.5 μm in the vertical range, with up to 1024 pixels per line. The scan rate reaches from 0.1 Hz to 100 Hz, i.e. 0.1 to 100 lines per second and 360^o scan rotation. The scan direction is fixed from left to right and top to bottom. The engage controls are done coarsely by the head motors and fine by the piezoelectric tube. In the measuring head (Figure 3.13b), a diode laser is used for the detection of the cantilever oscillations with a maximum output of 0.2 W in the wavelength range of 600 to 700 nm, as stated by the company. The QPD can detect frequencies from 0 to 1 MHz. The laser and QPD are aligned horizontally with an angle. It has two full digital LIAs available. Although this system itself had the KPFM option built-in, it was replaced by a homemade setup which consists of an external signal generator, LIA and PI controller [129]. This modification allows adjusting the feedback electronics at the desired frequency of operation.

For AM-KPFM measurements at f_1 a *Stanford Research* lock-in amplifier model SR844 is used, with a frequency range from 25 kHz to 200 MHz, a phase resolution of 0.02^o, a full-scale sensitivity of 100 nV to 1 V and a time constant of 100 μs to 30 ks. The sinusoidal signal at f_1 sent to the tip and to the LIA as the reference signal is generated by a signal generator *Stanford Research Systems* DS345.

NT-MDT SPM system

The *Ntegra Spectra* SPM system from *NT-MDT* can be seen in Figure 3.14a. It has a scanning range area of 120 μm x 120 μm and 9 μm in the vertical range, with up to 4000 pixels per line. The scan rate reaches from 0.5 Hz to 50 Hz and scan rotation from

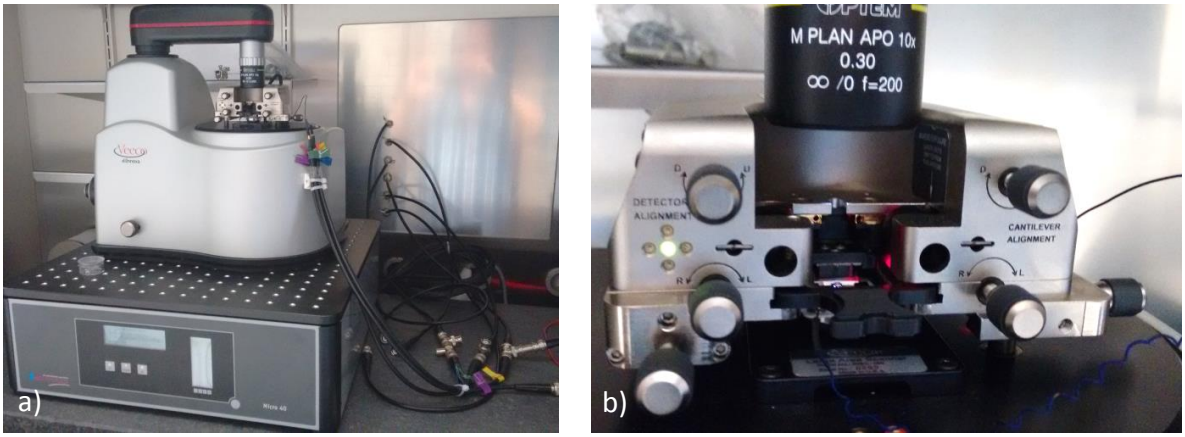

Figure 3.13: Optical images of the (a) SPM system and the (b) measuring head of the *Veeco Innova* system.

-45^o to 45^o is possible. In addition, several scan directions can be selected e.g. scans from bottom to top, from right to left. The coarse and fine engage commands, for the tip-sample distance, are controlled by the scanner stage while the head and tip are fixed at a specific height. The detection of the cantilever deflection is performed through a semiconductor laser diode of 650 nm wavelength. The QPD has a bandwidth from 0 to 5 MHz. The laser and QPD are aligned vertically. Integrated are two analog and three digital LIAs with three signal generators. Two signal generators, bounded to the analog LIAs, are capable of up to 1 V_{p-p} and frequencies up to 5 MHz. One digital LIA has a dedicated signal generator as the modulation voltage with up to 5 V_{p-p} for frequencies between 0.1 and 10 kHz. The system has interchangeable SPM heads for different purposes. For example, the universal SPM head (Figure 3.14b) can perform topography, tunneling microscopy, conductive AFM, thermal microscopy and KPFM measurements. While the optical/AFM head (see subsection 3.3.2) can implement topography, KPFM, near-field optical microscopy, photoluminescence, Raman and Tip-enhanced Raman measurements.

a) 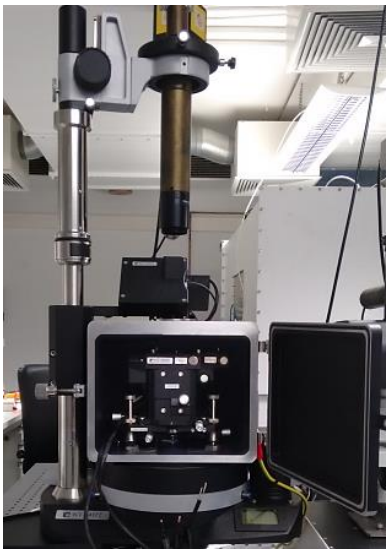

b) 

Figure 3.14: Optical images of the (a) SPM setup and (b) universal head of the *NT-MDT Ntegra Spectra* system.

3.3 Raman spectroscopy

Raman spectroscopy is a technique sensitive to vibrational and rotational transitions of molecules and groups of arranged atoms as in the crystal lattice of graphene. Before reviewing the specifics of Raman spectroscopy in graphene, the Raman process will be analyzed for the case of a diatomic molecule.

If the molecule is irradiated by a photon source with frequency ν_0, the light can be elastically (Rayleigh) or inelastically (Raman) scattered (Figure 3.15a). Rayleigh scattering is strong and the frequency (ν_0) of the photon is conserved. The Raman scattering of light is weak and here the frequency of the photon is not conserved ($\nu_0 \pm \nu_m$) due to interactions of the light with the vibrational states with frequency ν_m, of the molecule. If a reduction in the frequency of the scattered light is detected this is known as a Stokes shift ($\nu_0 - \nu_m$). If the scattered light has increased its frequency it is known as an anti-Stokes shift ($\nu_0 + \nu_m$). These interactions are illustrated in Figure 3.15b.

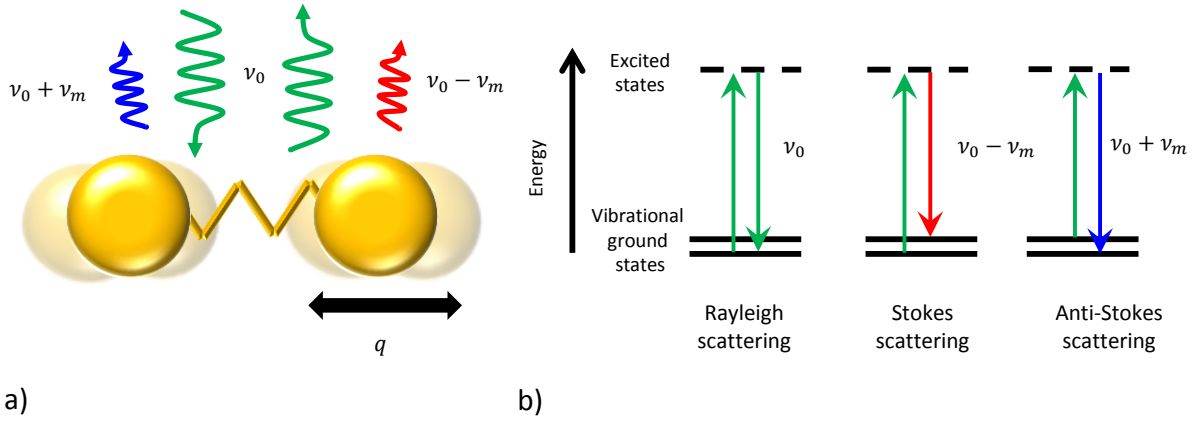

Figure 3.15: (a) Scheme of an incident photon altering the vibrational and rotational energy states of a diatomic molecule and (b) energy level diagram of the possible scattering processes when an incident photon excites a molecule.

For a correct measurement of the type of shift, the photons interacting with the material must be of a single frequency, i.e. monochromatic. Therefore lasers are used as the source for the incident photons [130]. For the measurement of the vibrational states by means of the Stokes and anti-Stokes shifts it must be noted that while the equations development is done with photon frequencies ν, measured in Hz, vibrational spectroscopies

commonly uses the wavenumber $\tilde{\nu}$, in cm^{-1} units for its representation, where

$$\tilde{\nu} = \frac{\nu}{c} \tag{3.28}$$

where c is the speed of light.

A diatomic molecule can be irradiated with a laser radiation of frequency (ν_0) and a time (t) varying electric field strength, E, such as

$$E = E_0 cos\,(2\pi\nu_0 t) \tag{3.29}$$

where E_0 is the electric field amplitude of the laser radiation.

As the laser irradiates the diatomic molecule, an electric dipole moment P is induced:

$$P = \alpha E = \alpha E_0 cos\,(2\pi\nu_0 t) \tag{3.30}$$

where α is the polarizability.

The natural vibration of the diatomic molecule at frequency ν_m creates an oscillating displacement (q) of the atoms as illustrated in Figure 3.15, which can be represented as

$$q = q_0 cos\,(2\pi\nu_m t) \tag{3.31}$$

where q_0 is the vibrational amplitude.

In the simple case, for a small amplitude of vibrations, α is a linear function of q, such that

$$\alpha = \alpha_0 + \left(\frac{\partial\alpha}{\partial q}\right)_0 q \tag{3.32}$$

where α_0 is the polarizability at the equilibrium position of the molecule′s vibration, and $(\partial\alpha/\partial q)_0$ is evaluated at this equilibrium position. Substituting Equation 3.31 and Equation 3.32 in Equation 3.30,

$$\begin{aligned} P &= \alpha E_0 cos\,(2\pi\nu_0 t) \\ &= \alpha_0 E_0 cos\,(2\pi\nu_0 t) + \left(\frac{\partial\alpha}{\partial q}\right)_0 q E_0 cos\,(2\pi\nu_0 t) \\ &= \alpha_0 E_0 cos\,(2\pi\nu_0 t) + \left(\frac{\partial\alpha}{\partial q}\right)_0 q_0 E_0 \left[cos\,(2\pi\nu_0 t)\, cos\,(2\pi\nu_m t)\right] \end{aligned} \tag{3.33}$$

Using trigonometric identities,

$$P = \alpha_0 E_0 cos\left(2\pi\nu_0 t\right) + \frac{1}{2}\left(\frac{\partial\alpha}{\partial q}\right)_0 q_0 E_0 \left\{cos\left[2\pi\left(\nu_0 + \nu_m\right)t\right] + cos\left[2\pi\left(\nu_0 - \nu_m\right)t\right]\right\} \quad (3.34)$$

Hence, in Equation 3.34, the Rayleigh scattering, Stokes and Anti-stokes shifts are visible in the right part of the equation. A schematic example of a Raman spectra can be seen in Figure 3.16, where the Rayleigh scattering (green shade) is represented in the first term of the equation. The second term corresponds to the anti-Stokes $(\nu_0 + \nu_m)$ Raman shift (blue shade) and Stokes $(\nu_0 - \nu_m)$ Raman shift (red shade) [131].

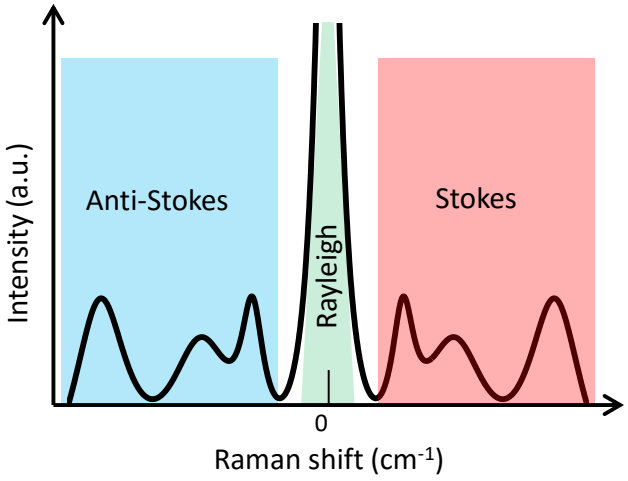

Figure 3.16: Exemplification of the Rayleigh scattering and the Stokes and anti-Stokes shifts in a Raman spectra.

Even with the use of a high-intensity excitation source such as the laser, the Raman scattering is very weak compared to the reflection of the laser on the sample (Rayleigh scattering). To separate these two signals, edge filters, notch filters or triple monochromators are used to attenuate the signal from the laser. With edge filters it can be measured closer to the laser line, while with notch filters Stokes and Anti-Stokes signals can be detected. After filtering, the detection is usually done by charge-coupled devices (CCD) due to their high sensitivity compared to photomultipliers [132].

3.3.1 Raman shift of graphene

The use of Raman spectroscopy for the study and characterization of graphene, graphite and other carbon materials has been extensively studied in literature [133, 134, 135, 136]. The highly ordered honeycomb structure of sp^2 carbon to carbon bonds of graphene has

more complex atom-group vibrations, addressed as normal modes. These Raman active normal modes present peaks which are widely used for the characterization, between others, of the number of layers, doping and defects [137, 138].

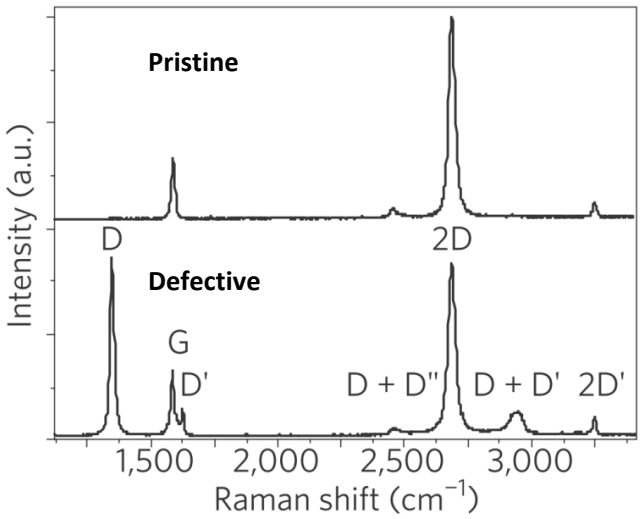

Figure 3.17: Raman shift spectra of non-defective graphene (pristine) and defective graphene. Most widely used for characterization are the D-, G- and 2D-mode peaks, seen around ∼1350, ∼1580 and ∼2700 cm^{-1}, respectively. Image adapted from [137].

The Raman shift range used for graphene extends approximately from 1100 to 3300 cm^{-1}. As seen in Figure 3.17, in this range all identified graphene characteristic peaks can be found. The most widely used and prominent features in literature, as well as in this work, are the D-mode peak (from disorder) at ∼1350 cm^{-1} which accounts for the breathing modes of six-atom rings and requires a defect for its activation, the G-mode peak (from graphite) at ∼1580 cm^{-1} corresponding to the high frequency normal mode at the center of the Brillouin zone and the 2D-mode peak at ∼2700 cm^{-1} which is the overtone of the D-mode peak.

In Figure 3.18a and Figure 3.18b, the schemes of the vibrations for the G- and D-mode of graphene are shown. The 2D-mode, although it is an in-plane mode, is sensitive to the number of layers, since the resonant Raman mechanism that gives rise to it is closely related to the electronic band structure. As the electronic band structure changes with the number of layers and the layer′s relative orientation, it is therefore used to identify the number of layers usually through the 2D- to G-mode peak (2D/G) ratio [137, 138].

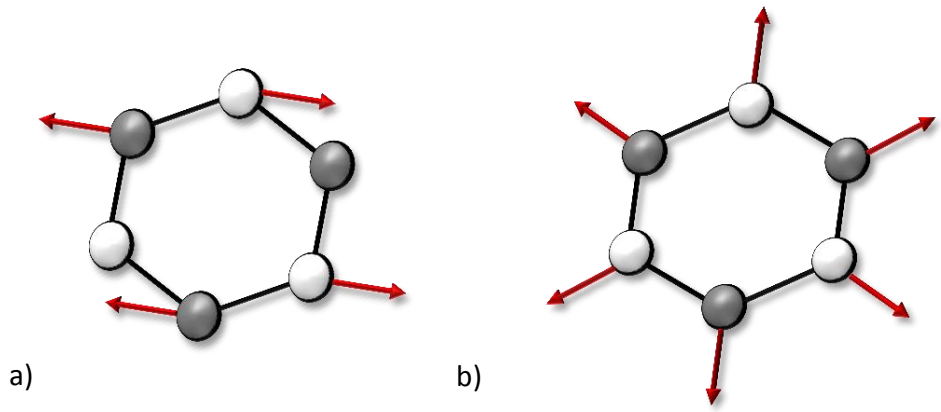

Figure 3.18: Normal modes for the (a) in-plane phonon displacement at ∼1580 cm^{-1} (G-peak) and (b) atom displacement breathing mode of the six-atom rings of graphene at ∼1350 cm^{-1}. The 2D-mode peak is an overtone of the latter and is sensitive to the number of layers.

3.3.2 NT-MDT Ntegra Spectra Optical/AFM

The *NT-MDT Ntegra Spectra* has the possibility to perform optical measurements inside and outside the SPM system. For the optical measurements inside the SPM system a high performance optical/AFM measuring head (Figure 3.19a) is used, instead of the universal SPM head shown before. The characteristics of this head, along with the spectrometer instrumentation, can provide a spatial resolution down to 0.5 μm in optical measurements.

The main component of the optical/AFM measuring head is the high numerical aperture (0.7) *Mitutoyo M* Plan Apo 100 lens. It has a focal length of 2 mm, a visual field of 80 μm and a working distance of 6 mm, through which the AFM and other lasers are delivered and their response collected. The xyz-sample motor and scanning area for the optical/AFM measurements are the same as the SPM system described above (120 μm x 120 μm x 9 μm). An isolation chamber can be used to reduce ambient light and noise sources. A front view scheme of the system can be seen in Figure 3.19b, which can be compared to the optical image in Figure 3.14a. A second motor is available only for optical measurements, which controls the xy-position of a mirror. The mirror scanner is inside of the diffraction module (Figure 3.19c) and has a scanning range area of 52 μm x 52 μm, up to 4000 pixels per line, a scan rate of .0005 to 500 Hz and free selection of the scan direction. The mirror motor is used to position the laser independent of the position of the sample motor. Thus the sample can be analyzed without moving the sample and/or, if needed, to focus the laser to a specific point. Such case is mainly for measurements where

the laser needs to be focused at the end of the AFM tip. Thus, this setup provides the capability of simultaneous optical and AFM measurements such as topography, Raman measurements or more sophisticated like Tip-enhanced Raman Spectroscopy or Scanning Near-field Optical Microscopy.

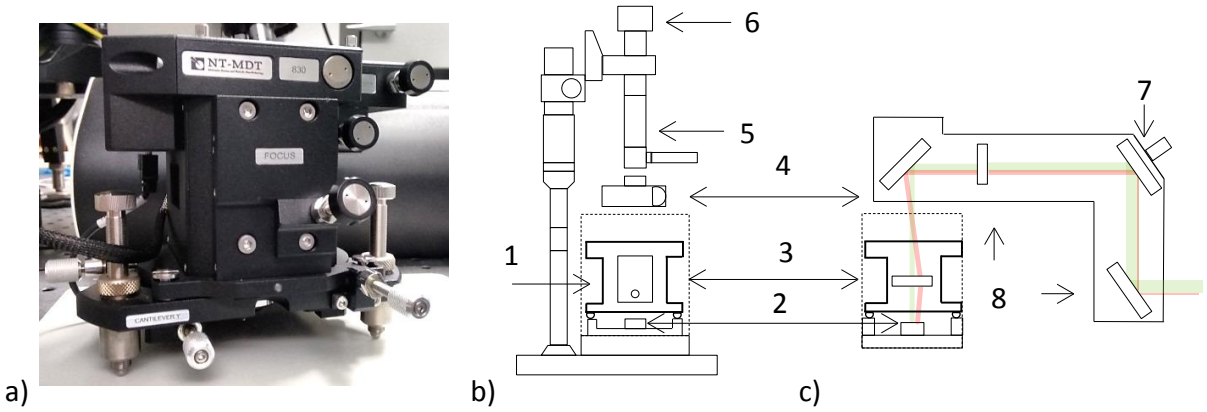

Figure 3.19: The (a) optical/AFM head and (b) front view and (c) side view diagrams of the optical/AFM setup. Here are visible the (1) optical head, (2) xyz-sample motor, (3) isolation chamber, (4) diffraction module, (5) lamp and digital camera lenses, (6) digital camera, (7) xy-mirror motor and (8) aligning mirrors.

The detection of the sample′s optical response is done by a 1024 x 25 pixels *ANDOR* CCD camera with built-in Peltier element to cool down the CCD-matrices to -90^{o}C in order to reduce thermal noise. The laser line is attenuated by a *Semrock, Inc.* edge filter. The system has 3 lasers at dispose for different wavelengths: 325 nm, 405 nm and 532 nm. For the Raman spectroscopy analysis of graphene samples and devices only the 532 nm solid state laser was used. The laser is delivered to the spectrometer through a single-mode optical fiber and is linearly polarized with a maximum power of 20 mW.

Chapter 4

Phase sensitive detection of the force gradient for KPFM

This chapter presents the implementation and measurement results of phase modulation (PM-) KPFM on an already operating AM-KPFM system. While FM-KPFM uses the frequency shifts of the mechanical oscillation to detect the force gradient, PM-KPFM uses the phase shifts for the same purpose. First, it will be discussed how the detection of phase shifts are related to the already available theory in FM-KPFM. It will be explained how the cantilever′s mechanical oscillation carries the electrostatic force information in its phase signal along with the description of the inputs and outputs of the Lock-In Amplifiers (LIA) to extract the relevant information for single pass PM-KPFM. Following, the exact technical implementation in an operating *Veeco Innova* system, including the equipment employed and its working parameters will be described. Afterwards, the importance of the correct adjustment at the LIA outputs for the precise measurement of the CPD is explained. The chapter continues with the results of the grounding configurations and their significance in the interpretation of the results, and how, for the purposes of this investigation, the sample-grounded configuration is the only option. Furthermore, the improvement of PM-KPFM over AM-KPFM will be demonstrated, with a comparison of the KPFM voltage drop analysis results obtained by both modulations. To conclude this chapter, the reliability of PM-KPFM voltage drop analysis for the electrical characterization of the devices is verified by comparing its results to those of the macroscopic 4p probe method.

4.1 Development of PM-KPFM

As mentioned in subsection 3.2.7, the gradient detection of $\vec{F}_{\omega_{ac}}$ shows an improvement over the detection of the electrostatic force itself for KPFM measurements by reducing the contribution of cantilever and cone to the overall signal. The tip-sample interactions cause a frequency shift of the fundamental oscillation frequency Δf_0 which is related to the force gradient $\partial\vec{F}_{ts}/\partial z$. In FM-AFM operation, the Δf_0 is directly obtained, since the oscillation frequency of the cantilever is varied to maintain the oscillation amplitude constant and thus, can be directly used for FM-KPFM by detecting the oscillations of the frequency shift $\Delta f_0(\omega_{ac})$ at ω_{ac}. Since in AM-AFM the oscillation frequency is maintained constant, the phase shift of the oscillation frequency ($\Delta\theta_0$) can be used to retrieve the force gradient $\partial\vec{F}_{\omega_{ac}}/\partial z$. Thus by demodulating the phase shift oscillations at ω_{ac}, $\Delta\theta_0(\omega_{ac})$, the amplitude of the electrostatic interactions can be obtained for the correction of the CPD during KPFM operation.

Using the harmonic approximation [139], which assumes that the vibration of the cantilever is harmonic and Δk and $\Delta\omega$ shifts are small compared to k and ω, respectively, the phase shift ($\Delta\theta_0$) can be related to Δf_0 at the resonance frequency [140] by:

$$\Delta\theta_0 = \frac{\pi}{2} - arctan\left(\frac{\omega_0}{2Q\Delta\omega_0}\right) \approx 2Q\frac{\Delta\omega}{\omega_0} \tag{4.1}$$

or

$$\frac{\Delta\theta_0}{2Q} \approx \frac{\Delta f_0}{f_0} \tag{4.2}$$

Due to the non-linear relation of the phase with respect to frequency, the proportionality in Equation 4.2 holds true only at the regime of low frequency shifts, i.e. $\Delta f_0 < f_0/2Q$ [141].

To ascertain that the general case of the AFM/KPFM setup is indeed in the low frequency shift regime, the quality factor Q must be stated. The value of Q is in function of the resonance frequency bandwidth (B), as

$$\frac{Q}{f_0} = \frac{1}{B} \tag{4.3}$$

To obtain B, a spectrum analyzer is used for the QPD signal of the usual tip used throughout this investigation (Budget sensors Multi 75E coated with Cr/PtIr). The bandwidth is defined here as the frequency difference between the lower and upper

frequency where the signal of the cantilever's mechanical oscillation losses half of its power (Figure 4.1a). Hence, for a mechanical resonance at 66.3 kHz, a value for the bandwidth is calculated to be $B \sim 0.4$ kHz. Thus, the quality factor has a value of $Q \sim 165$, which correlates with values in literature for ambient conditions [142]. This result establishes that Δf_0 must not exceed 0.2 kHz for a linear relation between phase and frequency shifts.

The resonance frequency shift influenced partially by the electrostatic force and detected by the alternating electric field V_{ac} causes sidebands (satellite peaks) around the mechanical oscillation frequency. The modulation index of the frequency modulation signal, defined as $\Delta\omega_0/\omega_{ac}$, is in direct relation to the number of sidebands to expect and is defined as the ratio of the frequency shift and the modulating signal. If the modulating index is < 0.5, sidebands can be expected at $\omega_0 \pm \omega_{ac}$ and $\omega_0 \pm 2\omega_{ac}$, as depicted in Figure 4.1b.

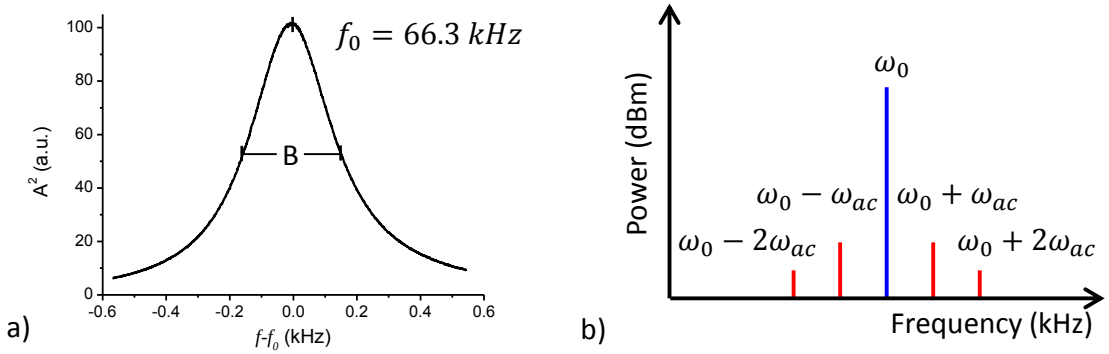

Figure 4.1: (a) Resonance spectra of the AFM tip and its bandwidth. (b) Expected frequency spectra of frequency modulated signal where $\omega_0 \gg \omega_{ac}$

Thus, if the AFM/KPFM setup operates in the low frequency shift regime with a linear relation of $\Delta\theta_0$ and Δf_0, the frequency modulation equation for the detection of the force gradient can be recast as

$$\Delta\theta_0(\omega_{ac}) \propto \Delta f_0(\omega_{ac}) \propto \left|\frac{\partial \vec{F}_{\omega_{ac}}}{\partial z}\right| = -\frac{\partial^2 C}{\partial z^2}(V_k + V_{CPD})V_{ac} sin\,(\omega_{ac} t) \tag{4.4}$$

Hence the phase shifts of the mechanical oscillations caused by electrostatic interactions $\Delta\theta_0(\omega_{ac})$ can be used for the detection of $\partial\vec{F}_{\omega_{ac}}/\partial z$.

The detection of $\Delta\theta_0$ can be thus achieved by means of the phase sensitive lock-in amplifier (LIA-I) used for the topography channel while the detection of the electrostatic

interactions with a second LIA (LIA-II) connected in series. In LIA-I, the reference signal $s_{Ref}(\omega_0^{'})$ will be multiplied with the QPD signal where the tip-sample interactions $\vec{F}_{ts}(z, \omega_0^{'})$ are embedded

$$\vec{F}_{ts}(z, \omega_0^{'}) = \vec{F}(z_0) + \left.\frac{\partial \vec{F}_{ts}}{\partial z}\right|_{z_0} (z(t) - z_0) \tag{4.5}$$

where the function $z(t)$ describes sinusoidal motion of the cantilever with amplitude A and frequency $\omega_0^{'}$ around the tip-sample distance z_0, as

$$z(t) = z_0 + Asin\left(\omega_0^{'} t\right) \tag{4.6}$$

Due to the orthogonal nature of sinusoidal waves, from the mix of the two frequencies at LIA-I, all signals different from $\omega_0^{'}$ will be attenuated. The output is an in-phase component (X_I) and a quadrature component (Y_I),

$$\vec{F}_{ts}(\omega_0^{'}) s_{Ref}(\omega_0^{'} t) \Rightarrow X_I = k_{LIA} V_{sig} cos(\theta) \tag{4.7}$$

$$\vec{F}_{ts}(\omega_0^{'}) s_{Ref}(\omega_0^{'} t + 90^o) \Rightarrow Y_I = k_{LIA} V_{sig} sin(\theta) \tag{4.8}$$

where k_{LIA} is a scaling factor of the LIA and V_{sig} is the r.m.s LIA value of the measured signal

$$V_{sig} \sim Asin\left(\omega_0^{'} t\right) \left|\frac{\partial \vec{F}_{ts}}{dz}\right| \tag{4.9}$$

Here it is clear that both X_I and Y_I components are proportional to the derivative of the force [143]. This signal can be then used as the input of LIA-II tuned to w_{ac} to extract the amplitude of electrostatic force gradients

$$Y_I \propto \frac{\partial \vec{F}_{ts}}{\partial z} \propto \frac{\partial \vec{F}_{\omega_{ac}}}{\partial z} \tag{4.10}$$

By correctly adjusting the phase of the LIA-II to zero, the in-phase component X_{II} should be proportional to the amplitude of the sidebands, which by the correction of the V_k voltage of the Kelvin controller should nullify the amplitude of the sidebands.

If the setup indeed operates with a linear relation of the phase and frequency shifts and the considerations shown above are correctly implemented, the appearance of the sidebands near ω_0 and the nullification of its amplitude by V_k can be expected. In

Figure 4.2a, the frequency spectrum of an engaged metal coated tip can be seen, while the Kelvin controller is turned off. The mechanical oscillations frequency has the sidebands at $\omega_0^{'} \pm \omega_{ac}$ and $\omega_0^{'} \pm 2\omega_{ac}$, as expected for a low modulation index and small frequency shifts. Indeed, as the Kelvin controller is turned on, the amplitude of the sidebands is minimized (Figure 4.2b), accounting for the correct detection and nullifying of $\partial\vec{F}_{\omega_{ac}}/\partial z$ by means of $\Delta\theta_0$.

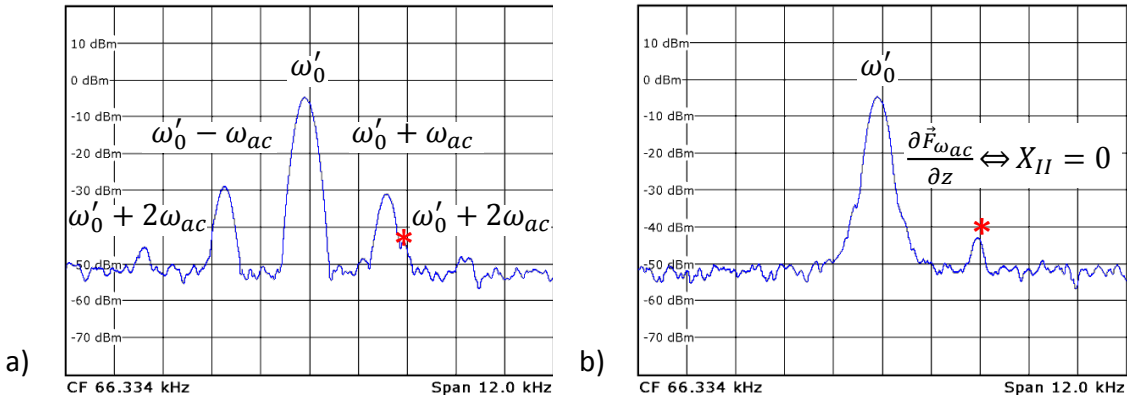

Figure 4.2: Frequency spectra of an engaged Cr/PtIr coated tip showing the presence of satellite peaks as the Kelvin controller is turned off. (b) The nullifying of the satellite peaks as the Kelvin controller is turned on, evidencing the working setup of the PM-KPFM. The red asterisk shows a natural peak of the tip, not related to the electrostatic forces.

4.2 Technical implementation of PM-KPFM

For the sensing of the electrostatic force gradient in single pass PM-KPFM, an external *Stanford Research* Digital Signal Processing Lock-In Amplifier (LIA-II) model SR830 is connected in series to the internal Lock-In Amplifier (LIA-I) inside the *Veeco Innova* system. The model SR830 has a phase resolution of 0.01^o, a full-scale sensitivity of 2 nV to 1 V and a time constant of 10 μs to 30 s. It differs from the LIA used for AM-KPFM (see Figure 3.10), by having a frequency range from 1 mHz to 102 kHz, which allows to demodulate at $\omega_0 \gg \omega_{ac}$ and stay within the topography LIA's low pass filter bandwidth [144].

The block diagram of the setup is shown in Figure 4.3. The PM-KPFM loop starts at the tip while it interacts with the sample. The QPD signal, which contains the topography information at $\omega_0^{'}$ and embedded in its phase shift the electrostatic forces gradient information at ω_{ac}, is fed to the built-in LIA-I. In LIA-I, the X_I and Y_I are used to obtain the amplitude A (magnitude) of the signal, which is sent to the topography z-controller to equal A_{sp}.

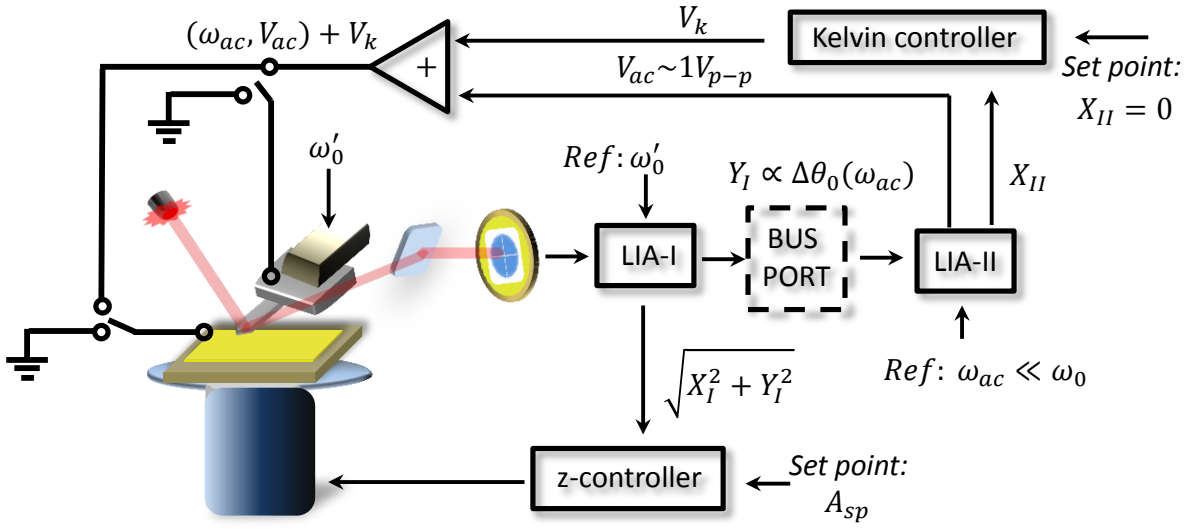

Figure 4.3: Block diagram for the implementation of PM-KPFM in a *Veeco Innova* SPM system.

The out-of-phase component Y_I carries the force gradient information and must be sent to LIA-II for demodulation. Using the open access hardware in the control software, the signal must be manually activated and sent to the internal BUS connectivity port of the *Innova* system. Through a BNC output, the analog signal is extracted and used as

the input of LIA-II.

Standard Cr/PtIr coated tips with f_0 ∼65 kHz, k = 48 N/m, ω_{ac} of 1.5 kHz and 1 V_{p-p} were used. The LIA-II filter parameters that render the best results for PM-KPFM in ambient conditions were a time constant of 100 μs with a roll-off of 18 dB/oct, full-scale sensitivity of 500 mV and low noise reserve. The internal oscillator of LIA-II was used as the reference for ω_{ac} and the source of V_{ac}. The X_{II} output is then fed to the Kelvin controller input, where V_{ac} and V_k are added and send back to the tip for the sensing and nullifying of the sidebands completing the PM-KPFM loop.

4.2.1 Ground dependence of KPFM measurements

For the KPFM analysis, it is required that either the sample or the tip has to be grounded while the $V_k + V_{ac}$ are applied to the opposite terminal (see Figure 4.3). The selection of the ground does not alter the principle of the technique: the electrostatic interactions, either being sensed by the force directly (AM-KPFM) or from its derivative (PM-KPFM), must be reduced to zero. However, depending on which end is grounded, the polarity of V_k and therefore of the data obtained is changed, which can lead to misinterpretation of the results. To corroborate the correct operation of the PM-KPFM setup, a gold sample was analyzed using both the tip and the sample as ground. The obtained results are discussed on the basis of changes in their E_F using simplified band diagrams to clarify their relative shifts and implications on the KPFM results. An aleatory 8 μm x 8 μm area on the gold surface was analyzed in ambient conditions with a 25 nm radius Cr/PtIr silicon probe (*Budget sensors*) and a V_{ac} = 1 V. The height map of the area is shown in Figure 4.4a and the height distribution in Figure 4.4b. This mostly flat surface with particles less than 100 nm in height (inset), was deliberately selected to prevent if any, topography cross-talk [145] and for orientation when comparing the following KPFM measurements.

First the *tip-grounded* setup is reviewed, i.e. the tip is grounded and $V_k + V_{ac}$ are send to the sample. The KPFM map of this setup can be seen in Figure 4.5a, and by direct comparison with Figure 4.4a, it can be observed how KPFM gives access to information not available by topography. The potential variations seen in the middle of the KPFM map, do not correlate with any topographic features. This can be caused by surface adsorbates or intrinsic changes in the Au surface [146]. However, in general, the KPFM map shows low variations for the V_k values, which are centered at positive values around 200 mV with a distribution of ±75 mV (Figure 4.5b). To validate the center value of the distribution a (KPFM) tip spectroscopy is performed, obtaining a value of 150 mV

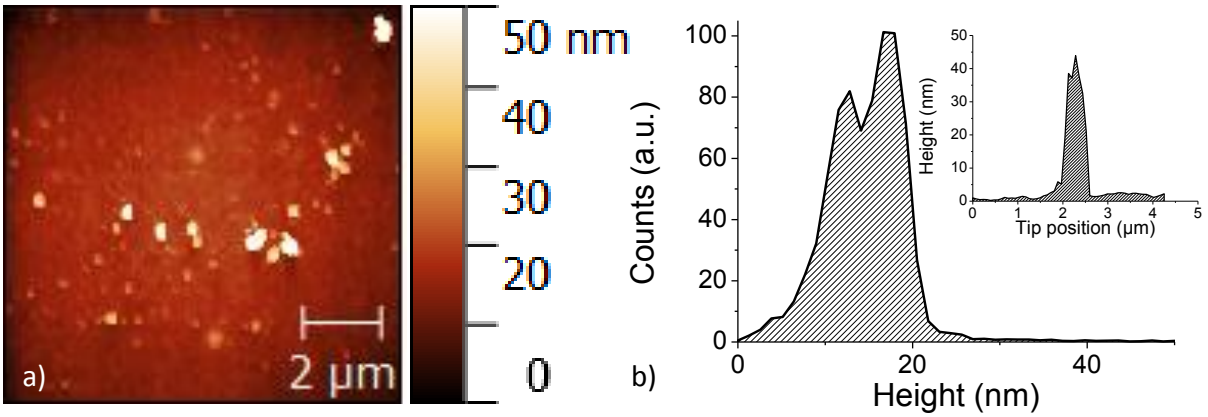

Figure 4.4: (a) Height map of a gold surface and its (b) height distribution histogram. Inset: Line profile over a topographic feature.

(inset). Tip spectroscopy is a punctual analysis done with the Kelvin controller turned off and consists of averaging several sweeps of V_k values, while tracking the response of X_{II}. The V_k value corresponding to the lower averaged X_{II} value represents the value at which the electrostatic force is minimized by compensating the CPD.

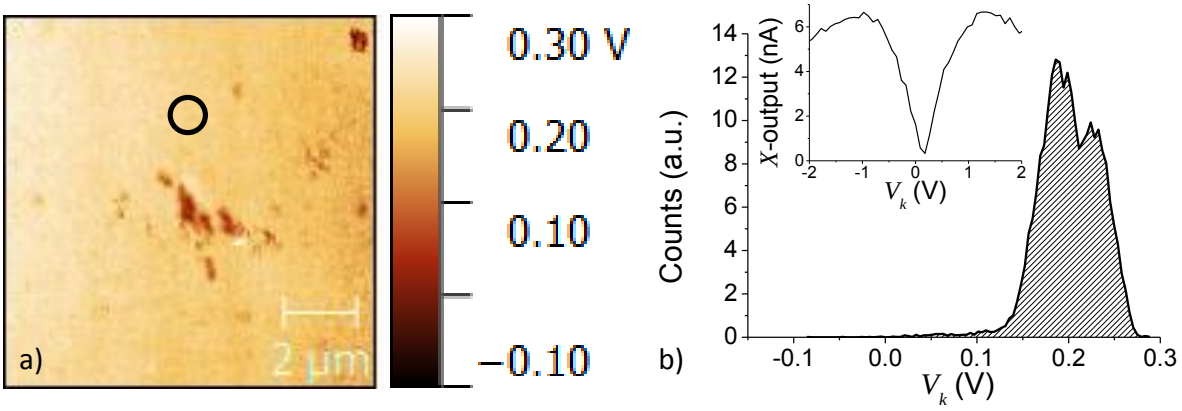

Figure 4.5: KPFM (a) map of the gold surface as the tip is grounded and (b) value distribution of this map. Inset: The valley of the tip spectroscopy is centered at $V_k = 150$ mV. The measurement position is marked in (a) by a circle.

In this setup, the value of V_k corresponds directly to the work function of the sample (ϕ_s) being greater by 150 mV to that of the tip (ϕ_t) and can be explained following the relative shifts E_F in the band diagrams of Figure 4.6. Since the tip is grounded, its Fermi level $E_{F,t}$ acts as the reference and is assumed as zero. It is clear from the work function difference that the Fermi level of the sample ($E_{F,s}$) lies below the reference $E_{F,t}$ before the

E_F leveling in the initial condition of KPFM. To correct the V_{CPD}, the position of $E_{F,s}$ has to be shifted downwards back to its original position. This is achieved by applying a positive voltage ($+V_k$) to the sample (black arrow in Figure 4.6b). Thus, the values in the KPFM maps, i.e. the polarity of V_k, in this setup will correspond directly to the work function of the sample with an offset equal to ϕ_t. Using a value for ϕ_t of 4.9 eV [147] to calculate ϕ_s results in 5.1 eV for this Au surface in ambient conditions, which fairly agrees with literature [148].

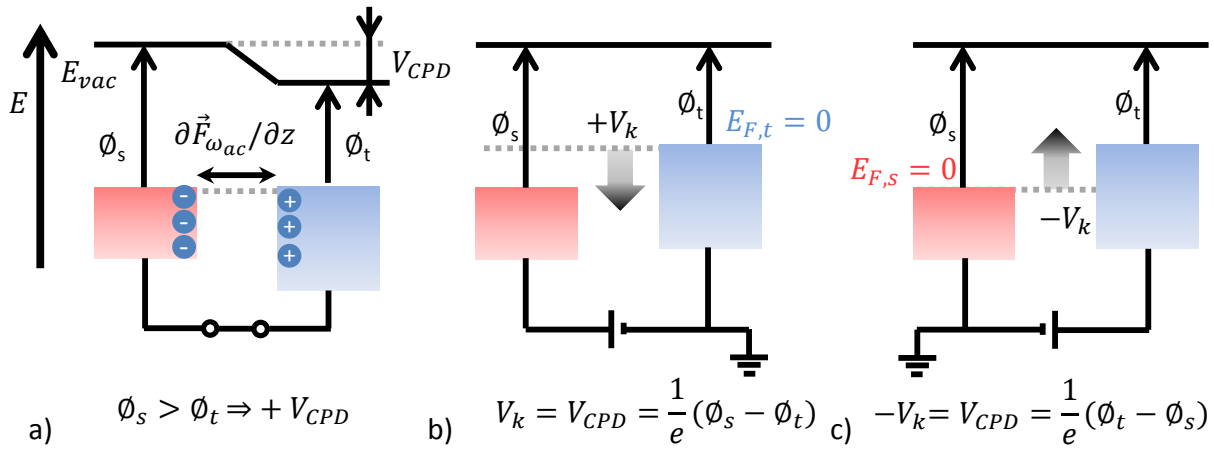

Figure 4.6: Band diagrams showing the correction of the (a) initial condition of KPFM, by the relative shifts of the materials E_F to nullify the force gradient using the (b) tip or (c) sample as ground

Next the *sample-grounded* setup is reviewed, i.e. the sample is grounded and the tip is receiving $V_k + V_{ac}$. Figure 4.7a shows the KPFM map centered nominally at the same position as in the analysis above. Compared to Figure 4.5, the same features are seen on the map with a clear change in its contrast over its surface. In Figure 4.7b the width of the V_k values distribution is ±75 mV and the spectroscopy shows us that the lowest value of the X_{II} corresponds to V_k = -140 mV, which is in agreement with the expected polarity change of the *tip-grounded* setup. In this setup, $E_{F,s}$ is the reference, thus its value is fixed at zero. By applying a negative V_k to the tip, the relative position of $E_{F,t}$ is increased (black arrow in Figure 4.6c) with respect to the sample causing again the nullifying of $\partial\vec{F}_{\omega_{ac}}/\partial z$. Therefore, for the KPFM analysis where the sample is grounded, the positive (negative) V_k values obtained in the map correspond to areas where ϕ_s is lower (larger) than ϕ_t. As the interest of this investigation is the voltage drops of operational devices, only the *sample-grounded* configuration can be used, since applying a DC voltage such as V_k to the sample would interfere with I_{ds} measurement during the KPFM analysis.

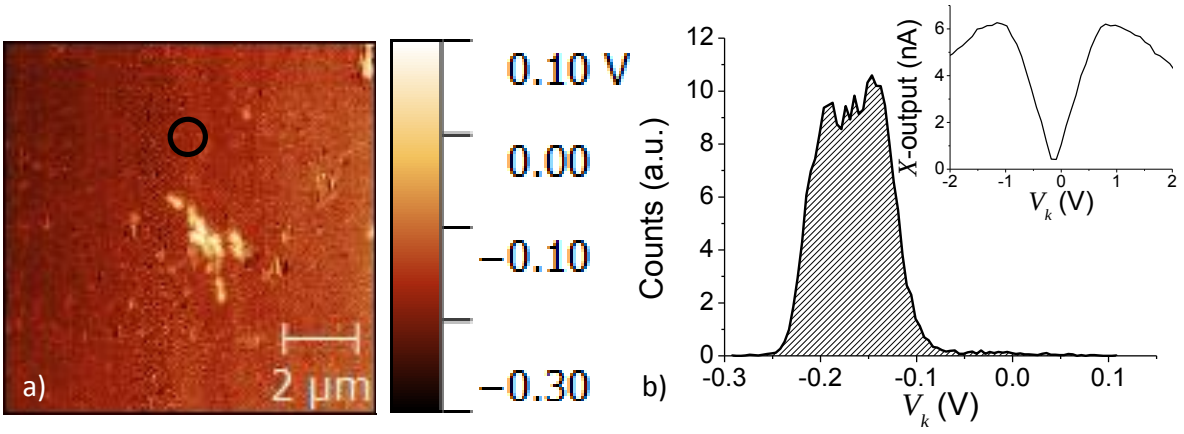

Figure 4.7: KPFM (a) map of the gold surface, as the system operates with the sample grounded. The (b) value distribution of this map follows the expected change in polarity in V_k values. Inset: The valley of the tip spectroscopy is centered at V_k = -140 mV. The measurement position is marked in (a) by a circle.

4.2.2 Resolution of PM-KPFM

To display the resolution achievable by PM-KPFM, the measurement done on a sample of graphene on Cu substrate is shown next. Graphene was grown by CVD on a polycrystalline Cu, sputtered on a SiO_2 substrate. This sample is chosen as it was observed that its surface offers a heterogeneous combination of features, for nominally the same material, with sharp changes which could be resolved [149]. In the topography map of a 1 μm^2 area of the sample (Figure 4.8a) a set of terraces can be seen. Although from a sputtered process a specific roughness of the whole sample is expected, at these dimensions these features might have their origin due to the growth of graphene as it is reported that its presence causes islands and valley topologies in the Cu surface [149].

The surface potential map of the same area is shown in Figure 4.8b. Here a heterogeneous surface potential can be clearly noted, many of them correlating with topography features. The independence of the KPFM measurement to topography can be evidenced with the feature inside of the dashed line box. In this area an explicit change of surface potential is visible which is clearly not resolved by neither topography nor the phase map (Figure 4.8c). The phase map consists of the recorded changes of the mechanical oscillation′s phase included those influenced by the electrostatic force (detected by ω_{ac}). The absence of any visible feature in the phase map of the dashed line box proves the actively and accurate correction of the phase changes caused by the

electrostatic interactions $\Delta\theta_{0(\omega_{ac})}$ as shown in section 4.1.

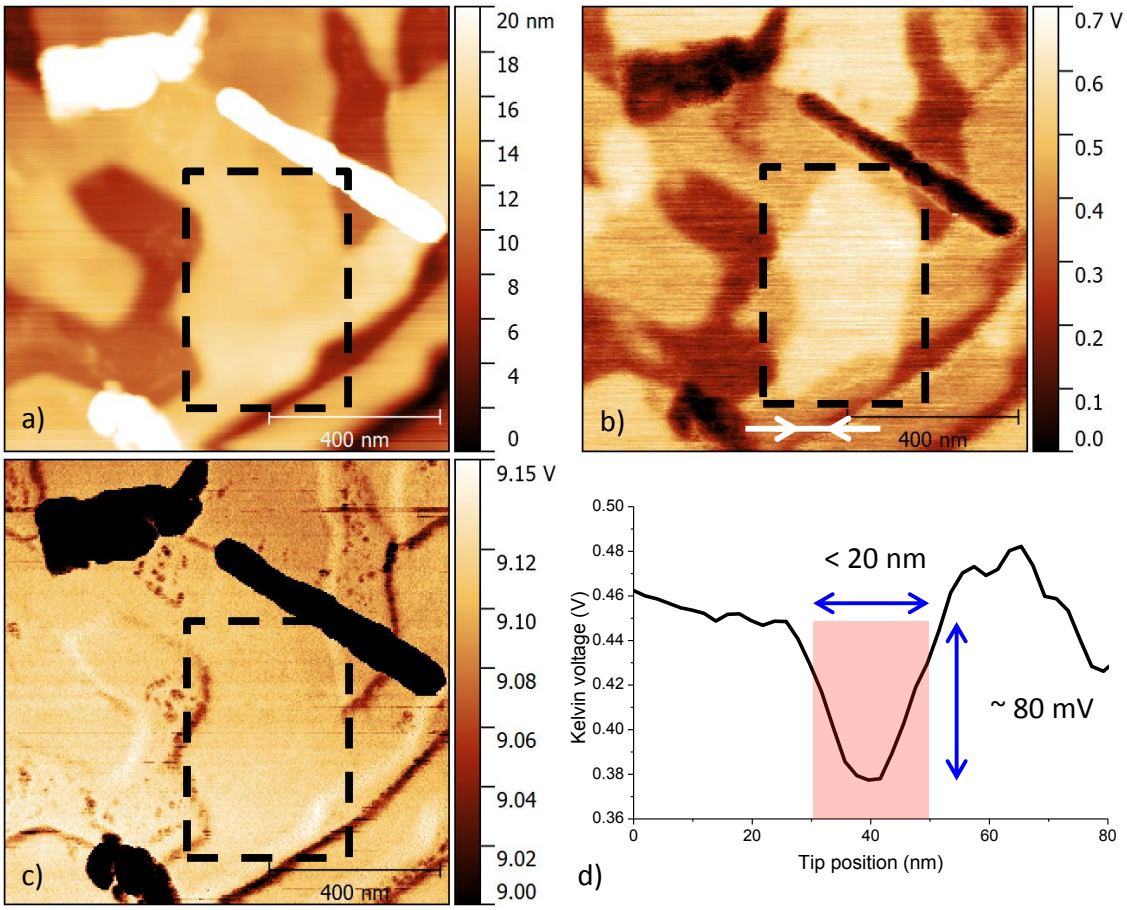

Figure 4.8: (a) Topography, (b) KPFM and (c) phase map of a graphene sample grown by CVD on a polycrystalline Cu substrate. The dashed line box shows the independence of KPFM to topography features and the accurate correction of only the phase shifts at ω_{ac}. The values of smallest featured extracted from (b) are indicated by the white arrow and plotted in (d).

The smallest, but clearly distinguishable potential variation in the KPFM map was chosen (white arrows in Figure 4.8b) to demonstrate the high resolution of the technique. The line profile (Figure 4.8d) shows a clear reduction of the Kelvin voltage of about 80 mV within a range of less than 20 nm. These results are comparable to the reported measurement of a 20 nm feature in InAlAs/InGaAs layered heterostructures resolved by Xie et al. [150] with a similar variation of potential. This proves the improvement by PM-KPFM over the state-of-the-art electric measurements with high spatial resolution in ambient conditions.

4.3 Comparison of AM- and PM-KPFM voltage drop analysis

To demonstrate the improvement of PM- over AM-KPFM voltage drop analysis, an operational graphene device is analyzed by both methods and a comparison of the KPFM maps and voltage drops obtained are presented next. All measurements were done in ambient atmosphere at room temperature, with the respective instrumentation for each method, a ω_{ac} of 1.5 kHz is used for PM while for AM $\omega_{ac} = \omega_1 \sim 425$ kHz was selected ($\omega_0 \sim 68$ kHz), both at $V_{ac} = 1\ V_{p-p}$. In Figure 4.9a, the topography map of the whole graphene device is shown, consisting of four contacts on top of the graphene channel. The AM-KPFM and PM-KPFM maps at $V_{ds} = 0$ V are shown in Figure 4.9b and Figure 4.9c, respectively, and are nominally centered at the same position of the topography map.

Qualitatively a better resolution and less variation of values of the PM- over the AM-KPFM map are seen from the images, specifically the noise reduction and definition of the features in the map for the same V_{ac}. Specifically, the graphene channel can be clearly differentiated from the substrate at the top and bottom of the PM-KPFM map. For the case of semiconductors, large modulation voltages can induce a band bending of the electronic band structure in the surface of the material [151]. Although graphene is considered to behave like a metal, the increase in resolution without increase of V_{ac} in PM is desired for KPFM in general to maintain a marginal contribution of the $\vec{F}_{dc}$ component to topography (see subsection 3.2.7).

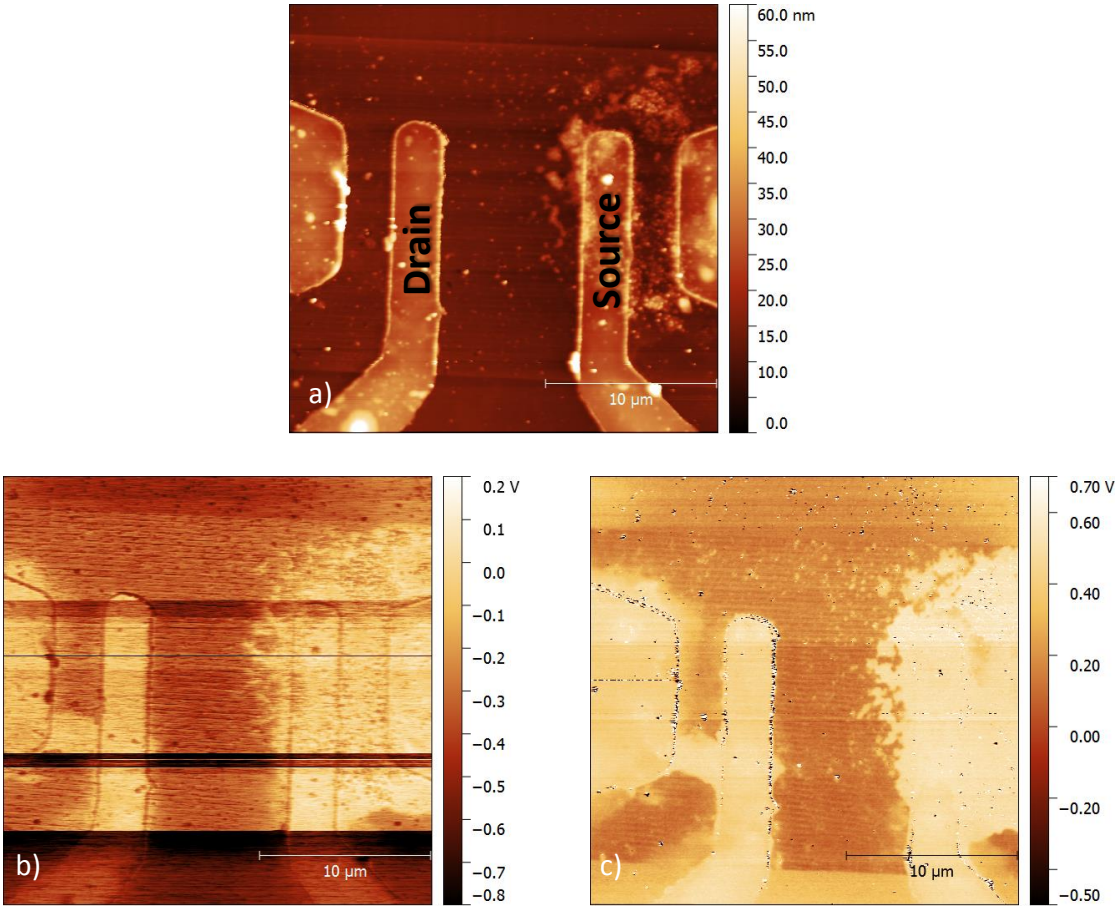

Figure 4.9: (a) Topography of the analyzed device, (b) AM- and (c) PM-KPFM maps both at $V_{ds} = 0$ V.

For the voltage drop analysis ± 1 V are applied to the device, Figure 4.10a and Figure 4.10b show the maps at V_{ds} = -1 V for AM- and PM-KPFM, respectively. It can be seen that similar qualitative results are obtained as in the 0 V case, and the definition of the channel′s device and loss of noise in the PM compared to AM image is evident once again. The channel is clearly distinguishable from the contacts and substrate. The area with different potential close to the source contact corresponds presumably to lingering metal rests of the fabrication process. The outer contacts have a floating potential and are not taken into account for the analysis. The full operation of both inner contacts can be seen as the whole area uniformly shifts the potential due to V_{ds}.

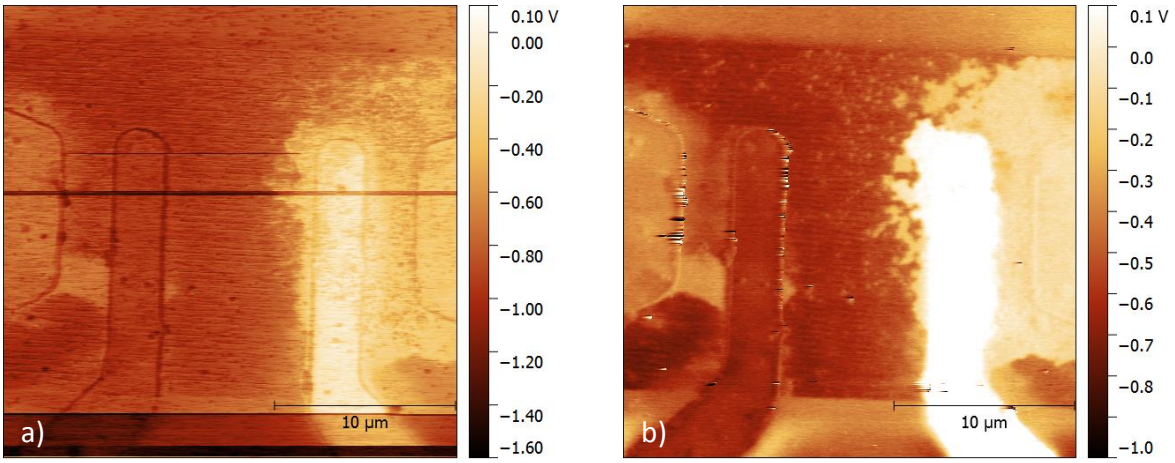

Figure 4.10: (a) AM- and (b) PM-KPFM maps of the graphene device at V_{ds} = -1 V.

The quantitative improvement of PM-KPFM in voltage drop analysis can be seen with a comparison of line profiles. An average of 11 lines are extracted out of the KPFM maps and subtracted following the process described in section 3.2.7. The results are plotted in Figure 4.11a and Figure 4.11c for AM- and PM-KPFM, respectively, where it can be seen the voltage drops for V_{ds} = -1 V (red lines) and V_{ds} = 1 V (black lines), in comparison with the topography (gray shaded area) of the device. Zooming into the drain interface (Figure 4.11b,d) the rate of change of the voltage over the tip position $\Delta V/\Delta x$ is used to compare both techniques. Thus, with slopes of 0.24 V/μm in AM versus that of 0.6 V/μm in PM, for the same interface, it is clearly seen that the detection of $\partial \vec{F}_{\omega_{ac}}/\partial z$ induces an increased reaction to surface potential variations without an increase of the modulation voltages.

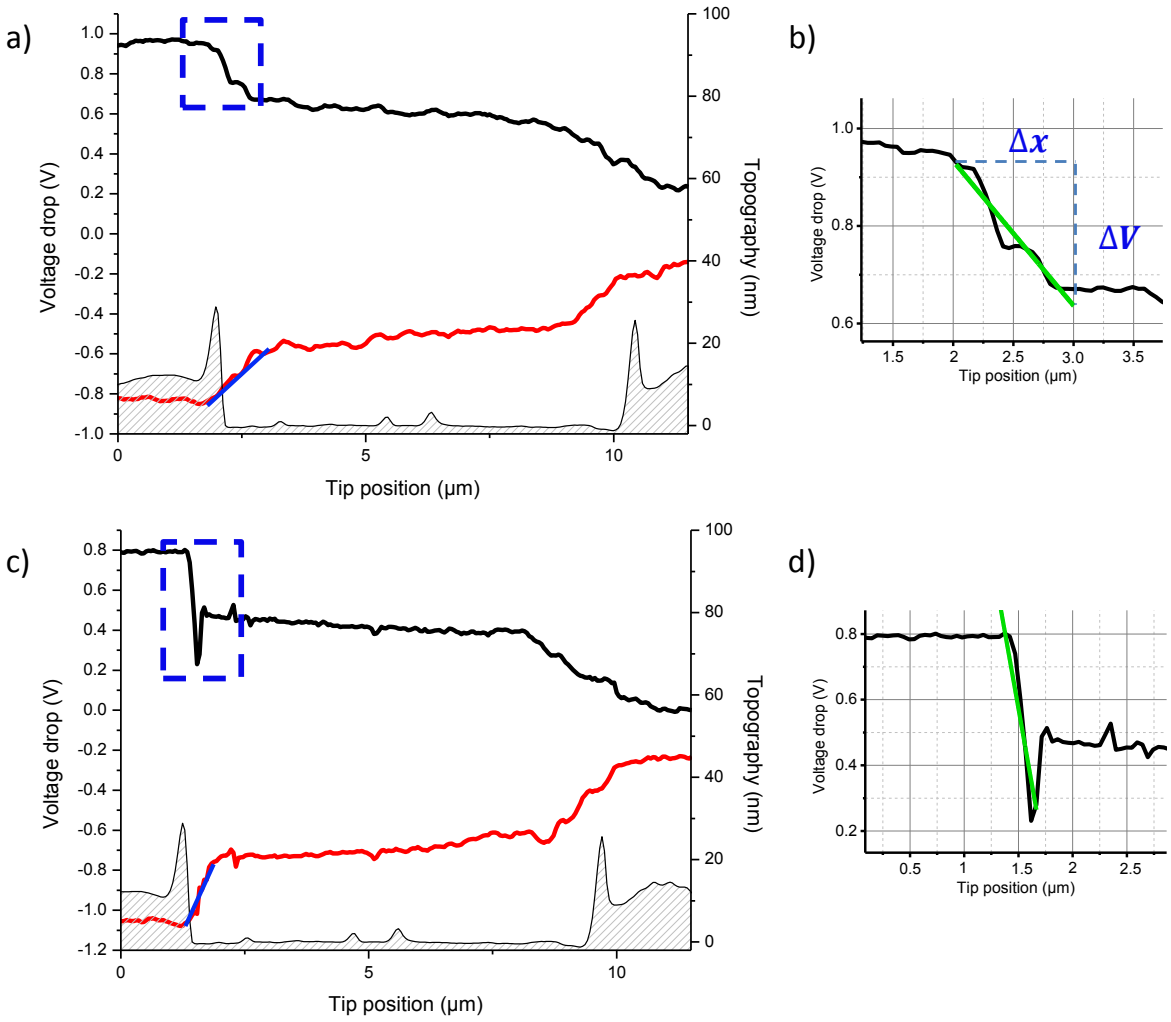

Figure 4.11: Line profile of the voltage drop of a graphene device (11 lines averaged), for (a) AM- and (c) PM-KPFM. Enlargement of the drain contact interface and the $\Delta V/\Delta x$ slope for (b) AM- and (d) PM-KPFM

4.4 Comparison of PM-KPFM voltage drop and 4 point probe method

To establish KPFM voltage drop as a reliable technique for the electrical characterization of microscale graphene devices, the same graphene devices were analyzed by both 4p method and KPFM voltage drop analysis to compare the results of R_c and R_s. The micrometer devices consisted of four evenly distanced nickel contacts (20 nm) over a graphene channel (l = 20 μm, w = 15 μm). The nickel contacts were reinforced with 100 nm of gold to prevent delamination during bonding and measurements. The 4p method was performed on a PM5 probe station (*Suss microtech*), using Tungsten 72T tips (*American Probes Inc*) with a 6 μm diameter, connected to a *Keithley* SMU 2612. For the KPFM voltage drop analysis, the two inner nickel contacts where microbonded to allow the application *in-situ* of voltage on the AFM sample holder.

An average of 11 profile lines was extracted from the KPFM maps. The KPFM voltage drop profiles at different V_{ds} were normalized for comparison by dividing each line by the nominal voltage applied. In Figure 4.12 the normalized voltage drop at different V_{ds} and the mean value of a representative device can be seen; this numerical average value was used for the calculations. In this device is seen an evenly distributed sharp voltage drop, at both drain and source interfaces as well as a homogeneous drop over the graphene channel. In the inset of Figure 4.12 the IV curves obtained during the KPFM and the macroscopic measurement during the analysis of the 4p method are shown. A variation of R_{2p} up to 17% can be identified between the data sets. This variation was unexpected as no modification was done on the device nor the ambient conditions changed. This suggests that the measurement conditions, i.e. from PM5 microprobes to microbonded pads, might partially influence.

The results for three different devices analyzed by the two methods are summarized in Table 4.1. For the 4p method the resistances are shown for channel (R_s), both contacts (R_c) and the total (Sum). The resistance calculated by KPFM voltage drop are separated by channel (R_s), both contacts (R_c), the drain-to-source voltage drop ratio (d/s) and the individual resistances for each contact ($R_{c,d}$, $R_{c,s}$). The methods are then compared as a percentage of the difference between the results for channel and contacts.

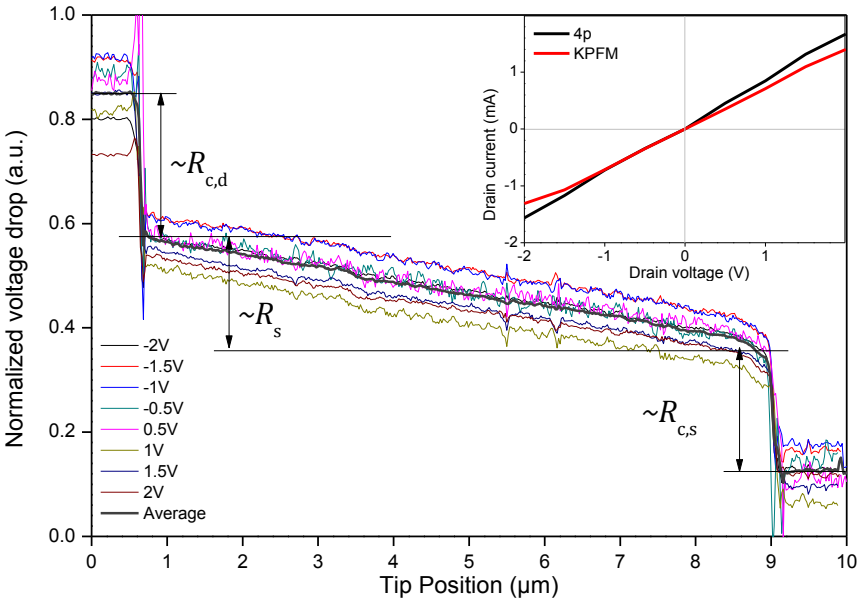

Figure 4.12: (a) Normalized voltage drop of device 66 (see Table 4.1) and (inset) output characteristics during the macroscopic 4p and KPFM measurements

	4p Method (Ω)			**KPFM** (Ω)					**% Difference**	
Device	R_s	R_c	Sum	R_s	R_c	d/s	$R_{c,d}$	$R_{c,s}$	R_s	R_c
15	431	1426	1858	244	2095	0.66	834	1261	43	-72
46	317	1723	2040	309	878	0.95	429	449	3	21
66	258	1001	1259	291	741	1.14	395	345	-12	-14

Table 4.1: Sumarized values of graphene device resistances obtained by 4p method and KPFM voltage drop analysis.

Device 66, discussed above, shows an overall difference of 13% for R_c and R_s between 4p and KPFM methods. Furthermore, device 46, shows only a 3% difference on the R_s values. However, the analysis of device 15 shows differences up to 72% at the contacts, which might question the reliability of KPFM as a characterization method.

To discuss the discrepancy of device 15, Figure 4.13 shows its normalized voltage drop. In this device, the variations between measurements at different V_{ds} has a stronger effect compared to device 66. At the interfaces, the voltage drop at the source ($R_{c,s}$) is almost two times the drop at the drain contact ($R_{c,d}$), which potential drop fluctuates largely compared to the mean value, suggesting a damaged contact. The variations found between 4p and KPFM methods can arise due to the time between both measurements, having an effect on the integrity of the device, such as oxidation of the nickel contacts, as well as adsorption or desorption of species in the exposed graphene channel. From the IV

curve (inset), it can be seen that the total resistance obtained during the KPFM analysis indeed increased up to 50% compared to the R_{2p} obtained during 4p analysis. By using the information of the IV curves for the 4p in the calculations of KPFM their discrepancy can be reduced down to 23%. It can be argued that changes over time on the device itself are responsible for the discrepancy between the macroscopic and microscopic approach. Thus, it can be concluded that given well behaved and stable operating devices, KPFM voltage drop can render results which are comparable to macroscopic methods.

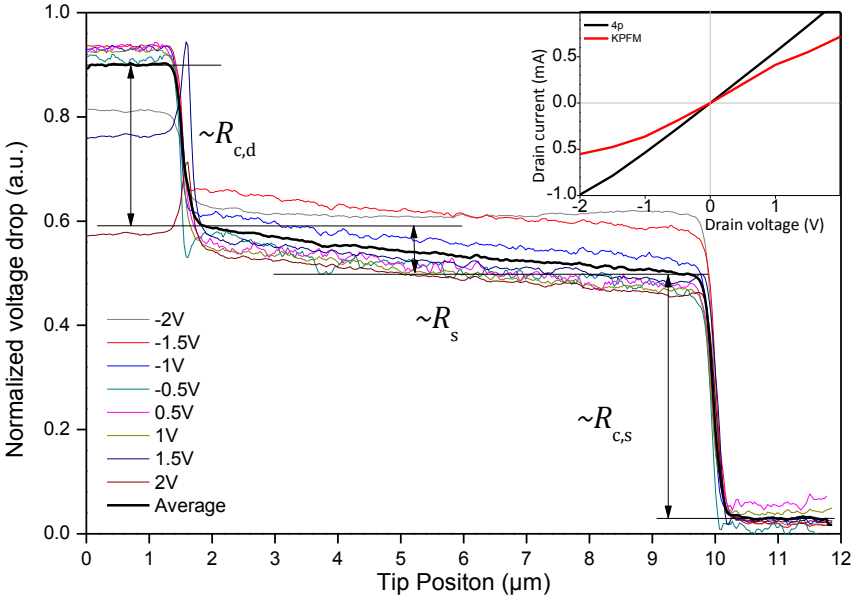

Figure 4.13: (a) Normalized voltage drop of device 15 and (inset) output characteristics of the macroscopic 4p and KPFM measurements

4.5 Conclusions

The improvement of the established KPFM technique by the detection of the electrostatic force gradient in ambient conditions by means of the phase shifts of the mechanical oscillations was successfully attained. It was shown that the equipment used works in the low frequency shifts regime, where the phase shifts are proportional to the frequency shifts for the detection and nullifying of the sideband′s amplitude at $\omega_0^{'} \pm \omega_{ac}$ and $\omega_0^{'} \pm 2\omega_{ac}$. Thus, using the correct signals, set of parameters and equipment allows the use of the higher resolution that the second order capacitance offers for KPFM. The achievable resolution of PM-KPFM for features smaller than 20 nm and with 80 mV in surface potential variation showed an improvement comparable with state-of-the-art measurements for KPFM in ambient conditions. In the voltage drop analysis, it was found a rate of change for AM-KPFM of $\Delta V/\Delta x = 0.24$ V/μm, while for the PM-KPFM data a $\Delta V/\Delta x = 0.6$ V/μm which supports the improvement in resolution.

The comparison of the results with the macroscopic 4p method gives a level of certainty for the electrical characterization of graphene devices using KPFM. The use of this approach allows overcoming two disadvantages from the macroscopic conventional techniques saw in section 3.1. First, 4p probe and/or TLM cannot be used to characterize functional devices which have any other but the corresponding layout for the technique. Second, they cannot be used if geometrical restrictions exist, i.e. if the conductive material to be investigated is so small that no more than two contacts are possible. Even more, KPFM allows the separation of potential drops not only between the conductive channel and the contacts but also discriminates the drops and thus the resistance between both contacts

Chapter 5

Effect of the reduction level in FGS devices

The structure of FGS has a variable density of oxygen-containing functional groups and lattice defects [10]. Higher levels of reduction, in terms of the carbon to oxygen ratio (C/O), have been reported to reduce the overall resistance. This is explained by Mattevi et al. for chemically (and subsequent thermally) reduced GO as a change in the charge transport mechanism [14]. Using Raman spectroscopy the domain size of sp^2 areas was followed at different reduction stages, finding that the oxygen content decreased (higher C/O) without any distinguishable increase in the sp^2 domain size. Therefore, they concluded that at a sp^2 fraction of 60%, the charge transport mechanism undergoes a transition from hopping and tunneling between the scattered sp^2 domains to a diffusive transport due to the increased presence of small graphitic clusters, as illustrated in Figure 5.1.

One of the main applications of FGS is as conductive inks [61, 62]. Conductive inks can be seen as an interconnected network of single FGSs with nominally the same electrical properties. Hence, a study of the effects that the charge transport mechanism have in single FGSs flakes and on the metal/FGS interfaces is a valuable addition to the understanding of the material itself and its collective behavior in a conductive network. However, as it will be seen in this chapter, the characteristic geometry of FGSs, independent of its degree of reduction, does not allow more than a pair of contacts with standard laboratory equipment. Therefore, for the determination of the FGS sheet and contacts contribution to the overall resistance, KPFM voltage drop analysis stands as a remarkable option for this task.

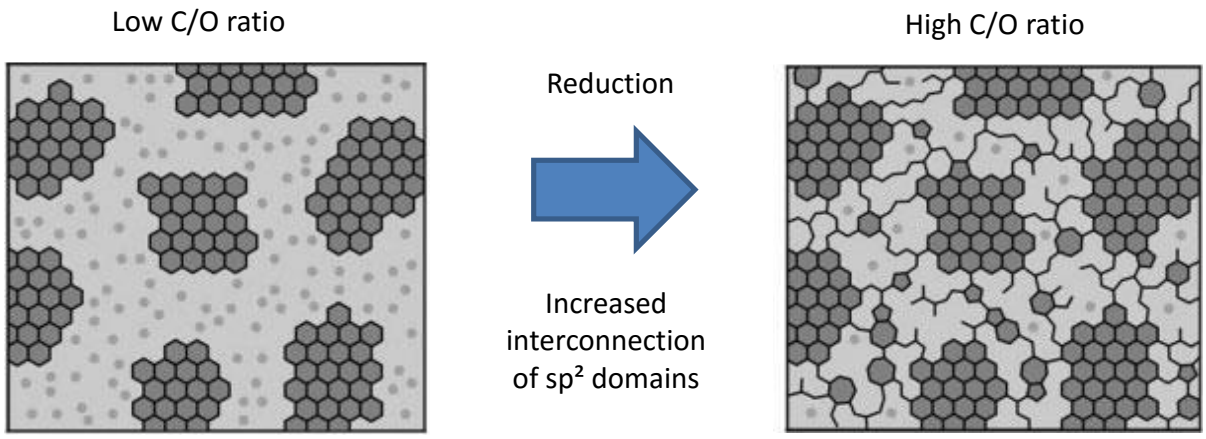

Figure 5.1: Structural model of the charge transport transition in chemically reduced graphene oxide comparing separated (left) and interconnected (right) sp^2 clusters (dark grey areas). Oxygen species (grey dots) bonded to carbon atoms disrupt the sp^2 network. Adapted from [14].

Hence, this chapter deals with the systematic characterization of ρ_c and ρ_s of FGSs thermally exfoliated and reduced at various temperatures from 500 ^{o}C to 1500 ^{o}C by means of KPFM voltage drop analysis. The samples were selected to range from low to high levels of reduction. First, the geometric characterization of single flakes in function of their C/O ratio by AFM analysis is presented. The chapter continues with the KPFM maps of the contacted flakes at $V_{ds} = 0$ V, followed by the KPFM maps at different values of V_{ds} and the output characteristics. Finally, the KPFM voltage drop profiles are presented along with the individual calculations of ρ_s and ρ_c for the different C/O ratios. The results in this chapter are partially presented in the author′s publication [13].

5.1 Experimental details

The production, chemical characterization and contacting of the FGS samples was done by colleagues at Princeton University. The C/O ratio of the samples was determined using combustion analysis (*Atlantic Microlabs*) and energy dispersive X-ray spectroscopy (*EDS, INCA x-act, Oxford instruments*, attached to *Vega 1* scanning electron microscope, *Tescan USA*) of compressed FGS pellets. The FGS samples are identified as FGS_x, were x corresponds to its nominal C/O ratio, i.e. its degree of reduction. 10 mm x 10 mm pieces of a silicon wafer with a 300 nm top layer of thermally grown SiO_2 were used as the substrates for the electrical characterizations. FGSs were suspended in ethanol solution at a concentration of 0.1 g/l by tip sonification (*Vibracells Inc.)* for 30 min, followed by centrifugation at 3000 rpm for 1 h (*IEC Centra GP8R* centrifuge with 218A rotor). Onto the substrates 10 ml of suspension were drop-casted and allowed to dry at room temperature overnight. The position of the selected individual FGSs with respect to predefined alignment marks was measured with optical microscopy (*Axioplan 2 with AxioCam HRc, Carl Zeiss MicroImaging, Inc.*) and two electrical contacts were applied to each selected sheet using e-beam lithography (*eLine, RAITH Inc*) and metal evaporation (*Angstrom Engineering*, 10 nm Ti adhesion layer and 100 nm Au) followed by a lift-off. A detailed procedure for the fabrication of the contacted FGS samples is presented in section A.1.

The AFM and KPFM measurements were done on a *Veeco Innova* SPM system using silicon probes coated with 25/5 nm of Cr/PtIr (*Budget sensors* Multi 75E). The sub-micrometer devices were bonded using a *Delvotek* micro bonder and a *Keithley* Model 2601 to apply the V_{ds} voltages. The devices were under voltage bias during the whole duration ($\sim$ 20 min) of the specified measurement. All electrical measurements were performed in air at room temperature. The temperatures for thermal exfoliation of the three different C/O ratios $FGS_{7.3}$, FGS_{24} and FGS_{170} analyzed by KPFM,were, respectively, 500^{o}C, 1100^{o}C and 1100^{o}C with additional heating in Ar atmosphere for one hour.

5.2 Geometric dimensions of FGS

The variability of the individual flakes morphology have a direct impact on the contacting procedure i.e. every flake has its own contact layout, and therefore the end-product has specific dimensions. In Figure 5.2a, an AFM image of a contacted FGS is presented, where its perimeter is delimited to improve visibility. The sections of the FGS underneath the metal, making direct contact, can be visualized as the deposition of the metal follows the contour.

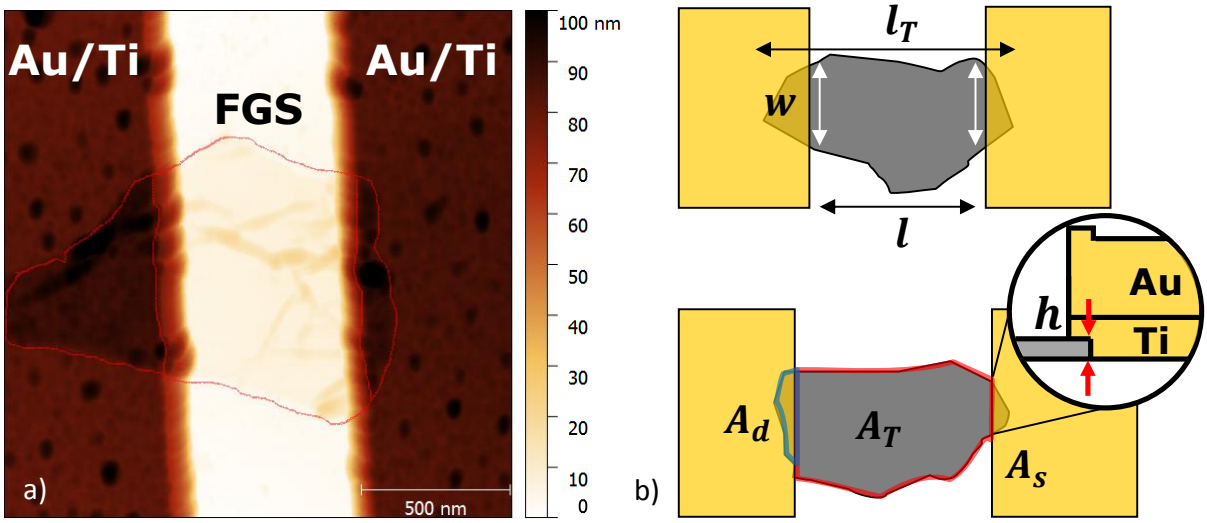

Figure 5.2: (a) AFM image of a FGS flake with inverted scale bar contrast to highlight its perimeter. (b) Schematics of the irregular shapes found in the flakes and the measurements reported.

In Figure 5.2b, the flakes′ dimensions reported in this chapter are indicated and the irregular FGS shapes schematized, which yield inhomogeneous length and contact widths within a single flake. The total length of the flake (l_T) was taken from the visible edges of the FGS flakes underneath the contacts. The length on the substrate (l), which represents the conductive channel, was taken as the distance between the contacts. The contact width (w) between the two metals and the flake was usually dissimilar up to a factor two; the values are reported as an average from both sides for simplification. The mean height (h) or thickness, was taken as an average of substrate-to-FGS steps, not considering wrinkles or any other features. The flake area on the substrate (A_T) not covered by the contacts as well as the area of the flake underneath the metal (A_d,A_s), having no ordinary geometry, were calculated by an image processor software (*SPIP, Image metrology*).

An example of a $FGS_{7.3}$ flake is seen in Figure 5.3. Its dimensions are $l_T = 1.25$ μm, $l = 0.8$ μm, $w = 0.9$ μm, $A_T = 0.64$ μm^2, $h = 1.26$ nm, $A_d = 0.109$ μm^2 and $A_s = 0.112$ μm^2. The shapes of the wrinkles of this low temperature reduced sample suggest the presence of functional groups and defects that induce strain in the carbon lattice [55]. Also, it is likely that during the sheet deposition, the sheet folds into itself and/or capillary forces from the drying of the ethanol suspension acting on the sheet are involved in the formation of this topographical features [152].

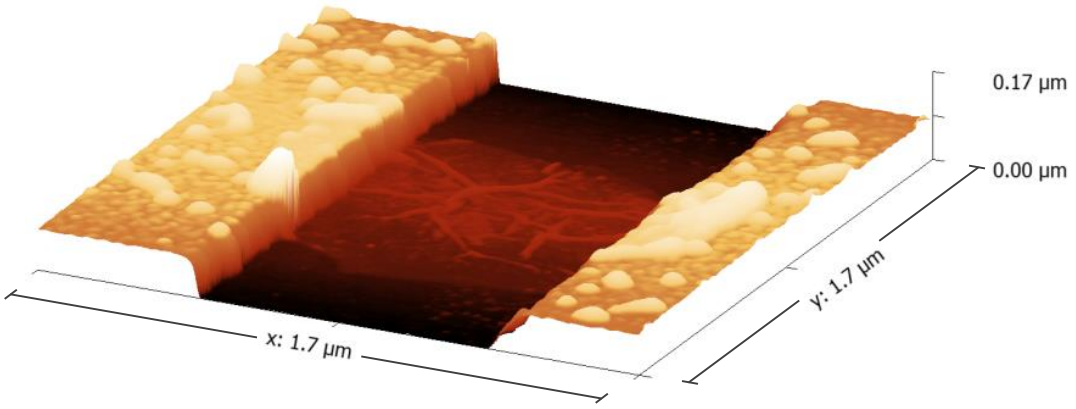

Figure 5.3: 3D representation of AFM topography of a $FGS_{7.3}$ flake. A well-defined wrinkle structures can be seen, over an otherwise flat surface. The width of the wrinkles is less than 50 nm.

A representative FGS_{24} flake can be seen in Figure 5.4. It has a $l_T = 1.2$ μm, $l = 0.33$ μm, $w = 0.62$ μm, $A_T = 0.198$ μm^2, $h = 5.21$ nm, $A_d = 0.26$ μm^2 and $A_s = 0.09$ μm^2. Here the conductive channel is only 27% of the whole flake length. With similar dimensions as its lower C/O counterpart, this flake is a good example of the challenging task of the contact procedure to individually analyze this material.

The analysis of one FGS_{170} flake resulted in a $l_T = 1.2$ μm, $l = 0.4$ μm, $w = 0.74$ μm, $A_T = 0.25$ μm^2, $h = 23$ nm, $A_d = 0.11$ μm^2 and $A_s = 0.2$ μm^2. The visible increase in the number, height and shape of the wrinkles, which differs greatly from those at lower C/O ratios, suggest that due to the sudden high temperatures of the thermal shock, a violent expansion of the sheets could be involved in the formation of these features.

Summarized in Table 5.1 are the AFM measurement results of 11 FGS flakes. In general, all FGS flakes have areas of about 1 μm^2 with a variety of complex wrinkled structures, independent of the level of reduction. It is also observed that h tends to increase with the C/O ratio. This trend is also followed by the density and height of wrinkles. To prevent damage by electrostatic discharge before operation of the FGS

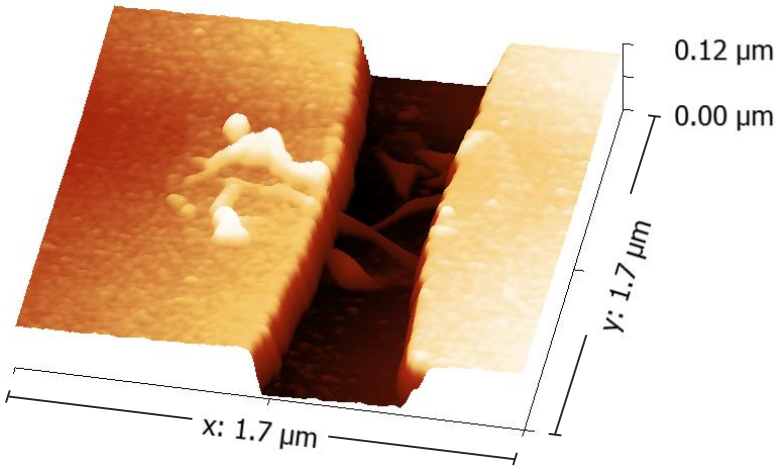

Figure 5.4: 3D representation of AFM topography of a FGS_{24} flake. At this level of reduction the flakes show an averaged increase in the thickness and the width of the wrinkles can reach more than 50 nm.

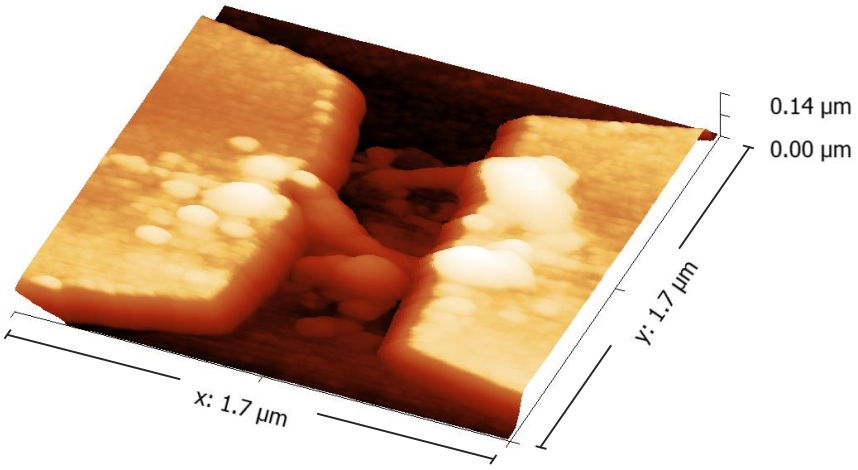

Figure 5.5: 3D representation of AFM topography of a FGS_{170} flake. The more capricious shape of the wrinkles in this material might be related to the sudden thermal exposure during synthesis.

device a short circuit is patterned between the metal electrodes (see section A.1). During the length of the analysis, all devices remain operational without physical deformations or damage. Partial damage could be expected due to Joule heating of the electric current flowing through the reduced contact area A_d and A_s between the flake and the metal [153]. The length of the irregular contact area at drain and source was equal or less than 200 nm. Avorious et al.[154] define a transfer length over which the carriers start to effectively flow in and out between metal and graphene, which has been measured to be <0.2 μm [154, 155]). This suggests that the whole area of contact, A_d and A_s, is

actively participating in the injection of carriers into FGS. Moreover, the small areas of thermally exfoliated and reduced FGSs have an advantage over larger types of reduced GO to prevent problems such as nozzle clogging in printable electronics [156, 157].

		$\mathbf{C/O}_{7.3}$	$\mathbf{C/O}_{24}$	$\mathbf{C/O}_{170}$
Total length (l_T)	μm	1.16±.06	0.94±.18	1.04±.12
Length on substrate (l)	μm	0.57±.14	0.25±.11	0.38±.1
Width (w)	μm	0.99±.12	0.69±.04	0.70±.17
Mean height (h)	nm	1.61±.92	4.19±2.1	11.71±6.9
Area on substrate (A_T)	μm^2	0.49±.09	0.14±.07	0.23±.06
Drain contact area (A_d)	μm^2	0.20±.07	0.15±.09	0.13±.04
Source contact area (A_s)	μm^2	0.08±.02	0.10±.04	0.09±.08

Table 5.1: Geometrical measurements summarized for a total of 11 measured FGS flakes. For the KPFM voltage drop analysis the individual geometric data for each flake is used.

5.3 KPFM measurements and output characteristics

In Figure 5.6a and Figure 5.6b the KPFM maps of a $FGS_{7.3}$ and a FGS_{24} sample at $V_{ds} = 0$ V are shown, respectively. For $FGS_{7.3}$ a well-defined channel with similar work function values to the metal contacts is observed, while the substrate presents a noticeable difference. Compared to the values of the Au sample obtained in subsection 4.2.1, the Au/Ti contacts values are larger than expected. This shift is explained by the intrinsic variability between the macroscopic Au sample and the sputtered Au/Ti contacts, along with different ambient conditions and/or aging effects of the metals contacts and that of the tip coating. However, since the relative difference between Au and the SiO_2 values (200 mV) and a negligible difference between FGS and metal are in agreement with prior results [147], this can be seen as a V_k offset.

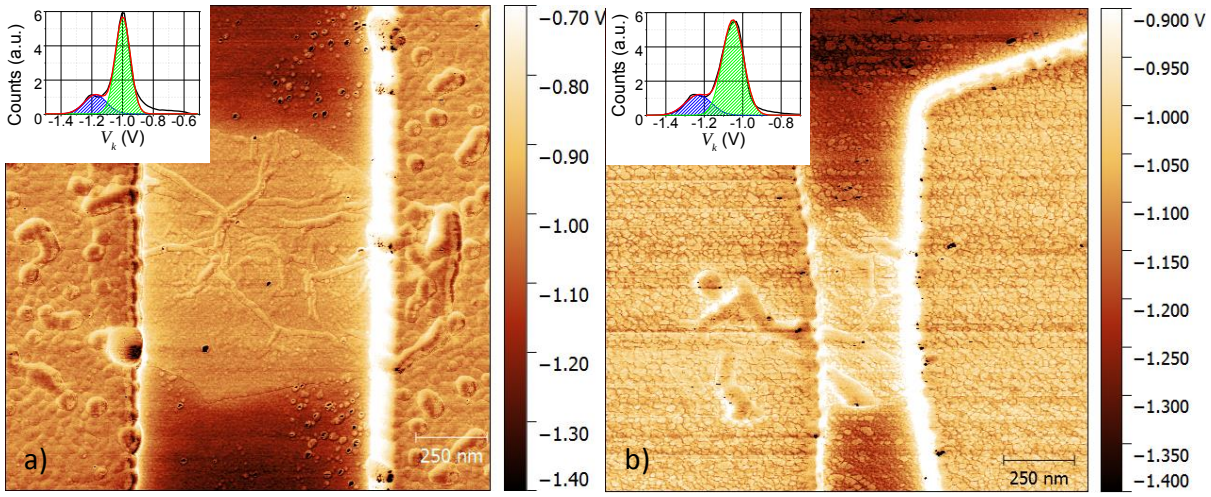

Figure 5.6: KPFM images at $V_{ds} = 0$ V of (a) $FGS_{7.3}$ and (b) FGS_{24}. Visible are the similar values for FGS and contacts (green shade insets) while the SiO_2 substrate has a noticeable difference (blue shade insets).

From literature a reduction of ϕ_{FGS} due to decreasing oxygen content is expected, as seen from GO to graphene [158]. However, a direct conclusion on the work function from these KPFM values is withheld. The ambient conditions along with the own variability of the C/O ratios seen in EDS analysis [13] yield inconclusive and speculative data. Also, not only the C/O ratio and recovery of the sp^2 network plays a role in ϕ_{FGS}, additionally the type of dopant is involved. Electron withdrawing groups, such as OH, will increase ϕ_{FGS}, while electron donating groups such as CH_3 will reduce it [159]. Nevertheless, these variations will be subtracted and will not affect the calculations of

the contact and sheet resistance during KPFM voltage drop analysis.

The KPFM maps at different V_{ds} and the output characteristics for $FGS_{7.3}$, FGS_{24} and FGS_{170} are presented next. The KPFM map of $FGS_{7.3}$ at $V_{ds} = 2$ V is seen in Figure 5.7a. A homogeneous contrast over the whole area of both contacts can be appreciated. The FGS channel shows a (sudden) change of V_k values at the contact interfaces while over its length there is a gradual reduction. The KPFM resolves gradual variations in the SiO_2 substrate as V_{ds} is applied, measuring the relative shifts of the substrate′s Fermi level. However, it is expected that these shifts does not overcome the large band gap of the substrate and therefore does not contribute to the device′s conductivity. In Figure 5.7b, I_{ds} is recorded over the range of $V_{ds} = \pm 2$ V. It can be seen that $FGS_{7.3}$ exhibits a non-linear behavior with dV_{ds}/dI_{ds} values (blue lines) ranging from 580 to 3000 kΩ. Based on the geometrical measurements of A_d and A_s, in Figure 5.7c a factor two increment in the current density ($I_{ds}/A_{d,s}$) as current flows in and out of the FGS can be seen. This observation suggests that small FGS-to-FGS contact areas are still capable of creating a fully conductive network of this material.

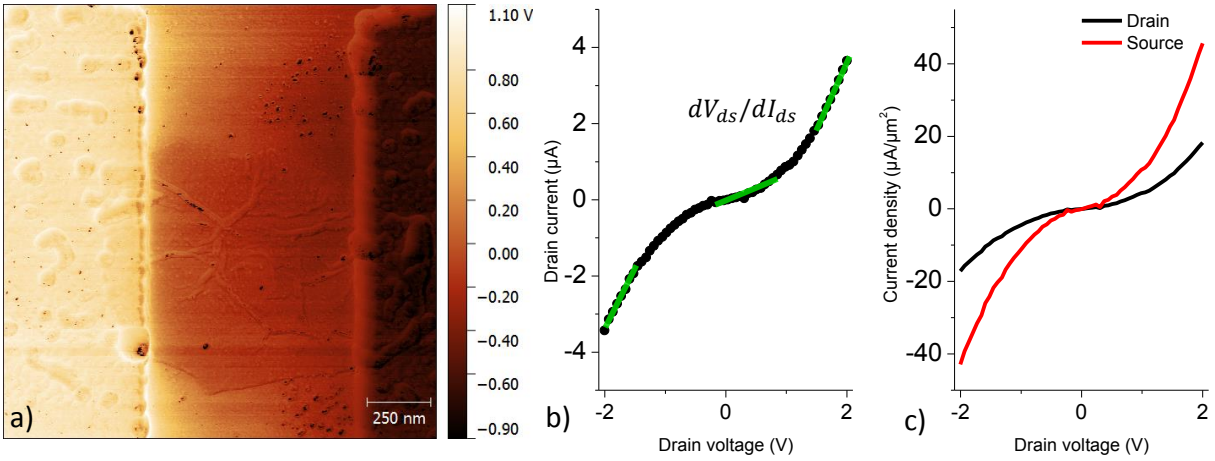

Figure 5.7: (a) KPFM map at $V_{ds} = 2$ V of a $FGS_{7.3}$ device, where fully operational contacts and channel can be observed. The (b) IV characteristics show a non-linear behavior (black dots) with different dV_{ds}/dI_{ds} (blue line) values over the whole range. The (c) I_{ds} normalized by A_d and A_s, demonstrates the increase of a factor two of the current density at such small contact areas.

In Figure 5.8a the KPFM map of a FGS_{24} device at $V_{ds} = 2$ V is shown. At this level of reduction, a more gradual change in the contrast from drain contact to FGS and from FGS to source contact can be observed. In Figure 5.8b the IV curve of this sample is compared to that of $FGS_{7.3}$ where a transition into a linear behavior with an I_{ds} increase is already visible. Different studies report the non-ohmic behavior seen in $FGS_{7.3}$, as well as a tendency to recover the linear behavior by increasing the reduction of the GO [160, 161, 162, 163, 164, 165, 166]. However, compared to FGS_{24} samples, a linearization was only partially achieved by their reduction process. In a related work from Jung et al. [167], using week-long weak shear forces for delamination, they obtained larger flakes of lower C/O ratios. In these larger samples, even with the use of a 4-probe configuration to remove the influence of ρ_c from the IV curve, nonlinear behavior was still observed in all cases. This suggests that the low C/O ratio of the sheet, and not the contacts, dominates the IV behavior.

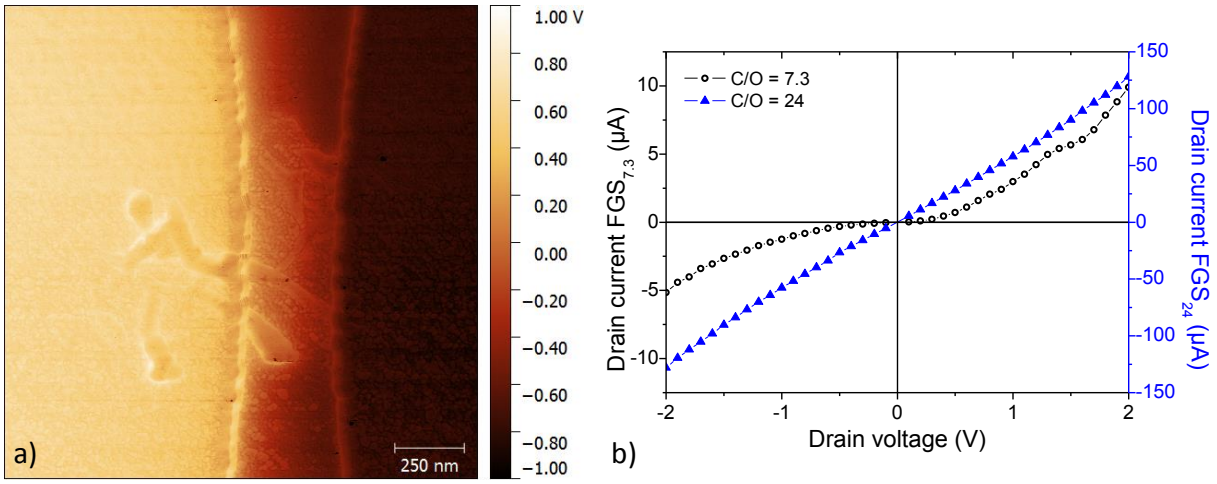

Figure 5.8: (a) KPFM map of a fully functional FGS_{24} device at $V_{ds} = 2$ V. (b) Comparison of the non-linear and linear IV behavior of $FGS_{7.3}$ (circles) and FGS_{24} (triangles), respectively.

The KPFM map of a representative FGS_{170} sample at $V_{ds} = 1$ V is seen in Figure 5.9a. Here a drain contact with homogeneous surface potential can be seen while the channel and source contact present variations over their area. Such difference in the channel is visible in the KPFM measurement at 0 V (not shown), therefore it can be expected that its origin is related to a heterogeneous C/O composition of the flake. A conclusion over the spatial composition of this flake is out of the scope of this investigation.

These variations, however, do not affect the overall operation of the device, as a linear relation to V_{ds} is obtained with a reduced overall resistance. At Figure 5.9b the I_{ds} curves of the three C/O ratios are compared. Here can be clearly noticed the trend of decreasing R_{2p} with increasing C/O ratio.

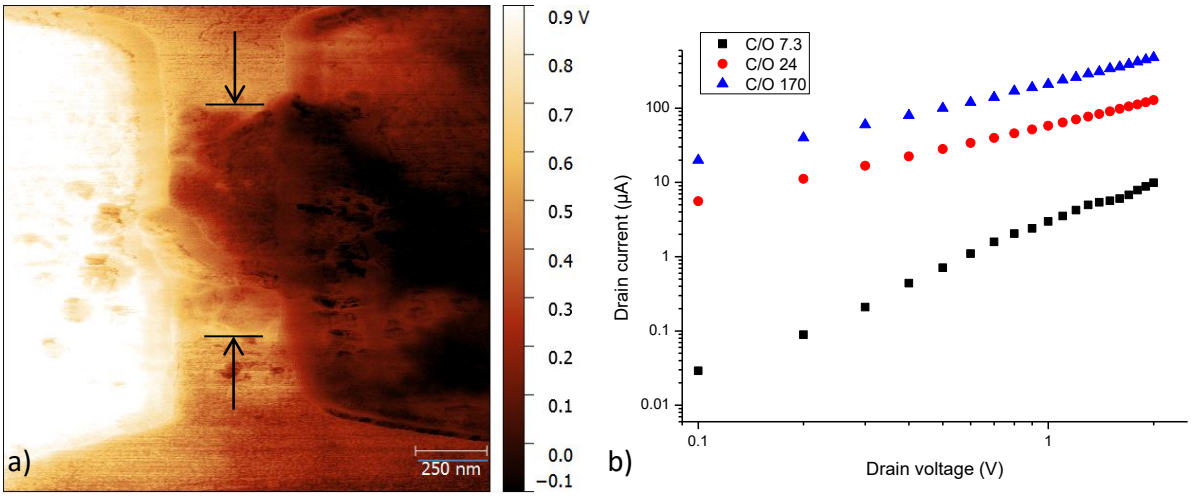

Figure 5.9: (a) KPFM map of a FGS_{170} device at $V_{ds} = 1$ V. The flake is indicated by the arrows. (b) Comparison of the I_{ds} increment vs drain voltage for $FGS_{7.3}$, FGS_{24} and FGS_{170} samples.

5.4 KPFM voltage drop analysis

KPFM voltage drop analysis are employed to obtain the contribution of the contacts to the total resistance of the devices presented above and with it to investigate the impact of the non-ohmic behavior on the metal/FGS interfaces.

In the upper part of Figure 5.10a is shown the (horizontal) line profile extracted from the topograpy map of $FGS_{7.3}$. Aligned to the topography profile are the voltage drops at different V_{ds} (bottom of Figure 5.10a), calculated from extracted profile lines of the different KPFM maps. It is visible how the sample has a severe voltage drop from the drain (left) electrode to the channel. In Figure 5.10b the device current is plotted as a function of the potential drops across the drain contact, graphene sheet and source (right) contact. The potential drops are obtained as described in section 3.2.7.

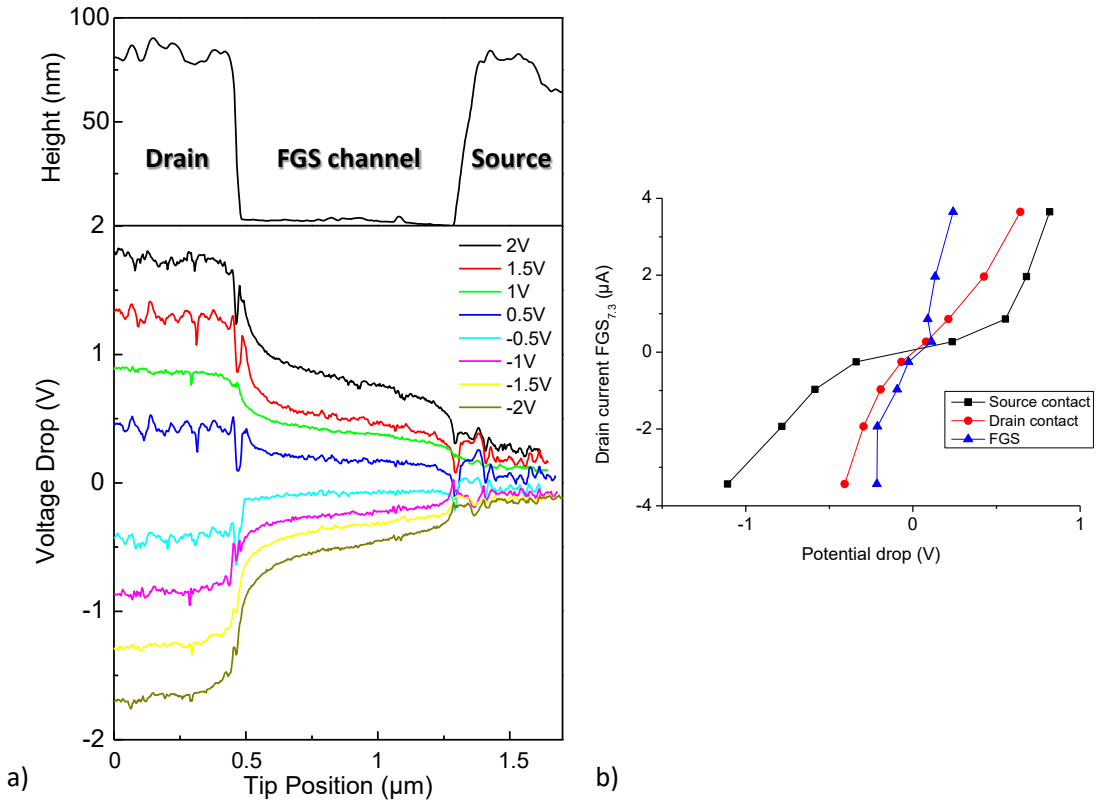

Figure 5.10: (a) KPFM voltage drop of a $FGS_{7.3}$ device and (b) KPFM-determined IV curve of the drain contact, graphene channel and source contact.

Using the potential drops at the different sections of the device, along with the corresponding I_{ds}, a set of three different IV curves are obtained from each individual measurement. These KPFM-determined IV curves reflect the behavior of the contacts and the FGSs independently and can be used along with the geometric dimensions to calculate the respective contact and sheet contribution to the overall resistance. The pronounced non-ohmic relationship between I_{ds} and V_{ds} resulted in a corresponding maximum effective ρ_s of 430 k$\Omega/\square$ and maximum ρ_c at drain and source of 1000 and 148 k$\Omega\mu$m, respectively. A C/O ratio of 7.3 corresponds to an oxygen content of 12%, and thus the sp^2 domains that have formed as a result of the thermal reduction treatment are likely not percolated [14]. Therefore, it is contended that the observed non-linear behavior is likely due to hopping within the FGSs sp^2 regions, and the large contact resistances are related to semiconducting characteristics of the FGS resulting in a Schottky contact between the FGS and the metal contacts [161, 166].

From the IV curves obtained by KPFM, at the drain and source contacts there is no pronounced asymmetry between the positive and negative polarity of V_{ds}. For Schottky contacts, however, it is expected that while one contact is under reverse bias (high resistance) the other one should be under forward bias (low resistance) and vice versa, as the polarity of V_{ds} changes [161]. Since no clear indication for such behavior is found in the data this could be related to convolution effects caused by the dimensions of the AFM tip, as demonstrated in a recent KPFM study of Si nanowire Schottky junctions [168]. Therefore, it is concluded, within the accuracy of these measurements, that the Schottky characteristics are superimposed by the onset of ohmic behavior and/or a tunneling contribution.

In Figure 5.11a, the KPFM voltage drop of a FGS_{24} device is presented. At this reduction grade, a reduction of the voltage drop at the interfaces and an increase of the drop at the channel can be seen, while the overall resistance is reduced by a factor of 10. For the FGS_{24} the KPFM-determined IV curves are nearly linear for the sheet and contacts measurements, corresponding to an intrinsic ρ_s of 21 k$\Omega/\square$. Due to noise and the reduced potential drops at the metal/FGS interfaces an upper estimation was made for ρ_c at the drain and source contacts of 1.6 and 1.9 k$\Omega\mu$m, respectively (Figure 5.11b).

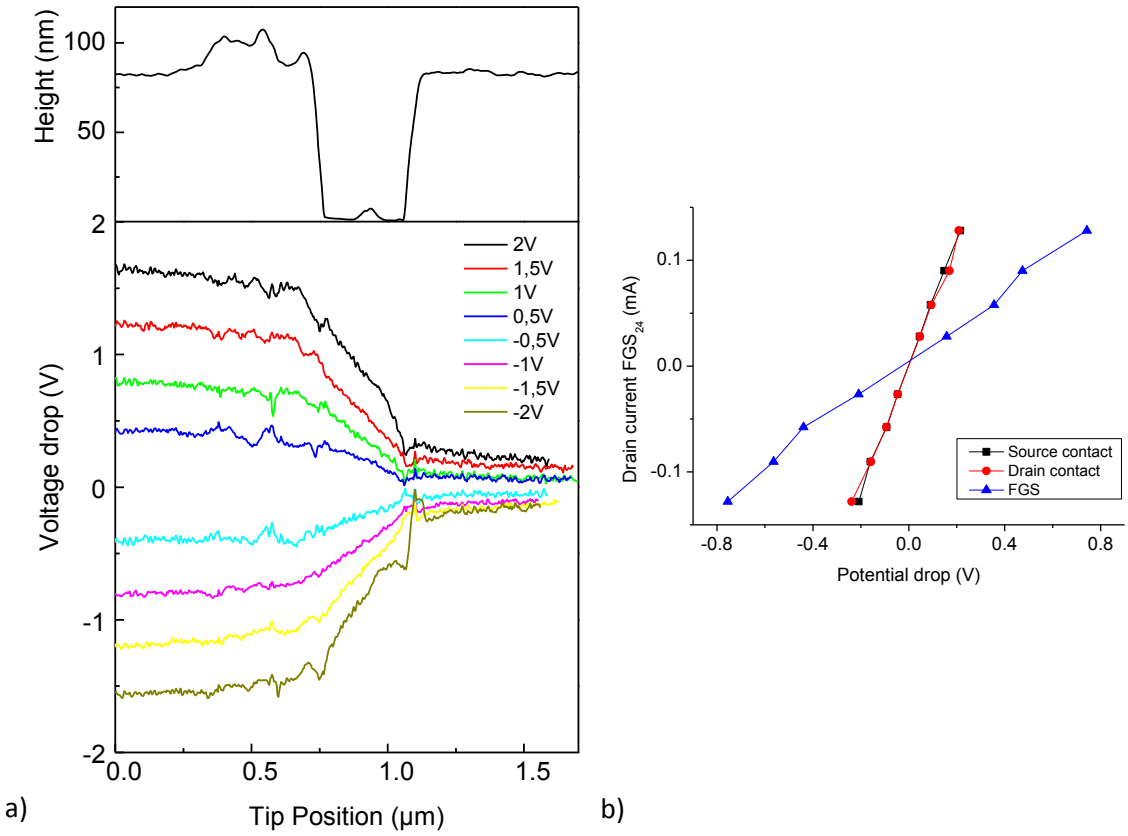

Figure 5.11: (a) KPFM voltage drop of FGS_{24} and (b) KPFM-determined IV curve of the drain contact, graphene channel and source contact.

The highest C/O ratio sample analyzed show as well a low voltage drop at the contact interfaces while the channel dominates the resistance of the device (Figure 5.12a and Figure 5.12b). Also, a nearly linear (KPFM-determined) IV curve is observed, corresponding to an ρ_s of 10 k$\Omega/\square$ and ρ_c of less than 1 k$\Omega\mu$m. These observations are attributed to the existence of a highly percolated network of sp^2 hybridized carbon network within the FGS at this degree of reduction [14]. For all sheets characterized by KPFM, the overall device resistance corresponds, within measurement error, to the macroscopic results from a larger set of similar devices [13].

GO-derived graphene materials with an electrical conductivity comparable to that of the most strongly reduced FGSs on this investigation could only be synthesized by a combination of chemical and subsequent thermal reduction at 900°C in Ar/H_2 [169]. Thermal reduction alone, without prior chemical treatment, cannot decrease the oxygen content of substrate-supported graphene oxide sufficiently [170] and thus yields resistances several orders of magnitude larger than those observed in the devices here

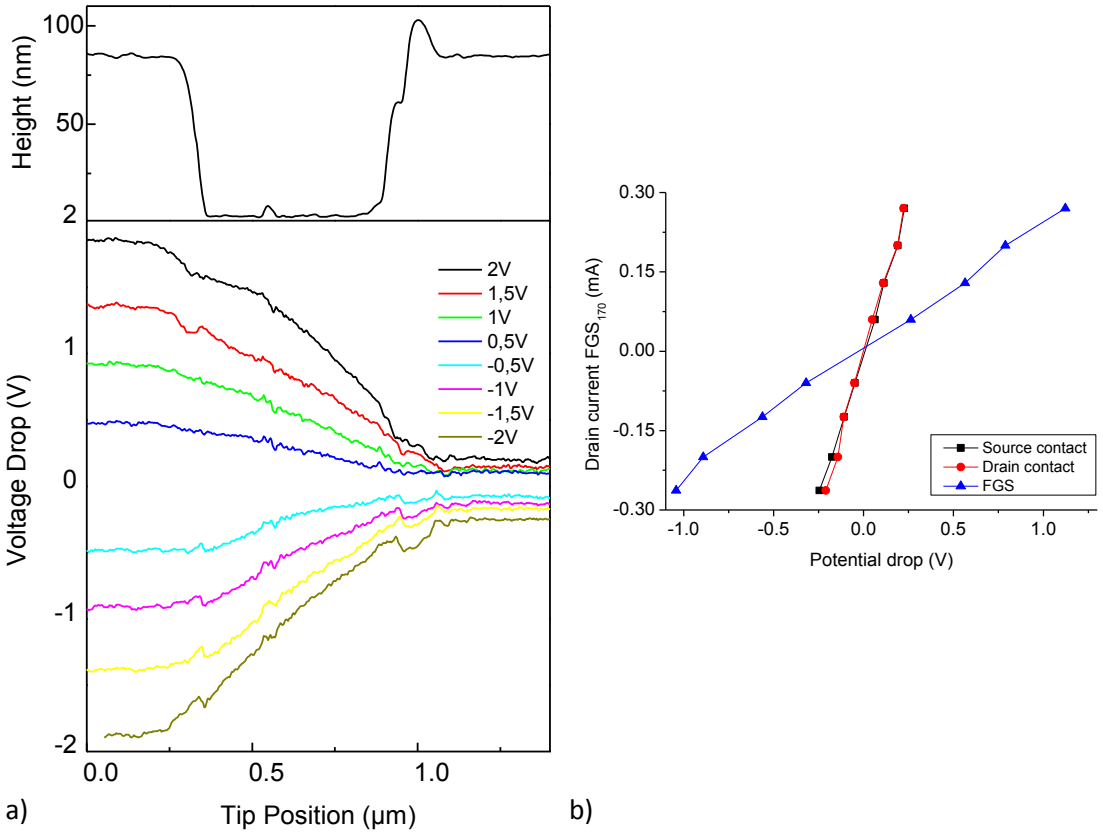

Figure 5.12: (a) KPFM voltage drop of a FGS_{170} device and (b) KPFM-determined IV curve of the drain contact, graphene channel and source contact.

studied. Therefore it is suggested that in order to obtain ρ_s of 10 k$\Omega/\square$ and below, a sufficient reduction of both the oxygen content and the defect density is necessary. Thermally, this can only be achieved at temperatures in excess of 1000^{o}C at which the onset of structural changes in graphene has been observed [171]. Defects in the carbon backbone that emerge upon thermal reduction at lower temperatures, e.g. through the reduction of epoxide groups, [172, 173] can be reduced in number through such thermal annealing [171]. Unlike in the case of substrate processing with thermally exfoliated and reduced FGSs, such high annealing temperatures can be achieved, resulting in the low resistances observed. It is proposed that the combination of chemical and thermal reduction on a substrate yields high conductivities because the chemical reduction step likely results in either the absence or a largely decreased density of lattice defects compared to thermal reduction-only approach at temperatures up to 1000^{o}C.

5.5 Conclusions

In summary, KPFM analysis was successfully applied to the characterization of the contact and sheet voltage drops in submicrometer, two-terminal single FGS devices, which ranged from low C/O ratio to high C/O ratio samples. The increase of C/O ratio in FGS samples is accompanied by a decrease in resistance and a linearization of the IV curve due to a restoration of the sp^2 carbon to carbon network. Using KPFM, it can be concluded that the observed non-linear IV curves at low C/O are due to a combination of intrinsic hopping charge transport at the channel and Schottky characteristics at the FGS-metal contacts superimposed by an ohmic behavior onset and/or a tunneling contribution, happening before the sp^2 network recovery reaches the percolation limit. At high C/O values, the diffusive charge transport mechanism can be observed in the linear voltage drop behavior of the contacts and the FGS channel, rendering FGS-metal ohmic contacts.

The thermal exfoliation and reduction of GO are shown to yield FGSs with a wide range of electrical properties, depending on the exfoliation and reduction protocol. With increasing reduction time and temperature, a transition is observed from non-ohmic high-resistance of $\rho_s > 400$ k$\Omega/\square$ and $\rho_c > 100$ k$\Omega\mu$m to ohmic low-resistance of $\rho_s < 10$ k$\Omega/\square$ and $\rho_c < 1$ k$\Omega\mu$m. The efforts on the characterization of contact and sheet resistance values of single FGS flakes are focused on the general behavior of this material. This investigation makes a precedent for the characterization and understanding of the operation of FGS conductive networks, such as in conductive inks.

Finally, the KPFM voltage drop analysis performed in this investigation shows the potential of this technique as an alternative for the electrical characterization of single devices with unique morphologies and limited dimensions, where conventional techniques such as 4p or TLM cannot be directly applied. As well as the capability to analyze the potential drops of the electrodes independently, which enables to differentiate between the linear or non-linear behavior of individual contacts and/or channel.

Chapter 6

Contact resistance in CVD graphene-based devices

Two principal divisions of the semiconductor industry are the digital logic and the radio frequency electronics. Due to its gapless nature, graphene has a larger potential on radio frequency rather than on digital logic applications. Radio frequency applications make use of High-Electron-Mobility Transistors (HEMTs) often based on SiGe or III-V compounds, such as GaAs and InP. With graphene′s electron mobility reaching up to 10^6 cm^2/Vs compared to that of III-V compounds with low band gaps being close to 10^5 cm^2/Vs its potential for these applications is highlighted [43].

The characterization of graphene-based transistors for high frequency applications can be done with established parameters, such as the cutoff frequency (f_T) and the maximum frequency of oscillation (f_{max}) [15]. These values mark the upper frequency limits at which the transistors start to loose their ability to amplify; f_T is the frequency at which the current gain has dropped to unity and f_{max} the frequency where the power gain equals one. Hence, both f_T and f_{max} are required to be as high as possible. Figure 6.1a and Figure 6.1b are a comparison of graphene against established HEMT′s semiconductor technologies for f_{max} and f_T, respectively. It can be seen that while graphene is competitive against III-V compounds in f_T values (CVD graphene included), it falls way behind in the f_{max} values.

The main cause of the low values of f_{max} is the large drain conductance g_{ds} (dI_{ds}/dV_{ds}) caused by the absence or low saturation of the drain current, where high contact resistances may play a role [174]. Indeed, from the definition of f_T and f_{max}, an indirect relation to $R_{c,d}$ and $R_{c,s}$ can be found, while having a proportion to the

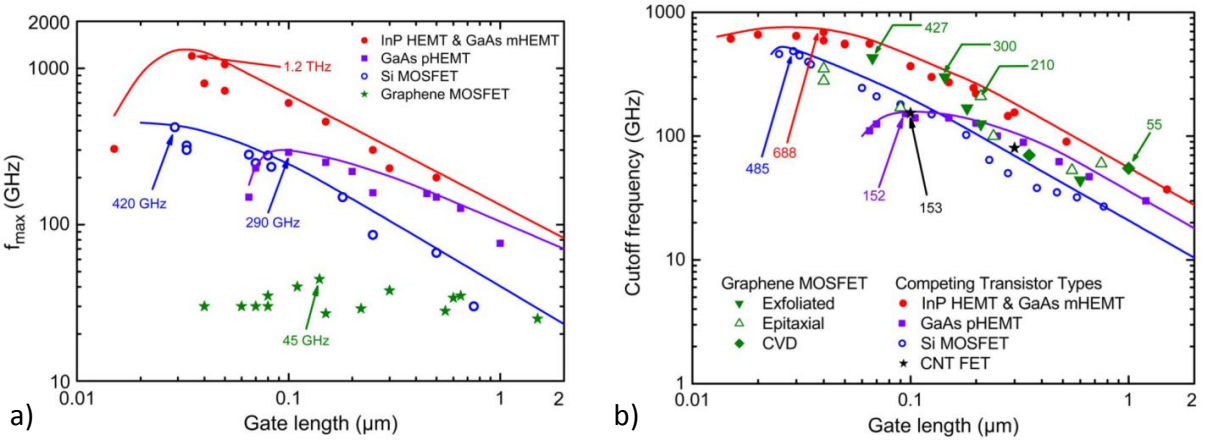

Figure 6.1: Graphene-based transistors compared against established semiconductor technologies for (a) the maximum frequency of oscillation (f_{max}) and (b) the cutoff frequency (f_T) versus gate length. Images taken from [15].

transconductance g_m (dI_{ds}/dV_{gs}), [43] such as

$$f_T = \frac{g_m}{2\pi(C_{gs}+C_{gd})} \frac{1}{1+g_{ds}(R_{c,s}+R_{c,d})+\frac{C_{gd}g_m(R_{c,s}+R_{c,d})}{C_{gs}+C_{gd}}}$$

$$f_{max} = \frac{g_m}{4\pi C_{gs}} \frac{1}{\left(g_{ds}(R_i+R_{c,s}+R_g)+g_m R_g \frac{C_{gd}}{C_{gs}}\right)^{1/2}}$$

where R_g is the gate resistance, R_i the intrinsic resistance of the transistor and C_{gd} as well as C_{gs} are the drain and source gate capacitance, respectively.

Hence, it can be followed that the resistivity ρ_c of the contacts has a contribution to g_{ds} and g_m as well as to f_T, f_{max}, such that

$$f_T = f(g_m, \rho_c, \rho_s)$$
$$f_{max} = f(g_m, \rho_c, \rho_s)$$
$$g_m = f(\rho_c, \rho_s)$$

It is then clear that the study and reduction of resistance at the electrical contacts is aligned to the improvement of graphene-based transistors for high frequency applications. The different causes influencing contact resistance can be:

1. **Contact material:** The work function of the materials used as contacts could

create barriers either due to the work function mismatch and/or the doping of the channel, induced by the contact material in the vicinity of the interface [175, 176].

2. **Field-effect:** The field effect generating carriers in the graphene channel also affects the graphene under the metal and thus a dependence of the contact resistance to V_{gs} has been observed. This can be related to the issues mentioned above, creating space-charge regions between adjacent areas with different doping [177, 178].

3. **Contact design:** It has been stated that graphene tends to create weak bonds out-of-plane [179, 180]. The customary approach for the design of graphene devices is the placement of metal above an area of graphene known as top or 2D contacts. However, by making use of graphene′s thickness it has been shown that contacts over the edge of graphene, i.e. 1D contacts, have an influence on reducing the contact resistance [17].

4. **Fabrication issues:** Also the fabrication process can have an impact on contact resistance. Although it has been observed that some traces of residues can be found on the graphene surface after the transfer and/or fabrication process, still no direct imaging of such residues and its thickness have been reported [181, 182]. Also, it is yet to clarify to which extent the residues cover the graphene surface, whether these residues affect permanently the material and/or if there is any dependence to a particular fabrication process.

This chapter is dedicated to the study of contact design and fabrication issues on the contact resistance of CVD graphene-based devices. First, a comparison is made between devices produced by optical lithography and e-beam lithography. The voltage drops at the contacts and over the channel are examined by KPFM analysis. Consequently, the influence of standard optical lithography process on graphene is further studied, with a combination of AFM patterning, Raman mapping and KPFM analysis. The chapter continues following the results of the fabrication issues by exploring the effect of 1D contact design in optical lithography fabrication processes. Devices fabricated with a modification of the customary approach of 2D contacts, which aims to produce metal/graphene contacts only over the edge of the channel, are characterized by a combination of TLM and AFM/KPFM analysis. The slight modification of the fabrication process, done by our partners at AMO GmbH, is stated and it will be discussed how this modification results in homogeneous, damage-free contacts over the edge of graphene. Parts of the results in this chapter are reported in the author′s publications [16].

6.1 Experimental procedure

To confirm a possible difference of the ρ_c between e-beam and optical lithography graphene devices, colleagues at AMO GmbH prepared several operational devices by both methods using the customary approach, i.e. top contacts. Both lithographic procedures used commercial graphene grown on Cu foils by CVD (Graphenea, S.A. de C.V.). The PMMA-assisted wet transfer method was used to deposit graphene onto a p-doped Si substrate with 90 nm thermally grown SiO_2 layer. The structuration of the channel and the metallization of the contacts of one type of devices were prepared by standard e-beam process using PMMA as the resist. Another batch of devices was prepared by an optical lithography process using AZ5214E (*MicroChem corp*) as the resist. For the contacts, 20 nm and 80 nm of Ni were deposited by sputter deposition and lift-off technique on optical and e-beam samples, respectively. To examine the process residues left by optical lithography on the graphene surface and thus, in the metal/graphene interface, a 1 cm^2 of the same type of graphene was transferred to the same type of substrate as mentioned before. The large area of this reference sample was deliberately chosen to clarify if any, the presence and the surface coverage of the residual layer. Once the graphene was transferred from the copper to the substrate and the PMMA sacrificial layer was removed, the sample was further treated with the standard lithography process used for the device fabrication. The optical resist was used as in the fabrication of the metal contacts. However, no metallization was done, i.e. the surface of the whole sample resembles that of the graphene before the metal contact placement, thus giving us the opportunity to study the conditions between metal and graphene surface in operational devices. These procedures are described in detail in section A.2.

The KPFM voltage drop analysis as well as the Raman spectroscopy measurements were taken with the *NT-MDT Ntegra Spectra* system in ambient conditions. Silicon probes (*Budget sensors*) with a $\omega_0 \sim 66$ kHz, nominal radius of < 25 nm and a conductive Cr/PtIr coating on both sides of the cantilever were used. For mechanical patterning, the AFM was used in contact mode with a scan rate of 1 Hz and a contact force of 50 - 100 nN. The patterning procedure was performed three times to ensure complete removal of the residue layer. The measurements of operational devices and the reference samples by KPFM were done in single-pass PM mode, with a modulation voltage of $V_{ac} = 1\ V_{p-p}$ at a frequency of $\omega_{ac} = 2.5$ kHz sent to the tip, while the source contact of the devices was grounded. For the Raman measurements, a 532 nm laser with < 1 mW power was used, focused by a long-distance 100x objective with a NA of 0.7.

6.2 Comparison of e-beam and optical lithography processed devices

The analyzed devices in this section are produced by the customary approach as stated above and detailed in section A.2. First, topography and surface potential mapping of the devices were taken for both lithography processes. In Figure 6.2a (bottom), the topography map of an optical lithography processed device can be seen with the drain and source contacts centered in the image. Here the graphene channel is covering the whole width and length of the image. The extracted line profile (average of 11 lines) is shown in Figure 6.2a above the topography map and marked as dashed line in the image. In Figure 6.2b (bottom) the corresponding KPFM map at $V_{ds} = 0$ V is shown. The analyzed area for voltage drop corresponds to that between the inner contacts, marked with dashed line rectangle at the corresponding averaged line profile of Figure 6.2b (top) for a $l \sim 8$ μm and $w \sim 14$ μm. Similar V_k values ($\sim$ 230 mV) can be seen in both electrodes clearly distinguishable from the graphene channel ($\sim$ -50 mV). The spatial distribution of the CPD inhomogeneity in the channel suggests doping variations, however, no large inhomogeneity is present in the area selected in the channel for voltage drop analysis. The KPFM map at $V_{ds} = 1$ V is shown in Figure 6.2c (bottom). The voltage applied can be clearly followed in the contrast change over the whole area of the drain contact displaying a fully operational contact. This change can also be seen in the extracted line profile (Figure 6.2c, top) with a ΔV between the drain and source of 0.96 V. The homogeneous and gradual voltage drop in the graphene channel at +1 V suggests equivalent conductive paths.

The KPFM voltage drop measurements of optical lithography devices (Figure 6.3) are obtained as stated in section 3.2.7 from the information shown above. Here large and sharp voltage drops at the metal/graphene interface at the drain and source contacts can be observed, which are used to calculate R_c for every V_{ds} applied. Consequently, these results are averaged and the reported ρ_c is determined using the geometrical dimensions of the device. The calculated ρ_c here is about 4 k$\Omega\mu$m for both contacts, reaching up to 30 k$\Omega\mu$m for other devices with the same production process. Similarly, the voltage drop over the channel was used to calculate an averaged ρ_s of about 590 $\Omega/\square$ reaching up to 900 $\Omega/\square$ for other similar devices.

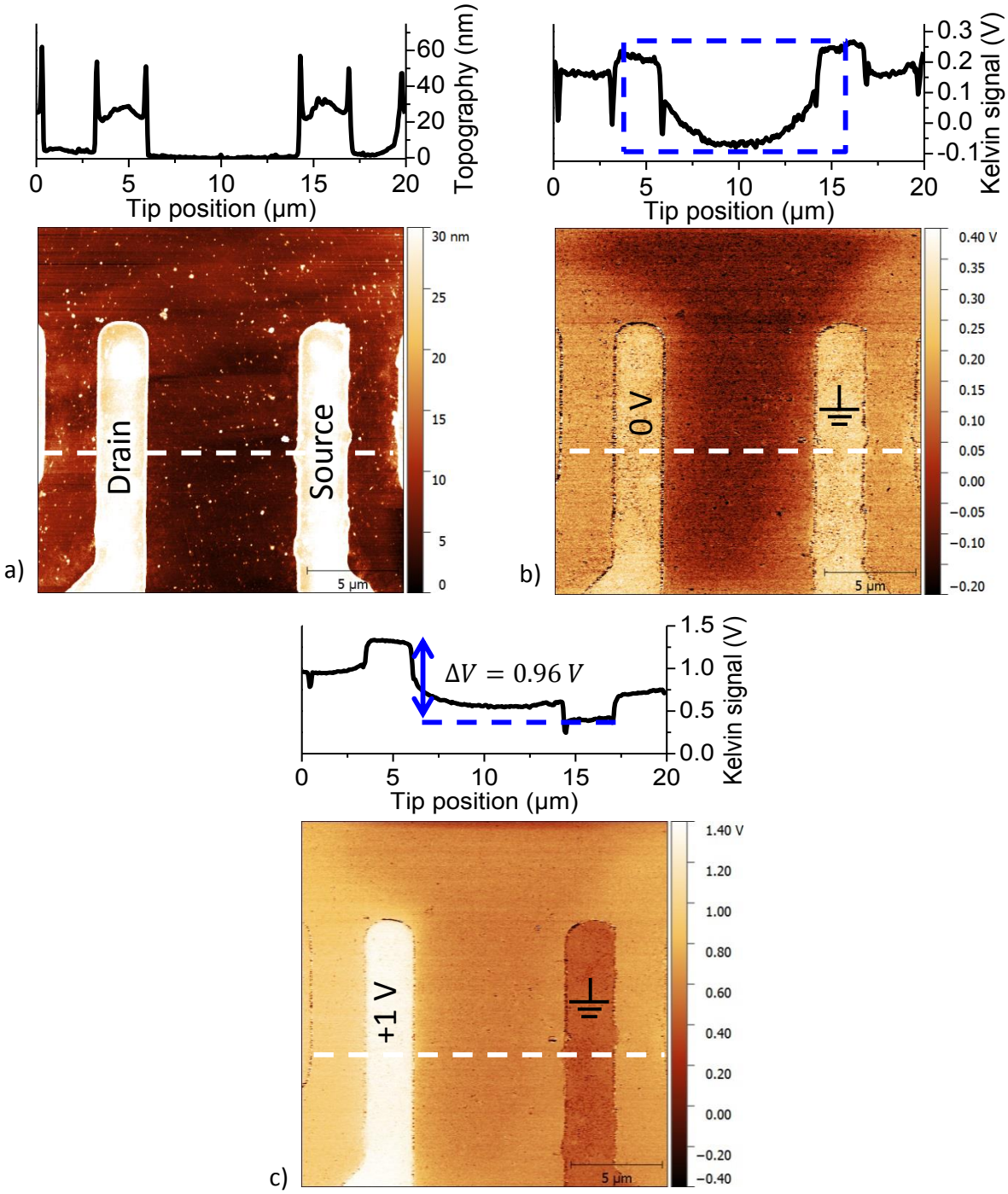

Figure 6.2: Maps (bottom) and extracted averaged line profiles (top) of the (a) topography, (b) KPFM $V_{ds} = 0$ V and (c) $V_{ds} = +1$ V of a top contact device fabricated by optical lithography. The analyzed area corresponds to the inner contacts.

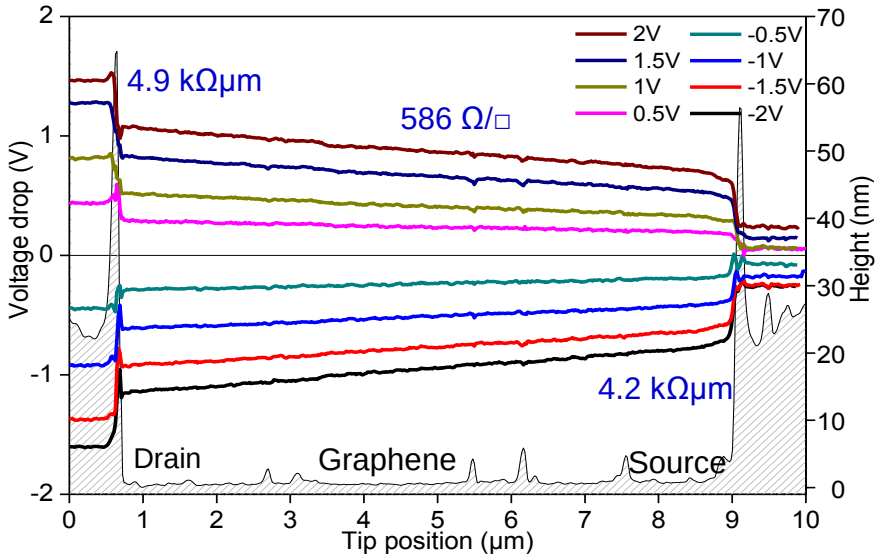

Figure 6.3: KPFM voltage drop analysis of a representative graphene top contact device made by optical lithography. The voltage drops can be clearly separated for ρ_c (4.9 k$\Omega\mu$m at the drain and 4.2 k$\Omega\mu$m at the source contact) and ρ_s (586 $\Omega/\square$).

Top contact devices prepared by e-beam lithography were also analyzed by KPFM and its information was extracted and processed as presented above. In Figure 6.4 an e-beam processed device, with $l \sim 1.5$ μm and $w \sim 8.5$ μm, presents a smoother and much lower voltage drop at the interface compared to the optical processed devices, while the graphene channel behaves similarly. For this device a ρ_c up to 540 $\Omega\mu$m and a ρ_s of 700 $\Omega/\square$ were calculated. Macroscopic TLM measurements, done independently by AMO GmbH, were performed on several samples from different runs (more than three each), always resulting in ρ_c values of 0.1 – 1 k$\Omega\mu$m for devices fabricated by e-beam lithography, while devices fabricated by optical lithography always showed values larger than 4 k$\Omega\mu$m. Within error, the calculated top limits of ρ_c of KPFM measurements correlate with the values obtained by the macroscopic method.

The KPFM measurements were done in a statistically relevant manner about 20 measurements on 3 optical and 3 e-beam lithography derived devices. The calculated values of contact and sheet resistivity are presented in Figure 6.5a and Figure 6.5b, respectively. From Figure 6.5a the difference of up to one order of magnitude between ρ_c of e-beam and optical lithography processed devices is clearly distinguishable. This difference clearly demonstrates the impact of the used lithography process on the metal/graphene interface and its electrical resistance. In contrast, no variation of the sheet resistance has been found for the two different approaches (Figure 6.5b).

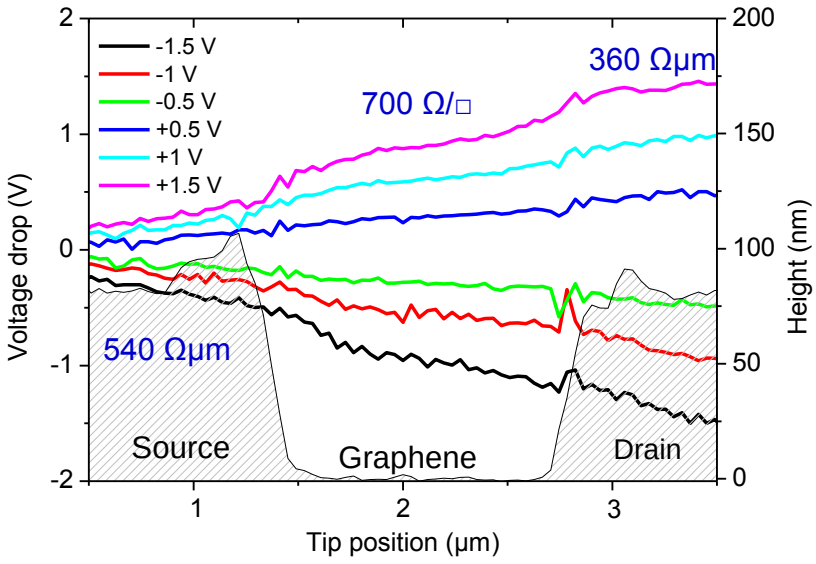

Figure 6.4: KPFM voltage drop analysis of a representative graphene top contact device made by e-beam lithography. The averaged small voltage drops at the contacts represent a ρ_c of 360 $\Omega\mu$m at the drain contact, 540 $\Omega\mu$m at the source contact and ρ_s of 700 $\Omega/\square$ for the channel.

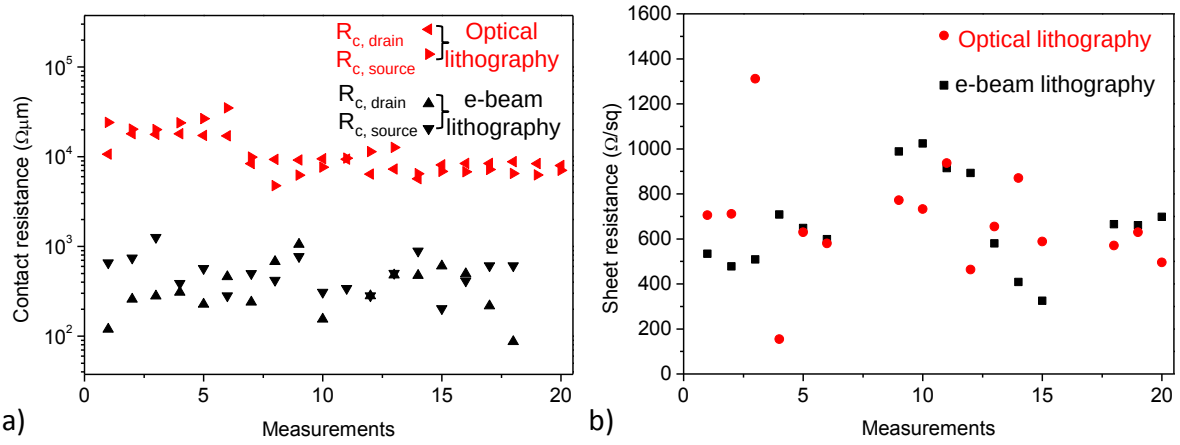

Figure 6.5: Summary of the results of (a) contact resistance and (b) sheet resistance derived from KPFM measurements for different devices prepared by optical and e-beam lithography.

The lack of a trend in the results of sheet resistance in Figure 6.5b could be a hint that optical lithography does not have a lingering effect on graphene, i.e. no structural or chemical changes occur during the fabrication process.

6.3 Presence of process residual layer

Apparently, PMMA and the use of e-beam lithography yield devices with lower ρ_c compared to those produced by optical lithography. This is consistent with literature reports where ρ_c of e-beam devices of several hundreds of $\Omega\mu$m can be found [183], while for optical lithography devices it is common to obtain values of some few, up to several tens of k$\Omega\mu$m [184, 185, 186, 181]. This observation has been investigated by means of XPS [181] and roughness analysis [182], indicating that layer(s) of residues play a role in the high contact resistivity for optical lithography processed devices. Out of these investigations, it was not clear whether the residues cover the surface of graphene entirely or partially, the spatial homogeneity, the thickness of the residue layer and/or whether graphene itself has been intrinsically modified.

There have been attempts to measure the residue layer of e-beam derived devices. Dan et al. [187] measured 1 nm of thickness of a residual PMMA layer similar to the observation of Cheng et al. [188] who found 0.7 nm. However, less is known about optical lithography derived devices. Ishigami et al. [189] could not perform scanning tunneling microscopy on a graphene surface and therefore assumed a layer of optical resist residues without further investigation. Li et al. [182] measured an rms roughness of 7.89 nm directly after developing the optical resist, which could be reduced to 1.49 nm by UV ozone treatment. Nevertheless, even after this roughness reduction, there is no evident proof whether the residue layer was completely removed or just its surface was smoothed since the thickness of the assumed residue layer was not measured. These organic residues are also found in the semiconductor industry and are easily removed with a treatment of ozone plasma. However, this same approach cannot be used for graphene since the treatment removes the residues as well as graphene from the substrate.

In order to determine whether the graphene layer is intrinsically modified due to the process or indeed a residual layer of the organic resist is left behind, a 1 cm^2 graphene samples was processed by optical lithography without the metallization step (details in section A.2) and used as a reference sample to study the graphene surface beneath the contacts in operational devices. A 100x optical image of this reference sample can be seen in Figure 6.6a. Intentionally an area close to a defective region was chosen, where the uncovered SiO_2/Si substrate is visible which can help for orientation and identification. On this same area, a 5 μm $\times$ 7.5 μm area was mechanically patterned by an AFM tip in contact mode to remove a possible residue layer as illustrated in Figure 6.6b. From the contrast in the optical images, it can be seen that indeed a residual layer was removed.

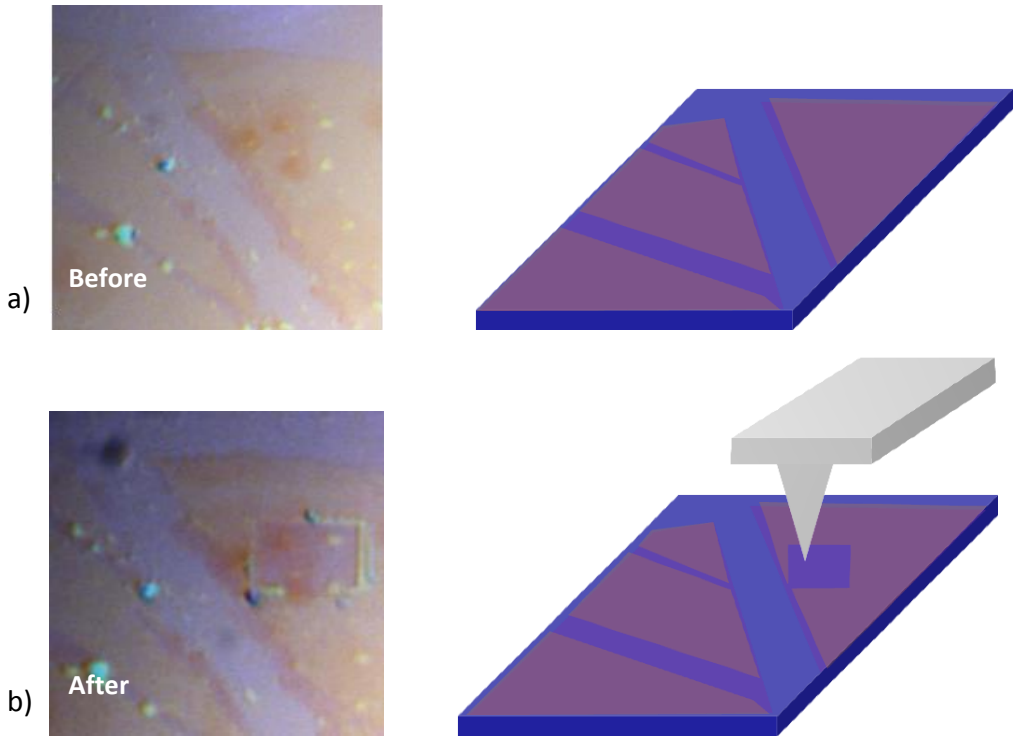

Figure 6.6: 100x optical images (left) and schematization (a) before and (b) after the AFM patterning of the optical resist residues on graphene.

The size of the pattern was chosen for two reasons: it is small enough to ensure that the patterning will be able to fully remove the layer, i.e. the scan/patterning step ($\sim$ 14 nm) will be equal or less than the end-diameter of the AFM tip ($\sim$ 25 nm). Second, it is large enough to be seen by our built-in 100x optical microscope, allowing us to compare *in-situ* before and after the removal.

Raman spectroscopy is performed to assess the presence of the residual layer and, if any, damage to the graphene sheet due to the AFM patterning procedure. In Figure 6.7a and Figure 6.7b Raman maps of the 2D to G peak intensity ratio (see subsection 3.3.1), are shown before and after processing, respectively, calculated as integrated area using a Lorentzian spectral shape [190]. The presence of FLG and MLG regions (low 2D/G values) can be seen at the center of the maps, surrounded by areas of SLG (high 2D/G values) and the substrate. Since the residual layer is homogeneous and continuous (not island-like accumulations) and since from Figure 6.7a it is evident that the Raman signal of graphene is not affected by the residues, the presence of this layer can easily be unnoticed. This observation is of great importance, since investigations that deal with contact resistances and improvement procedures, which overlook the presence of an interfacial residue layer

between graphene and metal, can lead to reported results with compromised data. In Figure 6.7b, an increase of the 2D/G intensity ratio can be seen in the patterned area (dashed line box), especially in the area of SLG, however, the presence of the residual layer itself is still not clearly distinguishable. The increase of the 2D/G ratio might indicate an enhanced doping level of the graphene due to the residual layer [45, 190, 191, 192], however, as no trend was observed in the results of ρ_s from TLM measurements, this might be rather an indication that the electron-phonon scattering of the 2D-mode peak is affected slightly by the residue layer [193].

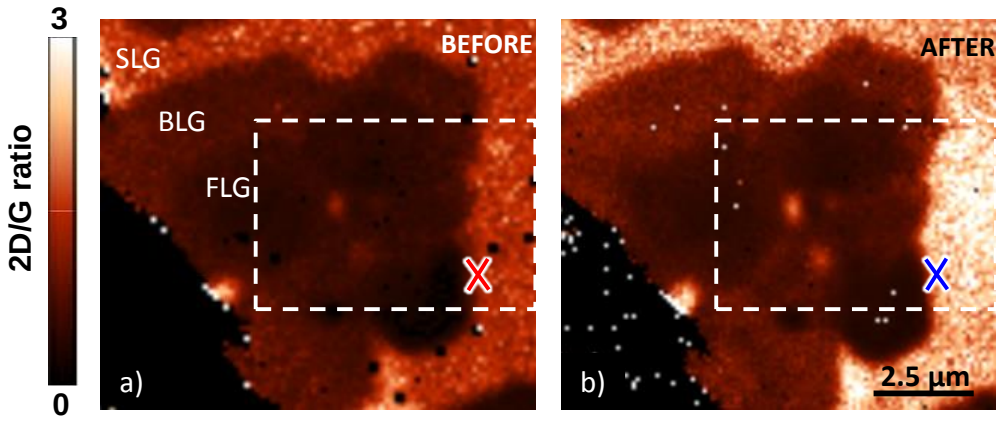

Figure 6.7: Raman maps of the 2D/G peak intensity ratio of the investigated area (a) before and (b) after the AFM patterning. The patterned area is indicated by the dashed line rectangle. Single Raman spectra were extracted from the position marked with crosses.

To confirm whether the mechanical treatment affects the graphene itself, single spectra were extracted from the Raman maps indicated by the crosses in Figure 6.7 from nominally the same position before (red) and after (blue) AFM patterning. The extracted spectra are shown in Figure 6.8. Here it can be seen that both, the 2D- and the G-mode peaks are visible without any indication of the defect-induced D-mode peak at around 1350 cm^{-1}. This clearly proves that the AFM patterning removed a residual layer without damaging the graphene underneath.

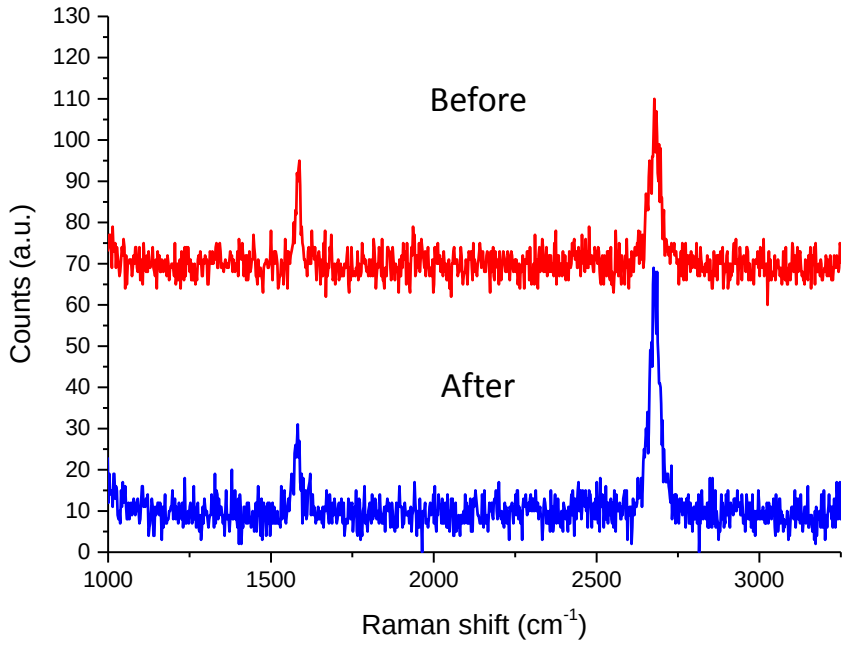

Figure 6.8: Spectra extracted from nominally the same position of the Raman map before (red line) and after (blue line) AFM patterning of the residual layer. The absence of the D-mode peak confirms that the AFM patterning does not damage the graphene sheet.

Due to the high sensitivity of KPFM to small work function differences, this technique was applied to compare the AFM patterned area to the rest of the sample. The KPFM map of the same area is shown in Figure 6.9a, where a clear contrast between (A) AFM patterned areas (where the residual layer is at least partially removed) and (B) the untreated areas (areas still covered by optical resist residues) can be observed. In addition, the uncovered SiO_2 area can also be clearly identified. In order to compare the Kelvin voltages of each area, mean values have been determined from the histograms (Figure 6.9b).

A Kelvin voltage of $\sim$ 0.39 V is determined for the AFM patterned area (A in Figure 6.9a), $\sim$ 0.52 V for the covered graphene (B in Figure 6.9a) and $\sim$ 0.56 V for the SiO_2 region. An additional area in the KPFM map can be seen with a V_k of about $\sim$ 0.38 V occurring along the SiO_2 areas, which can be attributed to uncovered graphene, excavated by sample handling. As the absolute value of the Kelvin voltage depends on the work function of the used tip, the discussion is focused on the work function differences between the various areas of interest. A Kelvin voltage difference of about $\sim$ 0.12 V is found between the AFM patterned and the covered graphene areas. In contrast, the Kelvin voltage of the uncovered graphene ($\sim$ 0.38 V) and the AFM

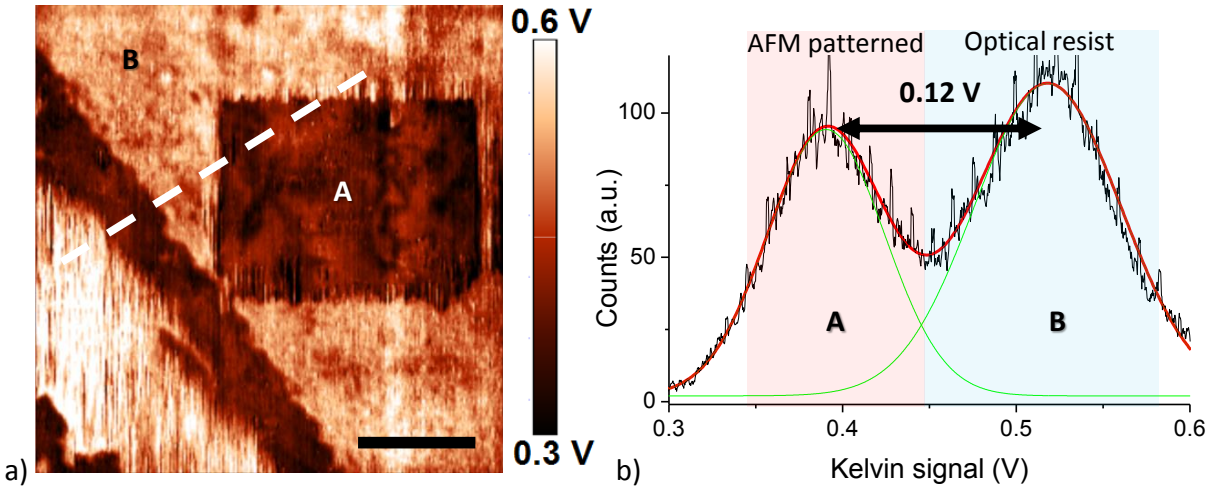

Figure 6.9: (a) KPFM map of the graphene sample where the surface potential of the (A) AFM patterned area, (B) optical resist residual layer and substrate are visible. Scale bar: 4 μm. The extracted line profile is indicated by the white dashed line in (a). (b) Histogram extracted from the KPFM map (black line) and peak fit (red line). The deconvolution of the peaks fit (green line) shows the distribution values of graphene and optical resist areas.

patterned area ($\sim$ 0.39 V) is similar, confirming that the graphene layer itself is not noticeably modified after removing the residual layer. From this observation, along with the sheet resistance measurements (see Figure 6.5) and the absence of a D-mode peak in the Raman spectra (see Figure 6.8), it can be concluded that the optical resist residues are only physically adsorbed and not chemically bonded to the graphene surface and can thus be removed by AFM patterning.

The AFM topography maps of the same areas before (Figure 6.10a) and after patterning (Figure 6.10b) confirm that the patterning leads to the removal of a layer of about 3 – 4 nm thick as derived from the data. Comparing this value with the thickness of the residual layer of 0.7 – 1 nm typically observed in case of electron beam lithography [187, 188] gives a clear hint why the contact resistance is much higher in case of optical lithography than in case of electron beam lithography.

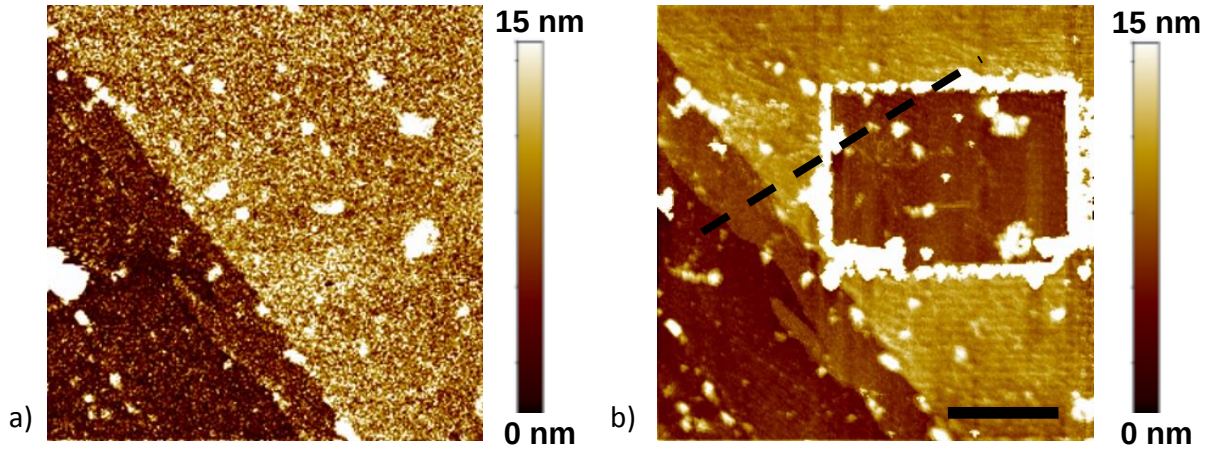

Figure 6.10: AFM height map of the selected area (a) before and (b) after contact mode patterning. Scale bar: 4 μm. The black dashed line in (b) indicates the extracted line profile.

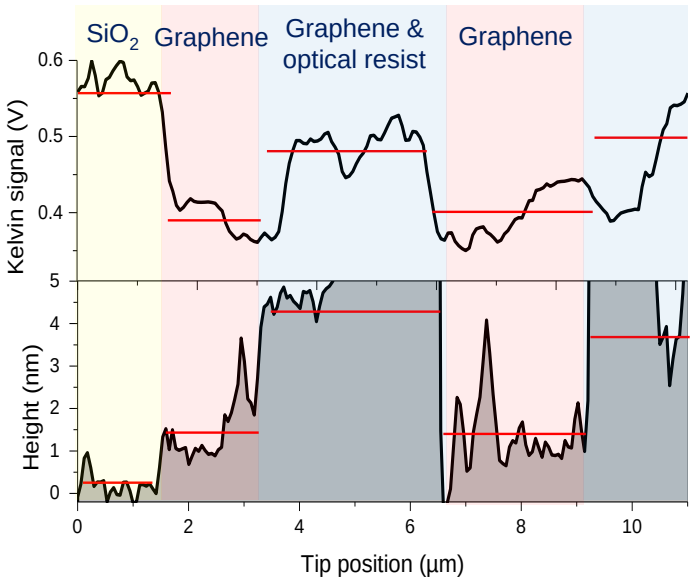

Figure 6.11: Graph of the line profiles extracted from the topography (bottom) and KPFM (top) map. The red lines represent the average values within each area.

Figure 6.11 shows the averaged scan of 11 lines (dashed lines in Figure 6.9a and Figure 6.10b) of the (top) Kelvin voltage and the corresponding (bottom) topography. The red lines represent the average values. Evident Kelvin voltage steps can be seen between the different areas as discussed above. From the topography measurements, a

height step of $\sim$ 1.1 nm from the SiO_2 to the graphene areas can be deduced, in very good agreement with literature values [188, 189, 194]. From this data a r.m.s. roughness of $\sim$ 0.99 nm for the covered area is extracted, which is comparable to the value that Hsu et al. measured using the same optical resist [184]. Compared to the r.m.s. surface roughness of 0.54 nm for the residues remaining on graphene after e-beam lithography [188], this is a nearly two times increased value and could thus be an additional reason for the high contact resistance. After AFM patterning the roughness decreases to $\sim$ 0.56 nm, which is very close to the roughness of the underlying SiO_2 substrate of $\sim$ 0.41 nm. This along with similar KPFM values for uncovered and patterned graphene areas indicates a virtually complete removal of the optical resist residual by the AFM patterning.

Following these results, it is evident that the high contact resistance of optical lithography processed devices must have a direct relation with the residual layer on top of graphene. Thus, the surface of the sample must be treated prior the metal contact placement and/or other contact architectures must be used in order to overcome this issue and reduce ρ_c.

6.4 Production scheme for edge contact graphene devices

Treatments to reduce the ρ_c of graphene devices can be found in literature mostly in the form of cleaning steps before [182] and after [183] metallization of the contacts. Also for this objective, the effect of metal/graphene work function differences have been studied using different metals as contacts [195] without obtaining a clear trend and/or control which could be consistently replicated. All of these experiments used the standard fabrication procedure, i.e. top contacts. Here the metal contact area is distributed over the surface of graphene injecting charges from/to graphene vertically (out-of-plane). It has been stated that graphene has poor out-of-plane conductivity due to weak van der Waals bondings, while having a very good in-plane conductivity due to covalent bondings [179]. Moreover, as seen before in this chapter, in the case of optical lithography devices the presence of a residual layer can be expected.

In 2013, a new contact architecture between metal and graphene was reported [17]. Using the intrinsic thickness of graphene, and thus of basically any 2D material, a punctual contact between the edges of graphene and metal can be obtained, also known as 1D contact. Making this horizontal contact over the edge of the graphene channel width, and not over the surface, it is expected that charges are injected in-plane from/to graphene. The reported improvements in ρ_c are expected to be based on avoiding graphene′s poor interlayer conductivity [196]. However, the reported procedure is rather complicated and not straightforward, as it requires a stack structure of graphene between two layers of hexagonal Boron Nitride and the metal deposition with an acute contacting angle.

A simplification of the above mentioned method has been proposed by colleagues at AMO GmbH. With a small change of the standard optical lithography production scheme, graphene/metal edge contacts can be obtained in a much more accessible way. This simplification requires the graphene contact structuration and metallization step to be merged, which main difference can be stated as removing graphene before metal placement. The difference to the customary approach is exemplified in Figure 6.12 and detailed in section A.2. Starting from a transferred graphene sample, the areas onto which the metals will be evaporated are defined and exposed to oxygen plasma to have graphene deliberately removed from the substrate. The metal is then evaporated onto the sample, placing itself on the substrate i.e. no graphene is underneath the metal. The process continues as in the standard approach by using a different mask to define the channel and

remove the excess of graphene.

The edge contact devices analyzed here were produced by AMO GmbH using commercial CVD graphene grown on copper foil and wet transferred onto a 90nm SiO_2/highly p-doped Si substrate. The entire steps of device fabrications were conducted with optical lithography and AZ5214E as the resist. This allows comparing the influence of contact design on ρ_c. Using one mask, graphene is removed by 30 s of O_2 plasma treatment followed by the placement of sputtered Ni/Al (15/120 nm) contacts. A different mask was used to structure the device's channel with O_2 plasma for 2 min for a final TLM layout.

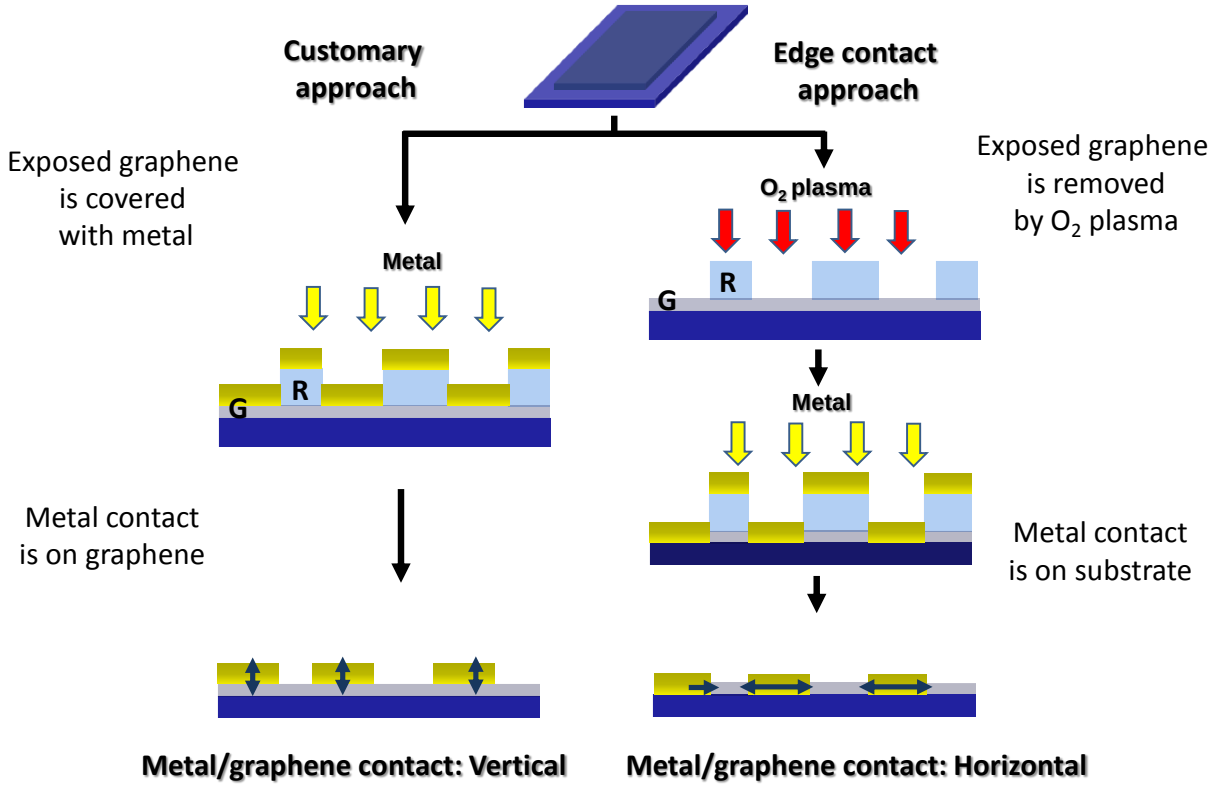

Figure 6.12: Simplified schematic comparison of the main difference between the customary (left) and edge contact (right) approach for the fabrication of graphene devices. For edge contacts, graphene is removed from the substrate before the placement of the metal contacts. G and R stand for graphene and optical lithography resist, respectively.

6.5 Macroscopic electrical characterization of edge contact devices

The TLM layout of the graphene devices fabricated by the edge contact approach have contact separation lengths of l = 1.5, 3.5, 5.5, 7.5 and 9.5 μm, respectively with three different channel widths of w = 1.5, 4 and 15 μm (Figure 6.13a). The measured R_{2p} is normalized by the respective w and plotted versus l in Figure 6.13b. Every device was measured several times at different voltages and polarities, $V_{ds} = \pm$ 0.1, $\pm$ 0.2, $\pm$ 0.5, $\pm$ 1 and $\pm$ 2 V to study R_{2p} variations. The results were averaged for the TLM plot and their normal distribution shown as an error bar. The measurements were done in air at a *PM5* probe station using a *Keithley* 2612 as the SMU without any gate voltage applied.

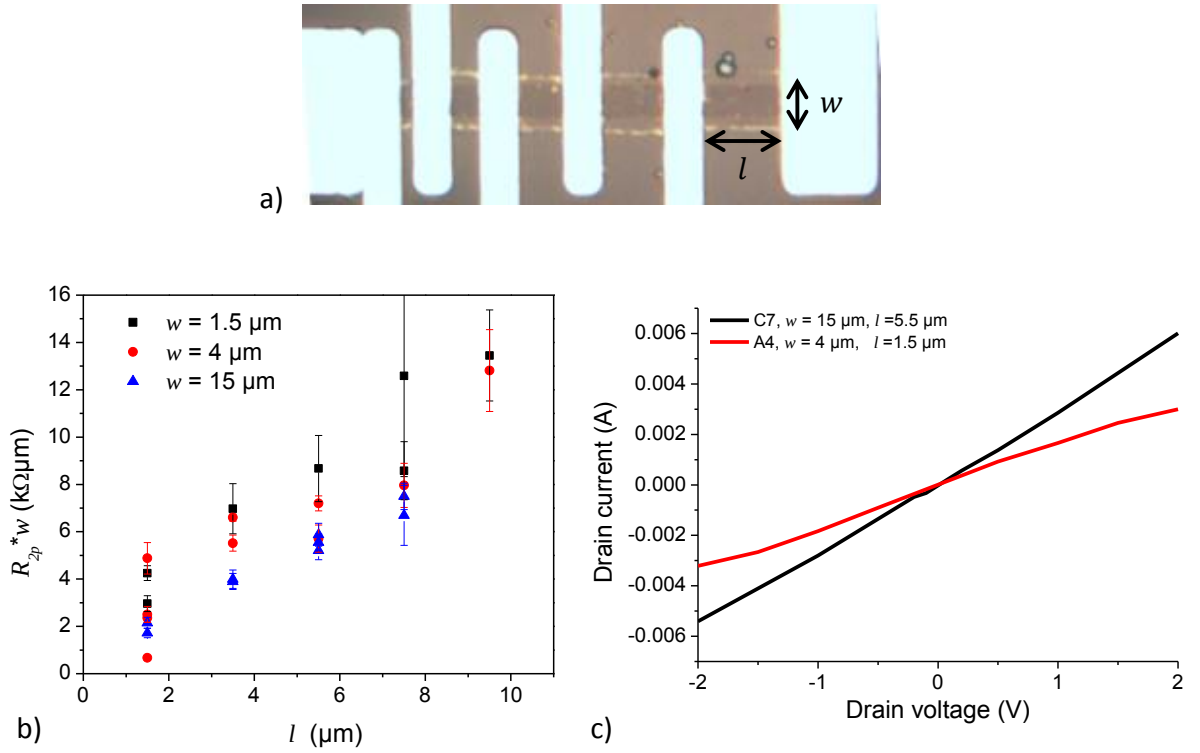

Figure 6.13: (a) A 100x optical micrograph of a graphene edge contact TLM layout (w = 4 μm). The (b) $R_{2p} * w$ vs l graph of the measured devices for three different widths at varying V_{ds} voltages, where the variations within the same devices are shown as an error bar. (c) Linear IV characteristics of representative edge contact devices with different dimensions.

Even with the absence of gate-induced doping in graphene, it can be fairly concluded, from the TLM measurements, that the intercept of the linearization has a tendency to values below the usual 4 k$\Omega\mu$m of optical lithography devices (see section 6.2), suggesting already a reduction of ρ_c compared to 2D contacts. During the measurements, a scattering of R_{2p} as V_{ds} increased was observed within devices. Between devices, the scattering was noted to be proportional to l for all widths, while inversely proportional to w, i.e. wider devices have less scattering compared to their narrow counterparts for any given l. Since the devices showed linear IV behavior for relatively fast V_{ds} sweeps (Figure 6.13c), the observed scattering could be explained as defects in the channel having a more crucial effect on the electrical characteristics for narrow devices. As ρ_c approaches values close to zero the scattering within a device and/or between devices over the length of the layout, can increase the error margins for the TLM linear fit and its intercept, which could render erroneous negative ρ_c. While not all devices within the same TLM layout presented these variations, even if individual devices operate with reduced ρ_c due to edge contacts, the correct estimation can be hindered by the TLM requirement of a linear fit. Therefore, to corroborate the suggested reduction of ρ_c by TLM measurements, a KPFM voltage drop analysis is performed in single two-terminal devices for an individual estimation of ρ_s and ρ_c.

6.6 KPFM voltage drop analysis of graphene edge contact devices

The selected devices for the KPFM analysis displayed a reduced R_{2p}, for their specific geometries, which potentially could be caused by a decrease of ρ_c due to the effect of the edge contact. The KPFM analysis were performed in air on a *NT-MDT Ntegra Spectra* system. Bond wires were used to connect the devices to a *Keithley* SMU 2612 for *in-situ* electric measurements. Produced by optical lithography, the graphene channels presented also a residual layer on their surface. To access the unscreened surface potential of the graphene channel the residual layer was removed by contact AFM as described earlier in this chapter. The AFM topography map of an edge contact device ($w = 4$ μm and $l = 1.5$ μm) is shown in Figure 6.14a. In the middle of the image is the graphene channel with drain and source contacts at its sides. Wrinkle-like features of around 3 nm in height and 30 nm wide are present at the bottom part of the channel. This is caused by the formation of vertical multilayers during the transfer process as the sheet folds into itself while drying [197, 198]. In Figure 6.14b a 3D representation of the metal/graphene interface is shown. It can be seen that the fabrication by the edge contact approach renders a uniform contact with no sign of damage.

In Figure 6.15a the KPFM map (bottom) of the same device at $V_{ds} = 0$ V and the extracted profile (top) averaged over the whole width of the channel are shown. The metal/graphene interfaces present a sharp variation of the surface potential. Within the graphene channel itself the relative decrease of 100 mV in the work function surrounding the areas of the wrinkle features, agrees with reported values for multilayer graphene [194]. In Figure 6.15b and Figure 6.15c the KPFM map (bottom) and profile line (top) of the device at $V_{ds} = +1$ V and $V_{ds} =$ -1 V, respectively are shown. Here, a particular effect can be seen at the channel interfaces which does not follow the usual appearance as in top contact devices. In the top contact case, for positive bias voltage, the drain contact displays a variation of the Kelvin signal in relation to the voltage applied ($\Delta V_k \cong V_{ds}$). Then, over the length of the device this value gradually or suddenly decreases ($|\Delta V_k(x)| < |V_{ds}|$), continuing this way until the source contact. In the case of high contact resistances, the potential of the source contact is expected to have a lower value than the channel, i.e. the voltage drop at the contact.

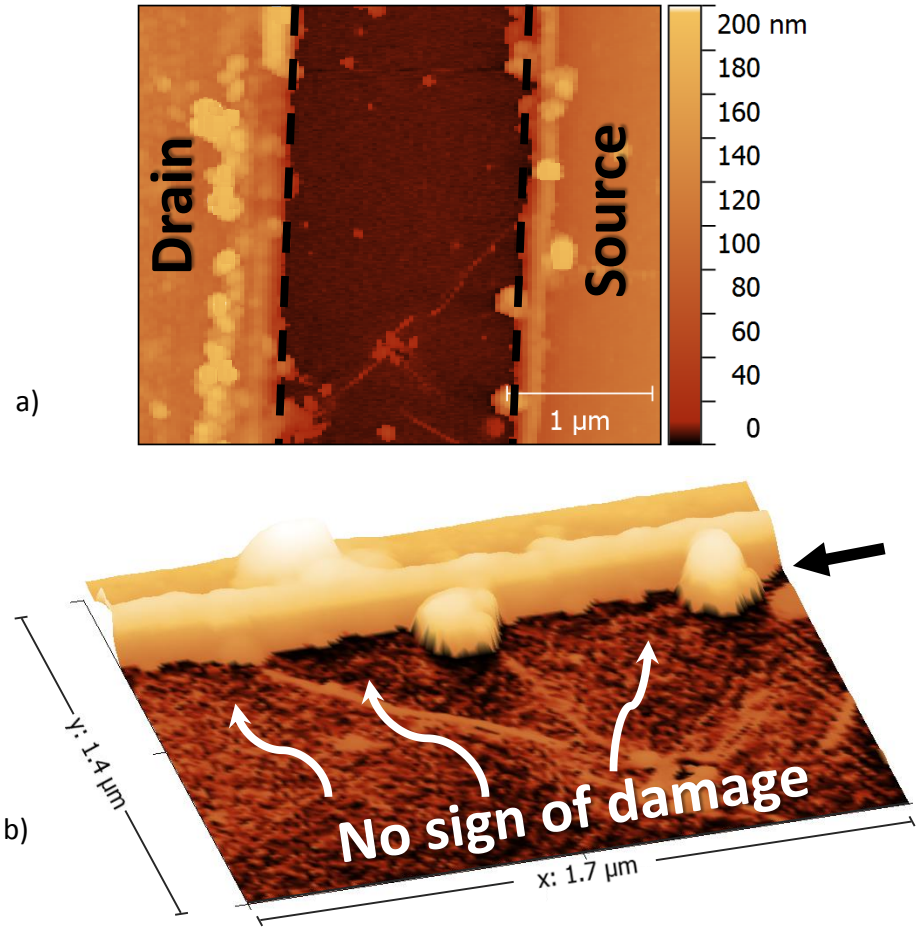

Figure 6.14: (a) AFM topography of an analyzed edge contact device and the (b) 3D topography map of the interface (along black arrow), which shows a uniform metal/graphene contact without damage.

However, in end contact devices graphene at the source interface has a surface potential lower than at the contact (compare with Figure 6.2), already indicating a possible reduction of the contact resistance.

The corroboration of a lower ρ_c, already suggested by TLM measurements, can be followed in Figure 6.16, where the voltage drop distribution map at V_{ds} = -1 V of the device presented above is shown. This map was created by carefully correlating every point measurement (pixel) from the V_{ds} = 0 V and the V_{ds} = -1 V KPFM map. Both contacts are indicated by the white dashed lines. In this plot the surface potential has a subtle change over the metal/graphene interface, i.e. no significant voltage drop, which can translate in a low ρ_c. The gradual drop over the length of the channel accounts for the integrity of the same, where it can be observed that the influence of the surface potential of the wrinkle features is marginal after the subtraction.

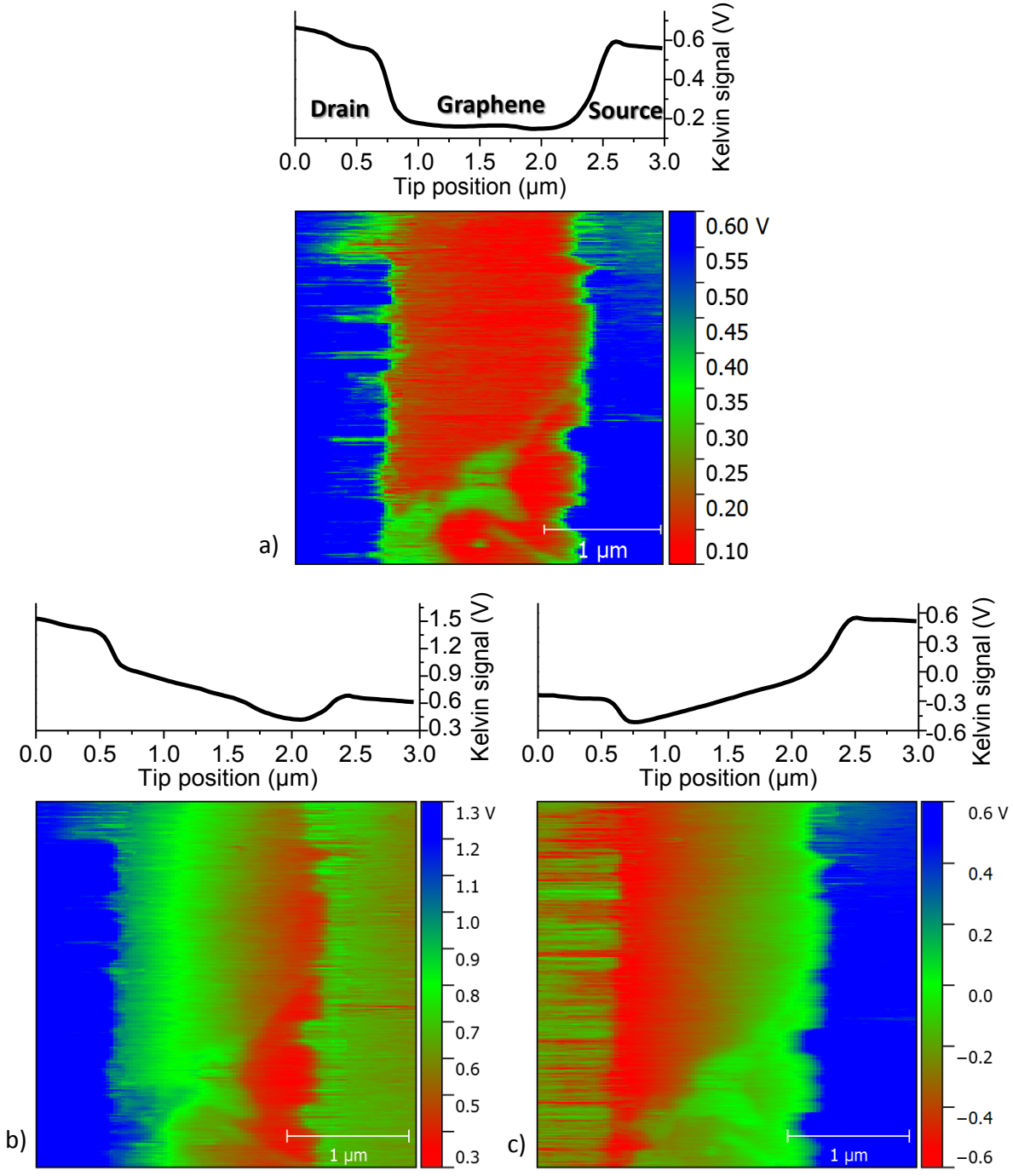

Figure 6.15: KPFM map and extracted profile (top) of the analyzed edge contact device at V_{ds} = (a) 0 V, (b) +1 V and (c) -1 V.

For the estimation of the ρ_c and ρ_s an average of 128 lines is extracted covering the whole channel's width. The KPFM voltage drops for different V_{ds} and topography profile are shown in Figure 6.17. As expected from Figure 6.16, the voltage drop at the

metal/graphene interface in Figure 6.17 is small and therefore complicate to evaluate.

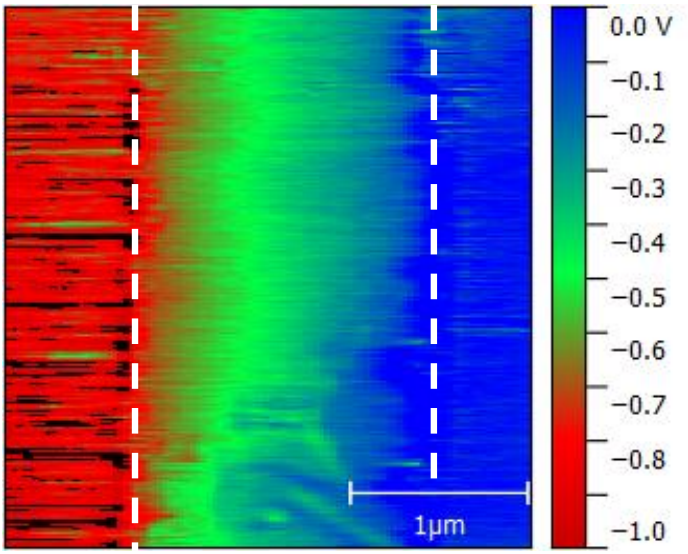

Figure 6.16: KPFM voltage drop distribution map of an end-contacted graphene device at V_{ds} = -1 V.

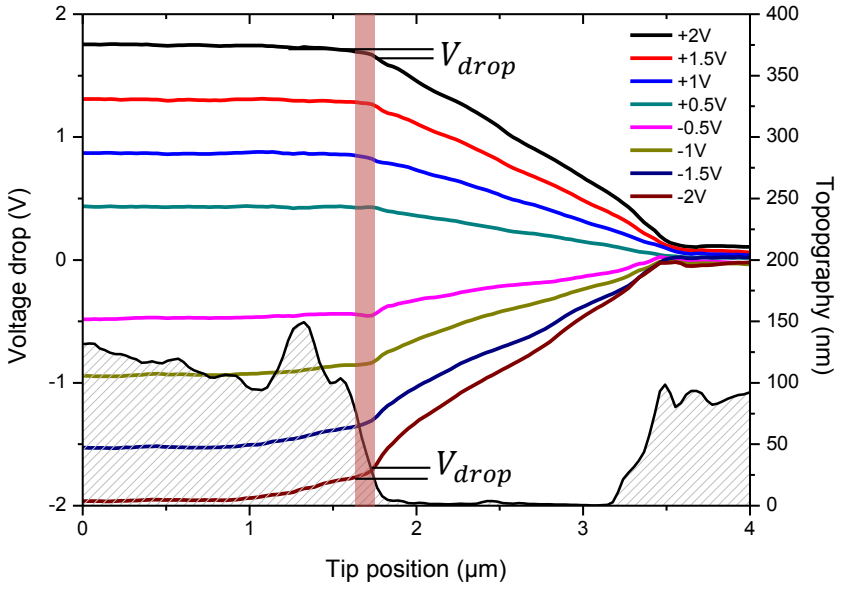

Figure 6.17: KPFM voltage drop profile along an edge contact device for different drain-source voltages. The shaded area represents the corresponding FWHM of the topography at the interface (see Figure 6.18).

To evaluate the small voltage drop of the edge contact devices a different approach for the calculation was used. Exemplified in Figure 6.18 is a non-averaged topography profile (black line), its derivative and the derivative's peak fit (red/blue lines) at the interface

are shown. The voltage drop is calculated using the width of the peak fit centered at its inflection point (red shade).

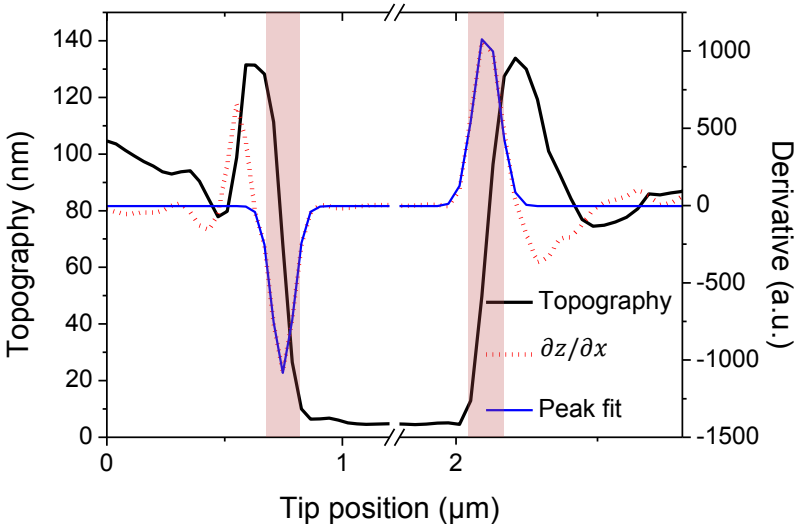

Figure 6.18: Plot of the topography profile (black line), its derivative (red dotted line) and derivative peaks fitting (blue line) of the drain and source contacts. The peak′s center and FWHM of the drain/graphene interface was used for calculation of the voltage drop.

Using this approximation and the corresponding experimental values of the current I_{ds} obtained during the KPFM measurements, the contact resistances for every V_{ds} applied can be estimated. No particular trend was found for the voltage polarity. Although the negative polarity has seemingly a larger drop in the profile line, close to the interface, this mostly happens at the metal. This can be explained as a measurement artifact caused by the subtraction method and the intrinsic decrease in the potential before the interface (seen in the $V_{ds} = 0$ V profile) and is therefore not taken into account for the ρ_c calculation. The resistances obtained for every voltage applied were averaged and resulted, as expected, in a reduced mean value of 250 $\Omega\mu$m, with a lowest value of 156 $\Omega\mu$m. The averaged channel′s ρ_s resulted in 870 $\Omega/\square$ which is comparable to results obtained before. This outcome denotes the effect of the edge contact architecture in ρ_c, with a reduction of at least one order of magnitude for graphene devices fabricated by optical lithography in comparison to the conventional fabrication process [16].

In Table 6.1 a summary of the different devices analyzed by KPFM voltage drop as described previously is shown. In this representative sample group, reduced values of averaged ρ_c can be observed for different devices with variable geometries. It can be noted

that devices with $w = 1.5$ μm did not present an improvement, which as discussed before, can be related to defects on the channel having a larger and more critical effect on the total resistance of these narrow devices.

Since the modified fabrication process is aimed at not having any graphene underneath the metal, it can be argued that these improvements come indeed from the narrowing of the interfaces, forcing an in-plane injection of carriers over the width of the channel. Even more, devices produced with this scheme have been also analyzed at AMO GmbH for transconductance measurements achieving a record value peak of $g_m = 0.51$ A/V for CVD graphene devices prepared by optical lithography. This again accounts for the improvement obtained by the modification of the customary approach.

Device	w (μm)	l (μm)	ρ_c ($\Omega\mu$m)	ρ_s ($\Omega/\square$)
C7	15	9.5	250	2500
C7	15	5.5	320	860
A4	4	1.5	250	870
A5	4	1.5	180	400
C5	4	3.5	370	3000
C6	4	3.5	200	700

Table 6.1: Summary of the analyzed devices by the KPFM voltage drop method. The values of ρ_c correspond to an average value for drain and source contacts.

6.7 Conclusions

In summary, the influence of fabrication and contact design issues in ρ_c of graphene-based devices were investigated. First, a comparison between devices produced by optical and e-beam lithography was made by KPFM voltage drop analysis. A systematic increase of ρ_c was found for optical lithography derived devices (4 – 30 k$\Omega\mu$m) compared to those derived by e-beam lithography (0.1 – 1 k$\Omega\mu$m). Consequently, the influence of standard optical lithography process was further studied. It was found that optical lithography leaves a 3 – 4 nm thick and 1 nm rough layer of optical resist residues behind which can be removed by AFM patterning. Raman spectroscopy before and after the patterning procedure showed no damage to the underlying graphene sheet suggesting that the residue layer is physically adsorbed to the surface of the graphene. It was found by KPFM analysis that this small residue layer has a screening effect of about 100 mV on the surface potential of graphene. This clarifies the contact resistance difference of optical lithography process devices, which can be about an order of magnitude larger, with respect to reference devices patterned with e-beam lithography. These findings make evident that in case of optical lithography, resist residues have to be taken into account.

This was followed up by the investigation of the contact design in optical lithography graphene-based devices. Graphene-based devices were prepared by a modified optical lithography approach to have the material deliberately removed from underneath the metal and make contact with graphene only over its width. These devices were analyzed by a combination of TLM and KPFM measurements. Even with this restriction in the physical connection between the two materials, this procedure yields working devices. TLM measurements suggested a reduction of the graphene/metal contact resistance which was verified in individual two-terminal devices by KPFM measurements. KPFM voltage drop analysis indeed showed a reduced voltage drop at the metal/graphene interfaces, confirming a positive influence of the contact architecture by reducing the contact resistivity down to values of 250 $\Omega\mu$m, thus confirming the reduction of contact resistance by one order of magnitude. These results showed an improvement of optical lithography graphene-based devices due to a change in the contact design accomplished by simple but effective modification of the fabrication process. With it the disadvantage of the residue layer left by optical lithography in graphene surface was overcome without the need of an extra cleaning step and with a reduction of the contact resistance down to values comparable to those from e-beam lithography.

Chapter 7

Summary

This work aimed to investigate the electrical behavior of operational graphene-based devices on ambient conditions at the nanoscale by means of KPFM. The analysis concentrated on the metal/graphene interfaces and device channel of two-terminal devices fabricated with graphene types derived from high production yield syntheses. First, efforts were placed in the improvement of KPFM by the detection of the electrostatic force gradient. Then, the effects of the C/O ratio and transport regime transitions were studied for FGS devices. On the last part of this work, the influence of the fabrication processes and contact design on CVD graphene-based devices were investigated. This chapter will summarize the conclusions and results obtained in this thesis.

The phase shifts of the mechanical oscillation of the AFM tip were successfully implemented for the detection of the electrostatic force gradient in single pass PM-KPFM on an already operating AM-KPFM system. The connections, signals and working parameters needed for its operation were presented. The improvement of this implementation was shown with the investigation of graphene grown on a Cu film. Here a feature of less than 20 nm and a Kelvin signal variation of 80 mV could be clearly resolved. These values are competitive to the results reported in the literature for the analysis of InAlAs/InGaAs layered heterostructures. The improvement of PM-KPFM over AM-KPFM on the acquisition of KPFM maps for the same modulation voltage was shown. For the voltage drop analysis comparison, the information extracted from the KPFM maps derived from the detection of the force and force gradient had a rate of change $\Delta V/\Delta x = 0.24$ V/μm and $\Delta V/\Delta x = 0.6$ V/μm, respectively, showing an

increased reaction to surface potential variations without an increase of the modulation voltage. The certainty of KPFM voltage drop analysis was supported by a comparison of results, in the same devices, to those from the conventional 4p macroscopic method.

Due to KPFM high spatial resolution, this non-invasive technique allows the electrical characterization of operating two-terminal micrometer devices with irregular geometries. This was successfully applied to the study of the C/O ratio effect on individual flakes of FGS and their electric contacts by means of KPFM voltage drop analysis. The use of KPFM allows separating the contributions of the channel and contacts, were a transition could be observed from non-ohmic high-resistance of $\rho_s > 400$ k$\Omega/\square$ and $\rho_c > 100$ k$\Omega\mu$m to ohmic low-resistance of $\rho_s < 10$ k$\Omega/\square$ and $\rho_c < 1$ k$\Omega\mu$m with increasing C/O ratio. It is concluded that the non-linear behavior at low C/O are due to a combination of sheet intrinsic hopping-dominated charge transport at the channel and Schottky characteristics at the FGS-metal contacts superimposed in an ohmic behavior onset and/or tunneling contributions, which happens before the sp^2 network recovery reaches the percolation limit. Agreeing with literature, at mildly reduced samples (C/O = 23), the linear IV behavior observed at both, channel and contacts, appears due to the charge transport percolating through the restored sp^2 network of graphene. These results are a valuable contribution to the overall knowledge of this material and make a precedent for understanding the behavior of FGS conductive networks and their electrical contacts in technological applications.

In the last part of this thesis, the impact that the fabrication process and contact design can have on the contact resistance of CVD grown graphene devices were investigated. Optical lithography showed a negative effect on the device′s ρ_c compared to those produced by e-beam lithography, with usual values larger than k$\Omega\mu$m for the former and lower than k$\Omega\mu$m for the latter. Using a combination of AFM patterning, KPFM and Raman mapping it was found that optical lithography leaves a 3 – 4 nm thick and 1 nm rough layer of optical resist residues behind which is physically adsorbed to the surface of the graphene. It is then argued that this thin residue layer leads to the observed increase in resistance. Due to the importance of optical lithography in industry, devices produced with a simple and efficient modification in the customary fabrication procedure were analyzed to overcome this problem. This modification had the objective of making a metal/graphene contact only over the edge of the channel instead of its

surface. The influence of this modified optical lithography process could have in the performance of the devices was studied by a combination of TLM and KPFM voltage drop analysis. KPFM voltage drop analysis confirmed that devices with ρ_c values of less than 200 $\Omega\mu$m can be achieved, thus confirming the reduction of contact resistance by one order of magnitude with a simple and effective modification of the customary approach for optical lithography devices. Overall, these results highlight the potential of edge contacts on graphene devices for a variety of applications.

In the outlook, KPFM can be applied to the study of the ever-growing family of 2D materials, but most importantly their heterostructures and devices. A great deal of interest could be on the relative changes of surface potential in their interfaces and/or the relative reactions to atmospheric conditions. Also, the capabilities for electrical characterization could be expanded by the use of a third lock-in amplifier and the second harmonic of the KPFM frequency which gives access to dielectric characteristics of the sample. Such approach has been marginally studied and reported, however, it could prove itself as a powerful characterization technique, along with KPFM, for the study of 2D devices.

Appendix A

Detailed procedure of the production of samples

A.1 FGS samples

This procedure was reported in [199] and performed by F. E. Muckel and S. Wolff for the publication [13].

The GO obtained by the Hummer′s method is washed to remove residues from the process such as acid excess. The material is then thoroughly dried as water content in GO has a negative effect in the exfoliation and reduction process [10].

For the thermal exfoliation/reduction a quartz tube is used. The tube is flushed with nitrogen and then brought to the desired temperature. For the $FGS_{7.3}$ samples temperatures of 500^oC for one minute were used. The FGS_{24} and FGS_{170} samples were treated at 1000^oC for one minute. The FGS_{170} samples were additionally placed for 1 hr at $> 100^oC$ temperatures in Ar atmosphere.

For the electrical characterization, the FGS samples are brought to a SiO_2/Si substrate to be individually contacted. This was done through a two-step e-beam lithography process. Both steps used the e-beam lithography system *eLine* from *Raith Inc.* In the first step the substrate is patterned with areas of 550 μm x 550 μm covered with $\sim$12 μm crosses (10 nm Ti/200 nm Au), separated by 50 μm (Figure A.1a). These crosses have underneath numbers which were placed on the SiO_2 substrate to help with the identification of the flakes and adjustment of the contacts position during the contacting process. The areas covered with crosses (e.g. A, B, C and D in Figure A.1b) are surrounded by 500 μm x 500 μm square bond pads, which will be used later for the

microbonding of the samples. After the placement of the adjustment crosses, the substrate is cleaned in an acetone bath. Afterwards the sample is rinsed with acetone, methanol and isopropanol and dried with nitrogen.

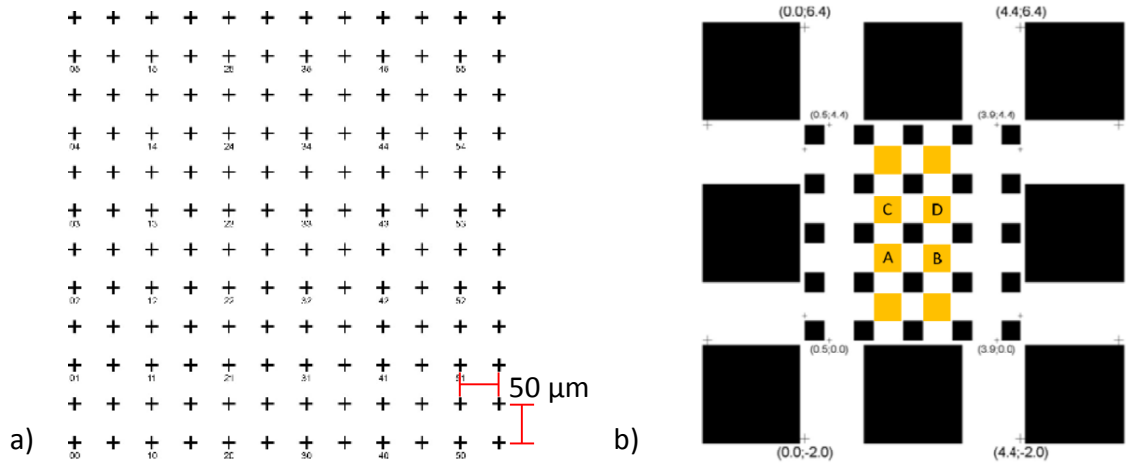

Figure A.1: (a) Diagram of one area containing micrometer Ti/Au adjustment crosses. (b) Overview diagram of several adjustment crosses areas and the surrounding bond pads for microbonding. Adapted from [199].

The produced FGS, in its powder form, is weighed and diluted in an ethanol dispersion (0.1 mg/ml to 0.02 mg/ml). To dissolve agglomerates the dispersion is treated with ultrasound (tip sonification) for 30 min, followed by centrifugation at 3000 rpm for 1 hr. An aliquot of 10 to 20 ml (depending on the concentration of the dispersion) is dropped onto the pre-patterned SiO_2/Si substrate. The ethanol is left to evaporate over time at room temperature.

The selection and measurement of the suitable flakes is done by a light microscope. The discrimination between SLG and MLG is done by contrast comparison. For the contacting of the flake by metal electrodes, coordinates are required by the *eLine* software. This is achieved by taking a picture of the selected flake and its surrounding adjustment crosses. Assisted by *Matlab* software a coordinate system is specified from this picture and thus the position of the contacts can be calculated in relation to the adjusting crosses. In Figure A.2a is the picture of a flake with the associated coordinates from *Matlab*. Four flakes of the same C/O ratio will be contacted.

The coordinates calculated by *Matlab* are introduced in the design of the *eLine* software. The metal contacts consist of two shapes: a trapezoid shape is used for the physical contact of the metal electrode and FGS, and the interconnection from the trapezoid contacts to the bond pads is done with a rectangle shape (Figure A.2b). To

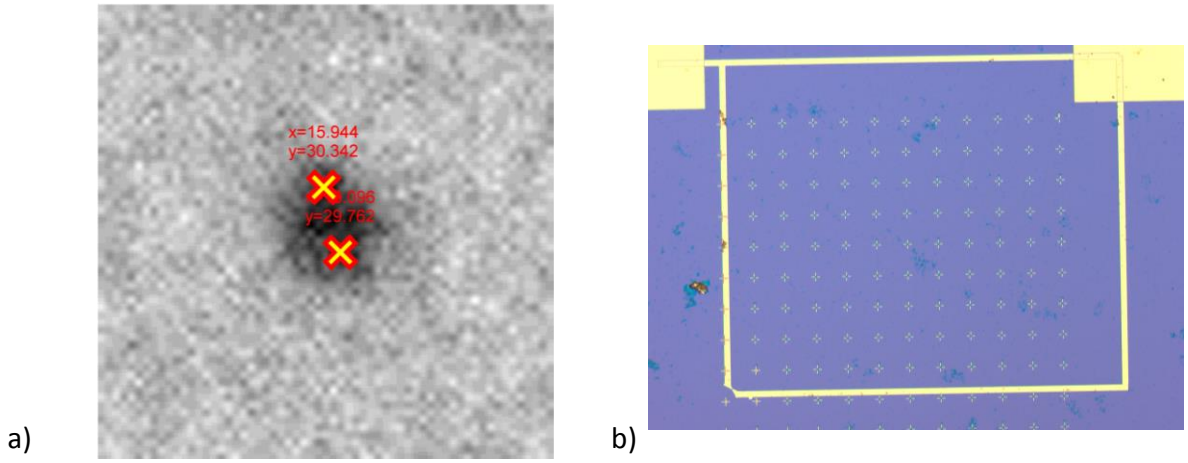

Figure A.2: (a) Optical image of a selected FGS flake and its coordinates taken by *Matlab*. (b) Optical image of a contacted FGS flake and its interconnection to the bond pads. Images taken from [199].

prevent damage from electrostatic discharge to the flake during storage and before (the first) operation, a short circuit is placed between the two bond pads.

For the e-beam lithography, few drops of a 3% PMMA resist were placed on the surface of the substrate and spin coated at 400 rpm during 40 s. The accelerating voltage used for the e-beam was 10 kV with an aperture of 30 μm. The PMMA resist was exposed to a dose of 250 μC/cm^2. After the illumination, the sample was placed in a 3 to 1 mixture of methyl isobutyl ketone and isopropanol for development and afterwards cleaned with isopropanol for a minute. In the next step 10 nm Ti (as an adhesion layer) and 100 nm Au were deposited by e-beam evaporation. For the lift-off, the sample was left on acetone overnight. The use of ultrasound bath during lift-off is not advised since the FGS flakes might release from the substrate. After lift-off, the samples were rinsed with acetone, methanol and isopropanol and dried with nitrogen.

A.2 CVD samples

The graphene devices samples were produced by colleagues at AMO GmbH.

For all samples, commercial graphene grown by CVD on 25 μm-thick Cu foil (Graphenea, S.A.) was transferred onto dielectric substrates (details in Appendix B) by PMMA-assisted wet transfer as presented in subsection 2.2.2.

1. Customary approach (Top contacts): After graphene is available on the desired substrate, the production of micrometer devices undergoes either an e-beam or optical lithography process for the definition of the metal contacts and graphene channel, this is exemplified in Figure A.3(a-l) and described next. The graphene sample (a) is spin coated with the corresponding positive lithography resist (b), PMMA for e-beam and AZ5214E for optical lithography. The resist was spin coated onto the sample with a thickness of ~ 1 μm and cured at 95^{o}C for 1.5 min. The definition of the metal contacts is done by exposing the resist to either an e-beam or UV light (365 nm) which will change its properties, exemplified in (c) as a change in color. The design and position of the contacts by e-beam are done through software which indicates where the e-beam should raster the sample. In optical lithography, this is done through a mask which aligns with the sample and only allows UV exposure to the areas already imprinted on the mask. After the resist is exposed the sample is developed, i.e. the exposed areas of resist are removed while the unexposed are unaffected (d). Afterwards, metal is evaporated on the sample (e) and after the removal of the resist (lift-off), the metal electrode is placed on top of graphene.

The production continues by defining the devices$'$ channels, i.e. the transferred graphene sheet must be patterned to remove all the graphene aside from the planned channel areas. The structure of the graphene channel in the device will be covered by a negative optical lithography resist (g) and then exposed to UV light (h). Exposed negative lithography resists are unaffected by the development while unexposed areas will be removed (i). The sample is then exposed to O_2 plasma (2 min). The carbon atoms of the unprotected areas of graphene will react with the plasma and will be removed from the substrate (j) while the resist (usually $>$ 300 nm) protects the graphene underneath. Afterwards, the resist is removed by acetone and the graphene channels are defined (l).

This method was used for the 4p probe samples in section 4.4 and for TLM samples in section 6.2. The 1 cm^2 reference sample in section 6.2 followed the procedure showed in Figure A.3(a-d), with the variation of exposing the whole 1 cm^2 sample to UV light

for 2.5 s, subsequently baked at 110^{o}C for 2 min and again exposed for 15 s to UV light. After development in AZ developer (*MicroChem corp.*) for 6 s, the optical resist was finally removed in boiling acetone and rinsed in isopropyl alcohol.

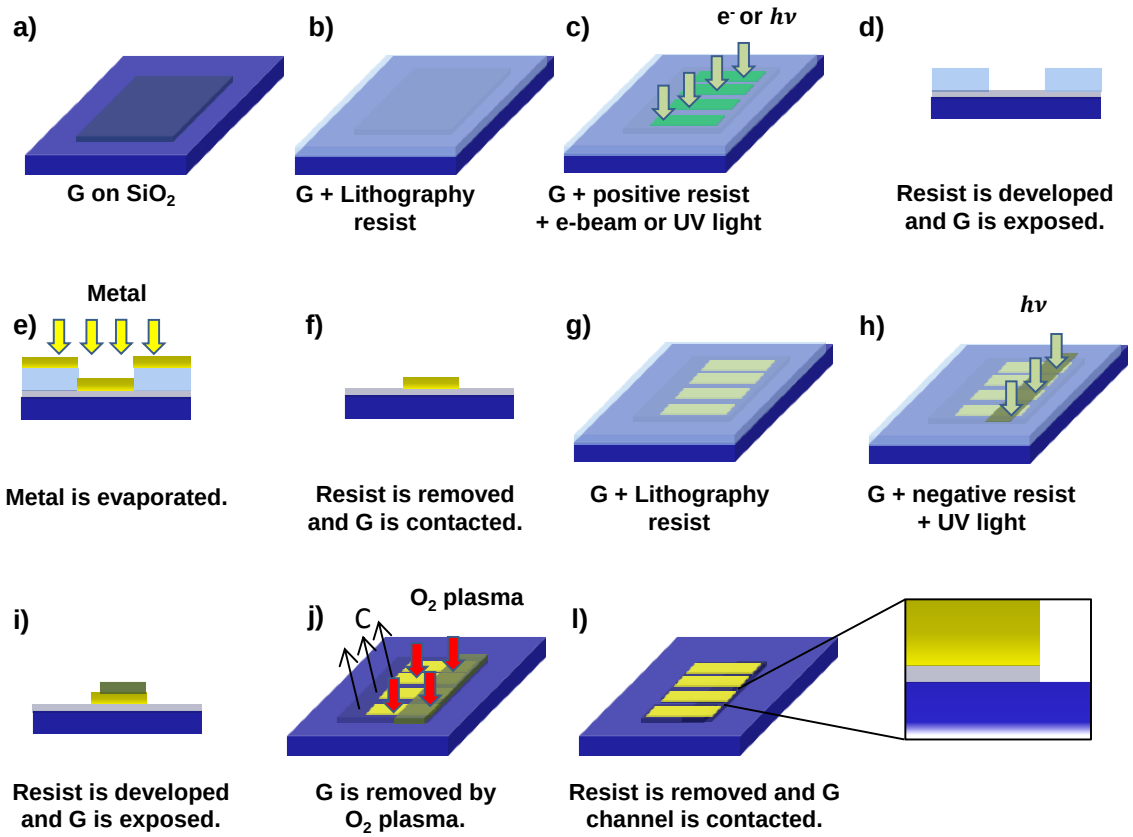

Figure A.3: Schematic flow chart of the customary approach to (a-f) place metal electrodes on graphene and (g-l) to define the graphene device channel. G stands for graphene.

2. Modification of the customary approach (Edge contacts): The variation to the optical lithography customary approach to produce edge contact to graphene is exemplified in process flow chart in Figure A.4(a-g). Commercial graphene grown by CVD on Cu foil was transferred onto a 90 nm SiO2/p-Si substrate (a). The entire steps of device fabrication were conducted with optical lithography and AZ5214E as resist (b). The sample was sample exposed to UV light (365 nm) for 2.5 s, subsequently baked at 110^{o}C for 2 min and again exposed for 15 s to UV light (c). The resist is then developed in AZ developer for 6 s (d) followed by exposure to oxygen plasma for 30 s (e). Metal contacts of Ni/Al (15/120 nm) were deposited using sputtering deposition (f) followed by lift-off technique (g). Both, the removal of graphene and placement of metal electrode

was performed with the same mask.

Using a different mask the rest of graphene was etched away with O_2 plasma for 2 min for the definition and patterning of the graphene channel. This process follows the procedure shown in Figure A.3(g-l). This method was used for the end contact samples in section 6.4.

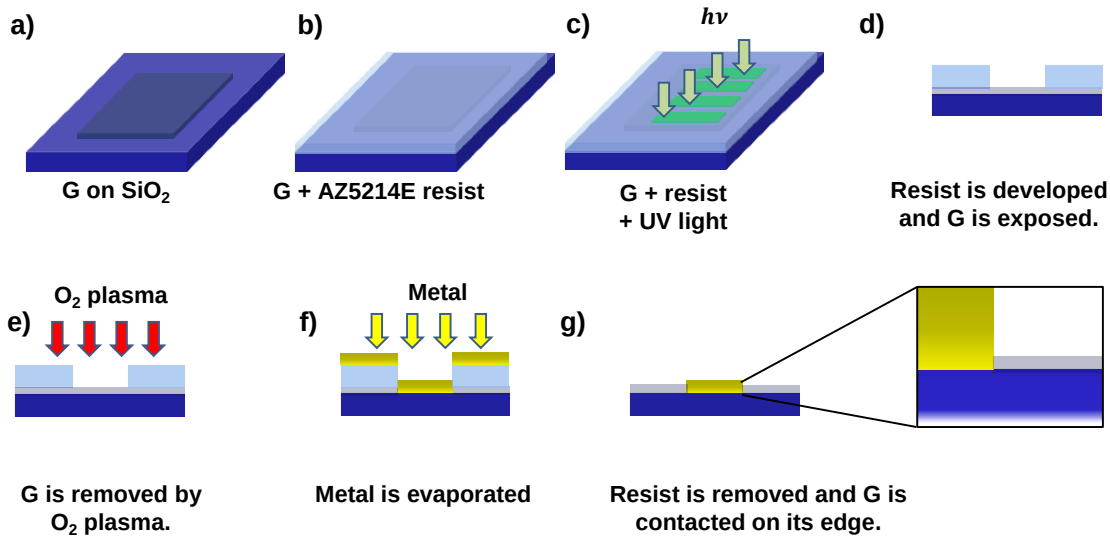

Figure A.4: (a-g) Schematic flow chart of the variation to the optical lithography customary approach to produce an edge contact to graphene.

Appendix B

Summarized information of the analyzed devices

Information of the analyzed devices on chapter 4, chapter 5 and chapter 6 are summarized next in table B.1, B.2 and B.3, respectively.

	4p probe
Dielectric	85 nm $Al_2O_3/SiO_2/Si$
Lithography for contacts	Optical
Lithography for channel	Optical
Metal contacts	Ni 20 nm
Channel's dimensions	$l = 8$ μm $w = 14$ μm

Table B.1: Description of the analyzed devices in chapter 4.

	$\mathbf{FGS_{7.3}}$	$\mathbf{FGS_{24}}$	$\mathbf{FGS_{170}}$
Dielectric	300 nm SiO_2/Si		
Lithography for contacts	e-beam		
Lithography for channel	n/a		
Metal contacts	Ti/Au 10/100 nm		
Channel's dimensions	$l = 0.8$ μm $w = 0.9$ μm	$l = 0.33$ μm $w = 0.74$ μm	$l = 0.4$ μm $w = 0.74$ μm

Table B.2: Description of the analyzed devices in chapter 5.

	4p probe	**TLM**	**Edge contact**
Dielectric	85 nm Al_2O_3/SiO_2/Si	90 nm SiO_2/Si	
Lithography for contacts	Optical	e-beam	optical
Lithography for channel		Optical	
Metal contacts	Ni 20 nm	Ni 20 nm	Ni/Al 15/120 nm
Channel's dimensions	$l = 8$ μm $w = 14$ μm	$l = 1.5$ μm $w = 8$ μm	$l = 1.5$ μm $w = 4$ μm

Table B.3: Description of the analyzed devices in chapter 6.

Bibliography

[1] K. S. Novoselov, A. K. Geim, S. V. Morozov, D. Jiang, Y. Zhang, S. V. Dubonos, I. V. Grigorieva, and A. A. Firsov. Electric field effect in atomically thin carbon films. *Science*, 306(5696):666–669, 2004.

[2] J. C. Meyer, A. K. Geim, M. I. Katsnelson, K. S. Novoselov, T. J. Booth, and S. Roth. The structure of suspended graphene sheets. *Nature*, 446:60–63, 2007.

[3] R. Peierls. Quelques proprietes typiques des corps solides. *Annales de l'institut Henri Poincare*, 5(3):177–222, 1935.

[4] L. D. Landau. Zur Theorie der Phasenumwandlungen II. *Phys. Z. Sowjetunion*, 11:26–35, 1937.

[5] K. S. Novoselov, A. K. Geim, S. V. Morozov, D. Jiang, M. I. Katsnelson, I. V. Grigorieva, S. V. Dubonos, and A. A. Firsov. Two-dimensional gas of massless dirac fermions in graphene. *Nature*, 438:197–200, 2005.

[6] J. Baringhaus, M. Ruan, F. Edler, A. Tejeda, M. Sicot, A. Taleb, A. Li, Z. Jiang, E.H. Conrad, C. Berger, C. Tegenkamp, and W. A. de Heer. Exceptional ballistic transport in epitaxial graphene nanoribbons. *Nature*, 506:349–354, 2014.

[7] S. Das Sarma, S. Adam, E. H. Hwang, and E. Rossi. Electronic transport in two-dimensional graphene. *Rev. Mod. Phys.*, 83:407–470, 2011.

[8] X. Huang, Z. Yin, S. Wu, X. Qi, Q. He, Q. Zhang, Q. Yan, F. Boey, and H. Zhang. Graphene-based materials: Synthesis, characterization, properties, and applications. *Small*, 7(14):1876–1902, 2011.

[9] J. Yoon, W. Park, G-Y. Bae, Y. Kim, H. S. Jang, Y. Hyun, S. K. Lim, Y. Kahng, W-K. Hong, and H. C. Ko. Highly flexible and transparent multilayer MoS_2 transistors with graphene electrodes. *Small*, 9(19):3295–3300, 2013.

[10] M. J. McAllister, J. Li, D. H. Adamson, H. C. Schniepp, A. A. Abdala, J. Liu, M. Herrera-Alonso, D. L. Milius, R. Car, R. K. Prud'homme, and I. A. Aksay. Single sheet functionalized graphene by oxidation and thermal expansion of graphite. *Chemistry of Materials*, 19(18):4396–4404, 2007.

[11] X. Li, W. Cai, J. An, S. Kim, J. Nah, D. Yang, R. Piner, A. Velamakanni, I. Jung, E. Tutuc, S. K. Banerjee, L. Colombo, and R. S. Rouff. Large-area synthesis of high-quality and uniform graphene films on copper foils. *Science*, 324:1312, 2009.

[12] S. Sadewasser and T. Glatzel. *Kelvin Probe Force Microscopy: Measuring and Compensating Electrostatic Forces*. Springer Series in Surface Sciences. Springer Berlin Heidelberg, 2011.

[13] C. Punckt, F. Muckel, S. Wolff, I.A. Aksay, C.A. Chavarin, G. Bacher, and W. Mertin. The effect of degree of reduction on the electrical properties of functionalized graphene sheets. *Applied Physics Letters*, 102(2):023114, 2013.

[14] C. Mattevi, G. Eda, S. Agnoli, S. Miller, K. A. Mkhoyan, O. Celik, D. Mastrogiovanni, G. Granozzi, E. Garfunkel, and M. Chhowalla. Evolution of electrical, chemical, and structural properties of transparent and conducting chemically derived graphene thin films. *Advanced Functional Materials*, 19(16):2577–2583, 2009.

[15] F. Schwierz. Graphene transistors: Status, prospects, and problems. *Proceedings of the IEEE*, 101(7):1567–1584, 2013.

[16] C.A. Chavarin, A. A. Sagade, D. Neumaier, G. Bacher, and W. Mertin. On the origin of contact resistances in graphene devices fabricated by optical lithography. *Applied Physics A*, 122(2):58, 2016.

[17] L. Wang, I. Meric, P. Y. Huang, Q. Gao, Y. Gao, H. Tran, T. Taniguchi, K. Watanabe, L. M. Campos, D. A. Muller, J. Guo, P. Kim, J. Hone, K. L. Shepard, and C. R. Dean. One-dimensional electrical contact to a two-dimensional material. *Science*, 342(6158):614–617, 2013.

[18] J. R. Pinzon, A. Villalta-Cerdas, and L. Echegoyen. *Fullerenes, Carbon Nanotubes, and Graphene for Molecular Electronics*, pages 127–174. Springer Berlin Heidelberg, Berlin, Heidelberg, 2012.

[19] A. H. Castro Neto, F. Guinea, N. M. R. Peres, K. S. Novoselov, and A. K. Geim. The electronic properties of graphene. *Rev. Mod. Phys.*, 81:109–162, 2009.

[20] A. K. Geim and K.S. Novoselov. The rise of graphene. *Nature Materials*, 6:183–191, 2007.

[21] L. Pauling. *The Nature of the Chemical Bond and the Structure of Molecules and Crystals: An Introduction to Modern Structural Chemistry*. George Fisher Baker Non-Resident Lecture Series. Cornell University Press, Ithaca, N.Y., 1960.

[22] A. Maffucci and G. Miano. Electrical properties of graphene for interconnect applications. *Applied Sciences*, 4(2):305, 2014.

[23] J. G. Champlain. A first principles theoretical examination of graphene-based field effect transistors. *Journal of Applied Physics*, 109(8):084515, 2011.

[24] J. Martin, N. Akerman, G. Ulbricht, T. Lohmann, J.H. Smet, K. von Klitzing, and A. Yacoby. Observation of electronhole puddles in graphene using a scanning single-electron transistor. *Nature Physics*, 4:144–148, 2008.

[25] J. H. Chen, C. Jang, S. Adam, M.S. Fuhrer, E.D. Williams, and M. Ishigami. Charged-impurity scattering in graphene. *Nature Physics*, 4:377–381, 2008.

[26] S. Cho and M. S. Fuhrer. Charge transport and inhomogeneity near the minimum conductivity point in graphene. *Phys. Rev. B*, 77:081402, 2008.

[27] J. G. Champlain. On the use of the term ambipolar. *Applied Physics Letters*, 99(12):123502, 2011.

[28] Y. Yu, Y. Zhao, S. Ryu, L. E. Brus, K. S. Kim, and P. Kim. Tuning the graphene work function by electric field effect. *Nano Letters*, 9(10):3430–3434, 2009.

[29] P. Avouris and C. Dimitrakopoulos. Graphene: synthesis and applications. *Materials Today*, 15(3):86 – 97, 2012.

[30] Y. Wu, D. B. Farmer, F. Xia, and P. Avouris. Graphene electronics: Materials, devices, and circuits. *Proceedings of the IEEE*, 101(7):1620–1637, 2013.

[31] R. Murali, Y. Yang, K. Brenner, T. Beck, and J. D. Meindl. Breakdown current density of graphene nanoribbons. *Applied Physics Letters*, 94(24):243114, 2009.

[32] K.I. Bolotin, K.J. Sikes, Z. Jiang, M. Klima, G. Fudenberg, J. Hone, P. Kim, and H.L. Stormer. Ultrahigh electron mobility in suspended graphene. *Solid State Communications*, 146(910):351 – 355, 2008.

[33] C. Sire, F. Ardiaca, S. Lepilliet, J. T. Seo, M. C. Hersam, G. Dambrine, H. Happy, and V. Derycke. Flexible gigahertz transistors derived from solution-based single-layer graphene. *Nano Letters*, 12(3):1184–1188, 2012.

[34] Y. M. Lin, K. Jenkins, D. Farmer, A. Valdes-Garcia, P. Avouris, C. Y. Sung, H. Y. Chiu, and B. Ek. Development of graphene FETs for high frequency electronics. In *2009 IEEE International Electron Devices Meeting*, pages 1–4, 2009.

[35] Y. Lin, A. Valdes-Garcia, S. Han, D. B. Farmer, I. Meric, Y. Sun, Y. Wu, C. Dimitrakopoulos, A. Grill, P. Avouris, and K. A. Jenkins. Wafer-scale graphene integrated circuit. *Science*, 332(6035):1294–1297, 2011.

[36] Y. Wu, K. A. Jenkins, A. Valdes-Garcia, D. B. Farmer, Y. Zhu, A. A. Bol, C. Dimitrakopoulos, W. Zhu, F. Xia, P. Avouris, and Y. Lin. State-of-the-art graphene high-frequency electronics. *Nano Letters*, 12(6):3062–3067, 2012.

[37] J. Zheng, L. Wang, R. Quhe, Q. Liu, H. Li, D. Yu, Z. Gao, and J. Lu. Sub-10 nm gate length graphene transistors: Operating at terahertz frequencies with current saturation. *Scientific Reports*, 3(1314):1–9, 2013.

[38] W. Mehr, J. Dabrowski, J. C. Scheytt, G. Lippert, Y. H. Xie, M. C. Lemme, M. Ostling, and G. Lupina. Vertical graphene base transistor. *IEEE Electron Device Letters*, 33(5):691–693, 2012.

[39] S. Bae, H. Kim, Y. Lee, X. Xu, J. Park, K.S. Kim, H.R. Kim, J. Ahn, B.H. Hong, and S. Lijima. Roll-to-roll production of 30-inch graphene films for transparent electrodes. *Nature Nanotechnology*, 5:574–578, 2010.

[40] P. Blake, P. D. Brimicombe, R. R. Nair, T. J. Booth, D. Jiang, F. Schedin, L. A. Ponomarenko, S. V. Morozov, H. F. Gleeson, E. W. Hill, A. K. Geim, and K. S. Novoselov. Graphene-based liquid crystal device. *Nano Letters*, 8(6):1704–1708, 2008.

[41] D. Schall, D. Neumaier, M. Mohsin, B. Chmielak, J. Bolten, C. Porschatis, A. Prinzen, C. Matheisen, W. Kuebart, B. Junginger, W. Templ, A. L. Giesecke,

and H. Kurz. 50 GBit/s photodetectors based on wafer-scale graphene for integrated silicon photonic communication systems. *ACS Photonics*, 1(9):781–784, 2014.

[42] D. Schall, M. Mohsin, A. A. Sagade, M. Otto, B. Chmielak, S. Suckow, A. L. Giesecke, D. Neumaier, and H. Kurz. Infrared transparent graphene heater for silicon photonic integrated circuits. *Opt. Express*, 24(8):7871–7878, 2016.

[43] F. Schwierz. Graphene transistors. *Nature Nanotechnology*, 5:487–496, 2010.

[44] A. K. Geim. Graphene: Status and prospects. *Science*, 324(5934):1530–1534, 2009.

[45] C. Casiraghi, S. Pisana, K. S. Novoselov, A. K. Geim, and A. C. Ferrari. Raman fingerprint of charged impurities in graphene. *Applied Physics Letters*, 91(23):233108, 2007.

[46] G. M. Rutter, S. Jung, N.N. Klimov, D.B. Newell, N.B. Zhitenev, and J.A. Stroscio. Microscopic polarization in bilayer graphene. *Nature Physics*, 7:649–655, 2011.

[47] J. Kedzierski, P. L. Hsu, A. Reina, J. Kong, P. Healey, P. Wyatt, and C. Keast. Graphene-on-insulator transistors made using C on Ni chemical-vapor deposition. *IEEE Electron Device Letters*, 30(7):745–747, 2009.

[48] K. Nakada, M. Fujita, G. Dresselhaus, and M. S. Dresselhaus. Edge state in graphene ribbons: Nanometer size effect and edge shape dependence. *Phys. Rev. B*, 54:17954–17961, 1996.

[49] Y. Zhang, L. Zhang, and C. Zhou. Review of chemical vapor deposition of graphene and related applications. *Accounts of Chemical Research*, 46(10):2329–2339, 2013.

[50] K.V. Emetsev, A. bostwick, K. Horn, J. Jobst, G. L. Kellog, L. Ley, J.L. McChesney, T. Ohta, S.A. Reshanov, J. Rohrl, H. Weber, and T. Seyller. Towards wafer-size graphene layers by atmospheric pressure graphitization of silicon carbide. *Nature Materials*, 8:203–207, 2009.

[51] C. Held, T. Seyller, and R. Bennewitz. Quantitative multichannel NC-AFM data analysis of graphene growth on SiC(0001). *Beilstein Journal of Nanotechnology*, 3:179–185, 2012.

[52] B. Jens, R. Ming, F. Edler, A. Tejeda, M. Sicot, C. Tegenkamp, and W.A. de Heer. Exceptional ballistic transport in epitaxial graphene nanoribbons. *Nature*, 506:349–354, 2014.

[53] M. Hiramatsu, M. Naito, H. Kondo, and M. Hori. Fabrication of graphene-based films using microwave-plasma-enhanced chemical vapor deposition. *Japanese Journal of Applied Physics*, 52:1–5, 2013.

[54] Z. Bo, Y. Yang, J. Chen, K. Yu, J. Yan, and K. Cen. Plasma-enhanced chemical vapor deposition synthesis of vertically oriented graphene nanosheets. *Nanoscale*, 5:5180–5204, 2013.

[55] H. C. Schniepp, J. Li, M. J. McAllister, H. Sai, M. Herrera-Alonso, D. H. Adamson, R. K. Prud'homme, R. Car, D. A. Saville, and I. A. Aksay. Functionalized single graphene sheets derived from splitting graphite oxide. *The Journal of Physical Chemistry B*, 110(17):8535–8539, 2006.

[56] Y. Zhu, S. Murali, M. D. Stoller, A. Velamakanni, R. D. Piner, and R. S. Ruoff. Microwave assisted exfoliation and reduction of graphite oxide for ultracapacitors. *Carbon*, 48(7):2118 – 2122, 2010.

[57] S. Park, J. An, J. R. Potts, A. Velamakanni, S. Murali, and R. S. Ruoff. Hydrazine-reduction of graphite- and graphene oxide. *Carbon*, 49(9):3019–3023, 2011.

[58] S. Park, J. An, R. D. Piner, I. Jung, D. Yang, A. Velamakanni, S. T. Nguyen, and R. S. Ruoff. Aqueous suspension and characterization of chemically modified graphene sheets. *Chemistry of Materials*, 20(21):6592–6594, 2008.

[59] M. G. Chung, D. H. Kim, H. M. Lee, T. Kim, J. H. Choi, D. K. Seo, J. Yoo, S. Hong, T. J. Kang, and Y. H. Kim. Highly sensitive NO_2 gas sensor based on ozone treated graphene. *Sensors and Actuators B: Chemical*, 166167:172 – 176, 2012.

[60] Y. Zhu, M. D. Stoller, W. Cai, A. Velamakanni, R. D. Piner, D. Chen, and R. S. Ruoff. Exfoliation of graphite oxide in propylene carbonate and thermal reduction of the resulting graphene oxide platelets. *ACS Nano*, 4(2):1227–1233, 2010.

[61] L. Huang, Y. Huang, J. Liang, X. Wan, and Y. Chen. Graphene-based conducting inks for direct inkjet printing of flexible conductive patterns and their applications in electric circuits and chemical sensors. *Nano Research*, 4(7):675–684, 2011.

[62] F. Torrisi, T. Hasan, W. Wu, Z. Sun, A. Lombardo, T. S. Kulmala, G. Hsieh, S. Jung, F. Bonaccorso, P. J. Paul, D. Chu, and A. C. Ferrari. Inkjet-printed graphene electronics. *ACS Nano*, 6(4):2992–3006, 2012.

[63] K. Erickson, R. Erni, Z. Lee, N. Alem, W. Gannett, and A. Zettl. Determination of the local chemical structure of graphene oxide and reduced graphene oxide. *Advanced Materials*, 22(40):4467–4472, 2010.

[64] J. W. S. Hummers and R. E. Offeman. Preparation of graphitic oxide. *Journal of the American Chemical Society*, 80(6):1339–1339, 1958.

[65] J. I. Paredes, S. Villar-Rodil, A. Martnez-Alonso, and J. M. D. Tascon. Graphene oxide dispersions in organic solvents. *Langmuir*, 24(19):10560–10564, 2008.

[66] G.I. Titelman, V. Gelman, S. Bron, R.L. Khalfin, Y. Cohen, and H. Bianco-Peled. Characteristics and microstructure of aqueous colloidal dispersions of graphite oxide. *Carbon*, 43(3):641 – 649, 2005.

[67] J.W.S. Hummers. Preparation of graphitic acid, 1957. US Patent 2,798,878.

[68] H. L. Poh, F. Sanek, A. Ambrosi, G. Zhao, Z. Sofer, and M. Pumera. Graphenes prepared by staudenmaier, hofmann and hummers methods with consequent thermal exfoliation exhibit very different electrochemical properties. *Nanoscale*, 4:3515–3522, 2012.

[69] W. Gao, L. B. Alemany, L. Ci, and P. M. Ajayan. New insights into the structure and reduction of graphite oxide. *Nature Chemistry*, 1:403–408, 2009.

[70] C. Gomez-Navarro, R. T. Weitz, A. M. Bittner, M. Scolari, A. Mews, M. Burghard, and K. Kern. Electronic transport properties of individual chemically reduced graphene oxide sheets. *Nano Letters*, 7(11):3499–3503, 2007.

[71] Y. Zhu, S. Murali, W. Cai, X. Li, J. W. Suk, J. R. Potts, and R. S. Ruoff. Graphene and graphene oxide: Synthesis, properties, and applications. *Advanced Materials*, 22(35):3906–3924, 2010.

[72] X. Huang, Z. Yin, S. Wu, X. Qi, Q. He, Q. Zhang, Q. Yan, F. Boey, and H. Zhang. Graphene-based materials: Synthesis, characterization, properties, and applications. *Small*, 7(14):1876–1902, 2011.

[73] S. Stankovich, D. A. Dikin, R. D. Piner, K. A. Kohlhaas, A. Kleinhammes, Y. Jia, Y. Wu, S. T. Nguyen, and R. S. Ruoff. Synthesis of graphene-based nanosheets via chemical reduction of exfoliated graphite oxide. *Carbon*, 45(7):1558–1565, 2007.

[74] C. Zhang, W. Lv, W. Zhang, X. Zheng, M. Wu, W. Wei, Y. Tao, Z. Li, and Q. Yang. Reduction of graphene oxide by hydrogen sulfide: A promising strategy for pollutant control and as an electrode for Li-S batteries. *Advanced Energy Materials*, 4(7):1–5, 2014.

[75] A. B. Bourlinos, D. Gournis, D. Petridis, T. Szabo, A. Szeri, and I. Dekany. Graphite oxide: Chemical reduction to graphite and surface modification with primary aliphatic amines and amino acids. *Langmuir*, 19(15):6050–6055, 2003.

[76] N. A. Kotov, I. Dekany, and J. H. Fendler. Ultrathin graphite oxidepolyelectrolyte composites prepared by self-assembly: Transition between conductive and non-conductive states. *Advanced Materials*, 8(8):637–641, 1996.

[77] G. W. Cushing, V. Johanek, J. K. Navin, and I. Harrison. Graphene growth on Pt(111) by ethylene chemical vapor deposition at surface temperatures near 1000 K. *The Journal of Physical Chemistry C*, 119(9):4759–4768, 2015.

[78] Z. Li, P. Wu, C. Wang, X. Fan, W. Zhang, X. Zhai, C. Zeng, Z. Li, J. Yang, and J. Hou. Low-temperature growth of graphene by chemical vapor deposition using solid and liquid carbon sources. *ACS Nano*, 5(4):3385–3390, 2011.

[79] G. Ruan, Z. Sun, Z. Peng, and J. M. Tour. Growth of graphene from food, insects, and waste. *ACS Nano*, 5(9):7601–7607, 2011.

[80] S. Kim, J. Kim, K. Kim, Y. Hwangbo, J. Yoon, E. Lee, J. Ryu, H. Lee, S. Cho, and S. Lee. Synthesis of CVD-graphene on rapidly heated copper foils. *Nanoscale*, 6:4728–4734, 2014.

[81] N. K. Memon, S. D. Tse, J. F. Al-Sharab, H. Yamaguchi, A. B. Goncalves, B. H. Kear, Y. Jaluria, E. Y. Andrei, and M. Chhowalla. Flame synthesis of graphene films in open environments. *Carbon*, 49(15):5064–5070, 2011.

[82] V. Miseikis, D. Convertino, N. Mishra, M. Gemmi, T. Mashoff, S. Heun, N. Haghighian, F. Bisio, M. Canepa, V. Piazza, and C. Coletti. Rapid CVD growth of millimetre-sized single crystal graphene using a cold-wall reactor. *2D Materials*, 2(1):014006, 2015.

[83] T. Terasawa and K. Saiki. Growth of graphene on Cu by plasma enhanced chemical vapor deposition. *Carbon*, 50(3):869–874, 2012.

[84] A. Siokou, F. Ravani, S. Karakalos, O. Frank, M. Kalbac, and C. Galiotis. Surface refinement and electronic properties of graphene layers grown on copper substrate: An XPS, UPS and EELS study. *Applied Surface Science*, 257(23):9785–9790, 2011.

[85] H. I. Rasool, E. B. Song, M. Mecklenburg, B. C. Regan, K. L. Wang, B. H. Weiller, and J. K. Gimzewski. Atomic-scale characterization of graphene grown on copper (100) single crystals. *Journal of the American Chemical Society*, 133(32):12536–12543, 2011.

[86] J. Lee, L. Tao, Y. Hao, R. S. Ruoff, and D. Akinwande. Embedded-gate graphene transistors for high-mobility detachable flexible nanoelectronics. *Applied Physics Letters*, 100(15):152104, 2012.

[87] L. Zhao, K.T. Rim, H. Zhou, R. He, T.F. Heinz, A. Pinczuk, G.W. Flynn, and A.N. Pasupathy. Influence of copper crystal surface on the CVD growth of large area monolayer graphene. *Solid State Communications*, 151(7):509–513, 2011.

[88] J. Tian, B. Hu, Z. Wei, Y. Jin, Z. Luo, M. Xia, Q. Pan, and Y. Liu. Surface structure deduced differences of copper foil and film for graphene CVD growth. *Applied Surface Science*, 300:73 – 79, 2014.

[89] Y. Chen, X. Gong, and J. Gai. Progress and challenges in transfer of large-area graphene films. *Advanced Science*, 3(8):1500343, 2016.

[90] J. W. Suk, A. Kitt, C. W. Magnuson, Y. Hao, S. Ahmed, J. An, A. K. Swan, B. B. Goldberg, and R. S. Ruoff. Transfer of CVD-grown monolayer graphene onto arbitrary substrates. *ACS Nano*, 5(9):6916–6924, 2011.

[91] A. Reina, H. Son, L. Jiao, B. Fan, M. S. Dresselhaus, Z. Liu, and J. Kong. Transferring and identification of single- and few-layer graphene on arbitrary substrates. *The Journal of Physical Chemistry C*, 112(46):17741–17744, 2008.

[92] C.R. Dean, A.F. Young, I. Meric, L. Wang, S. Sorgenfrei, K. Watanabe, T. Taniguchi, P. Kim, K.L. Shepard, and J. Hone. Boron nitride substrates for high-quality graphene electronics. *Nature Nanotechnology*, 5:722–726, 2010.

[93] C. J. An, S. J. Kim, H. O. Choi, D. W. Kim, S. W. Jang, M. L. Jin, J. Park, J. K. Choi, and H. Jung. Ultraclean transfer of CVD-grown graphene and its application to flexible organic photovoltaic cells. *J. Mater. Chem. A*, 2:20474–20480, 2014.

[94] X. Li, Y. Zhu, W. Cai, M. Borysiak, B. Han, D. Chen, R. D. Piner, L. Colombo, and R. S. Ruoff. Transfer of large-area graphene films for high-performance transparent conductive electrodes. *Nano Letters*, 9(12):4359–4363, 2009.

[95] Y. Han, L. Zhang, X. Zhang, K. Ruan, L. Cui, Y. Wang, L. Liao, Z. Wang, and J. Jie. Clean surface transfer of graphene films via an effective sandwich method for organic light-emitting diode applications. *J. Mater. Chem. C*, 2:201–207, 2014.

[96] X. Yang, H. Peng, Q. X., Y. Zhou, and Z. Liu. Clean and efficient transfer of cvd-grown graphene by electrochemical etching of metal substrate. *Journal of Electroanalytical Chemistry*, 688:243 – 248, 2013.

[97] ASTM International. Test method for measuring resistivity of silicon wafers with an in-line four-point probe. *SEMI International Standards*, Silicon Materials and Process Control, 2005.

[98] W. Shockley. Research and investigation of inverse epitaxial UHF power transistors. *Air Force Atomic Laboratory*, 1964.

[99] G. K. Reeves and H. B. Harrison. Obtaining the specific contact resistance from transmission line model measurements. *IEEE Electron Device Letters*, 3(5):111–113, 1982.

[100] G. Binnig, H. Rohrer, Ch. Gerber, and E. Weibel. Surface studies by scanning tunneling microscopy. *Phys. Rev. Lett.*, 49:57–61, 1982.

[101] G. Binnig, H. Rohrer, Ch. Gerber, and E. Weibel. 7 x 7 reconstruction on si(111) resolved in real space. *Phys. Rev. Lett.*, 50:120–123, 1983.

[102] C. Bai. *Scanning Tunneling Microscopy and Its Application*. Physics and astronomy online library. Springer, 2000.

[103] E. Meyer, H.J. Hug, and R. Bennewitz. *Scanning Probe Microscopy: The Lab on a Tip*. Advanced Texts in Physics. Springer Berlin Heidelberg, 2013.

[104] L. Gross, F. Mohn, N. Moll, B. Schuler, A. Criado, E. Guitián, D. Peña, A. Gourdon, and G. Meyer. Bond-order discrimination by atomic force microscopy. *Science*, 337(6100):1326–1329, 2012.

[105] W.R. Bowen and N. Hilal. *Atomic Force Microscopy in Process Engineering: An Introduction to AFM for Improved Processes and Products*. Butterworth-Heinemann/IChemE series. Elsevier Science, Oxford, 2009.

[106] A.M. Baró and R.G. Reifenberger. *Atomic Force Microscopy in Liquid: Biological Applications*. Wiley, Weinheim, 2012.

[107] P. Klapetek. *Quantitative Data Processing in Scanning Probe Microscopy: SPM Applications for Nanometrology*. Micro and Nano Technologies. Elsevier Science, Oxford, 2012.

[108] J.N. Israelachvili. *Intermolecular and Surface Forces*. Intermolecular and Surface Forces. Elsevier Science, Oxford, 2010.

[109] G.J. Vancso and H. Schönherr. *Scanning Force Microscopy of Polymers*. Springer Laboratory. Springer Berlin Heidelberg, 2010.

[110] D. Sarid. *Scanning Force Microscopy: With Applications to Electric, Magnetic, and Atomic Forces*. Oxford Series in Optical and Imaging Sciences. Oxford University Press, 1994.

[111] P. Eaton and P. West. *Atomic Force Microscopy*. OUP Oxford, 2010.

[112] O. Custance, R. Perez, and S. Morita. Atomic force microscopy as a tool for atom manipulation. *Nature Nanotechnology*, 4:803–810, 2009.

[113] R. Garcia and R. Perez. Dynamic atomic force microscopy methods. *Surface Science Reports*, 47(68):197–301, 2002.

[114] S. Santos, V. Barcons, J. Font, and N. H. Thomson. Cantilever dynamics in amplitude modulation AFM: continuous and discontinuous transitions. *Journal of Physics D: Applied Physics*, 43(27):275401, 2010.

[115] A. D. McNaught, A. Wilkinson, International Union of Pure, and Applied Chemistry. *Compendium of Chemical Terminology: IUPAC Recommendations*, page 1175. IUPAC Chemical Data Series. Blackwell Science, 1997.

[116] T. R. Albrecht, P. Grutter, D. Horne, and D. Rugar. Frequency modulation detection using highQ cantilevers for enhanced force microscope sensitivity. *Journal of Applied Physics*, 69(2):668–673, 1991.

[117] H. O. Jacobs, P. Leuchtmann, O. J. Homan, and A. Stemmer. Resolution and contrast in Kelvin Probe Force Microscopy. *Journal of Applied Physics*, 84(3):1168–1173, 1998.

[118] Lord Kelvin. Contact electricity of metals. *Philosophical Magazine Series 5*, 46(278):82–120, 1898.

[119] M. Rohwerder and F. Turcu. High-resolution kelvin probe microscopy in corrosion science: Scanning Kelvin Probe Force Microscopy (SKPFM) versus classical Scanning Kelvin Probe (SKP). *Electrochimica Acta*, 53(2):290–299, 2007.

[120] S. Datta. Electrical resistance: an atomistic view. *Nanotechnology*, 15(7):S433, 2004.

[121] H. Diesinger, D. Deresmes, J. P. Nys, and T. Mlin. Kelvin force microscopy at the second cantilever resonance: An out-of-vacuum crosstalk compensation setup. *Ultramicroscopy*, 108(8):773–781, 2008.

[122] T. Wagner, H. Beyer, P. Reissner, P. Mensch, H. Riel, B. Gotsmann, and A. Stemmer. Kelvin probe force microscopy for local characterisation of active nanoelectronic devices. *Beilstein Journal of Nanotechnology*, 6:2193–2206, 2015.

[123] Kl. D. Katzer, W. Mertin, G. Bacher, A. Jaeger, and K. Streubel. Voltage drop in an $(Al_xGa_1x)0.5In0.5P$ light-emitting diode probed by Kelvin Probe Force Microscopy. *Applied Physics Letters*, 89(10):103522, 2006.

[124] A. Lochthofen, W. Mertin, G. Bacher, M. Furitsch, G. Brderl, U. Strauss, and V. Hrle. Microscopic investigation of InGaN/GaN heterostructure laser diode degradation using kelvin probe force microscopy. *Journal of Physics D: Applied Physics*, 41(13):135115, 2008.

[125] A. V. Ankudinov, V. P. Evtikhiev, E. Yu. Kotelnikov, A. N. Titkov, and R. Laiho. Voltage distributions and nonoptical catastrophic mirror degradation in high power InGaAs/AlGaAs/GaAs lasers studied by Kelvin Probe Force Microscopy. *Journal of Applied Physics*, 93(1):432–437, 2003.

[126] C. C. Tsai, P. L. Chiang, C. J. Sun, T. W. Lin, M. H. Tsai, Y. C. Chang, and Y. T. Chen. Surface potential variations on a silicon nanowire transistor in biomolecular modification and detection. *Nanotechnology*, 22(13):135503, 2011.

[127] V. Palermo, M. Palma, and P. Samor. Electronic characterization of organic thin films by Kelvin Probe Force Microscopy. *Advanced Materials*, 18(2):145–164, 2006.

[128] C. Jiang, M. Yang, Y. Zhou, B. To, J. Berry, N. Padture, K. Zhu, and M. Al-Jassim. Carrier separation and transport in perovskite solar cells studied by nanometre-scale profiling of electrical potential. *Nature Communications*, 6(8397):1–10, 2015.

[129] K. D. Katzer. Rasterkraftmikroskopie zur elektrischen Charakterisierung von innovativen Bauelementen und Nanostrukturen. *PhD Thesis, University of Duisburg-Essen, Faculty of Engineering*, 2008.

[130] I. R. Lewis and H. Edwards. *Handbook of Raman Spectroscopy: From the Research Laboratory to the Process Line.* Practical Spectroscopy. CRC Press, N.Y., 2001.

[131] J. R. Ferraro. *Introductory Raman Spectroscopy.* Elsevier Science, Oxford, 2003.

[132] P. Matousek and M. Morris. *Emerging Raman Applications and Techniques in Biomedical and Pharmaceutical Fields.* Biological and Medical Physics, Biomedical Engineering. Springer Berlin Heidelberg, 2010.

[133] R. Saito, M. Hofmann, G. Dresselhaus, A. Jorio, and M. S. Dresselhaus. Raman spectroscopy of graphene and carbon nanotubes. *Advances in Physics*, 60(3):413–550, 2011.

[134] A. Jorio, M.S. Dresselhaus, R. Saito, and G. Dresselhaus. *Raman Spectroscopy in Graphene Related Systems.* Wiley, Weinheim, 2011.

[135] M. S. Dresselhaus. *Graphite fibers and filaments.* Springer series in materials science. Springer-Verlag, Berlin, 1988.

[136] M. S. Dresselhaus, G. Dresselhaus, R. Saito, and A. Jorio. Raman spectroscopy of carbon nanotubes. *Physics Reports*, 409(2):47–99, 2005.

[137] A. C. Ferrari and D. M. Basko. Raman spectroscopy as a versatile tool for studying the properties of graphene. *Nature Nanotechnology*, 8:235–246, 2013.

[138] L. M. Malard, M.A. Pimenta, G. Dresselhaus, and M.S. Dresselhaus. Raman spectroscopy in graphene. *Physics Reports*, 473(56):51–87, 2009.

[139] S. N. Magonov, V. Elings, and M. H. Whangbo. Phase imaging and stiffness in tapping-mode atomic force microscopy. *Surface Science*, 375(2):L385–L391, 1997.

[140] G. Bar, R. Brandsch, M. Bruch, L. Delineau, and M. H. Whangbo. Examination of the relationship between phase shift and energy dissipation in tapping mode atomic force microscopy by frequency-sweep and force-probe measurements. *Surface Science*, 444(13):L11–L16, 2000.

[141] T. Melin, M. Zdrojek, and D. Brunel. *Electrostatic Force Microscopy and Kelvin Force Microscopy as a Probe of the Electrostatic and Electronic Properties of Carbon Nanotubes*. Springer Berlin Heidelberg, Berlin, Heidelberg, 2010.

[142] J. Luebbe, M. Temmen, H. Schnieder, and M. Reichling. Measurement and modelling of non-contact Atomic Force Microscope cantilever properties from ultra-high vacuum to normal pressure conditions. *Measurement Science and Technology*, 22(5):055501, 2011.

[143] M. L. Meade. *Lock-in Amplifiers: Principles and Applications*, page 81. IEEE electrical measurement series. P. Peregrinus, 1983.

[144] S. Sadewasser, Th. Glatzel, R. Shikler, Y. Rosenwaks, and M.Ch. Lux-Steiner. Resolution of Kelvin Probe Force Microscopy in ultrahigh vacuum: comparison of experiment and simulation. *Applied Surface Science*, 210(12):32 – 36, 2003.

[145] S. Sadewasser, C. Leendertz, F. Streicher, and M. Ch. Lux-Steiner. The influence of surface topography on Kelvin Probe Force Microscopy. *Nanotechnology*, 20(50):505503, 2009.

[146] H. Sugimura, Y. Ishida, K. Hayashi, O. Takai, and N. Nakagiri. Potential shielding by the surface water layer in Kelvin Probe Force Microscopy. *Applied Physics Letters*, 80(8):1459–1461, 2002.

[147] L. Yan, C. Punckt, I. A. Aksay, W. Mertin, and G. Bacher. Local voltage drop in a single functionalized graphene sheet characterized by Kelvin Probe Force Microscopy. *Nano Letters*, 11(9):3543–3549, 2011.

[148] D. R. Lide. *CRC Handbook of Chemistry and Physics, 85th Edition*. Number v. 85 in CRC Handbook of Chemistry and Physics, 85th Ed. Taylor & Francis, 2004.

[149] L. Zhao, K.T. Rim, H. Zhou, R. He, T.F. Heinz, A. Pinczuk, G.W. Flynn, and A.N. Pasupathy. Influence of copper crystal surface on the CVD growth of large area monolayer graphene. *Solid State Communications*, 151(7):509–513, 2011.

[150] T. Xie, K. Kumada, S. Kishimoto, and T. Mizutani. Measurement of cross-sectional potential of InAlAs/InGaAs layered structures in vacuum by Kelvin Probe Force Microscopy. *Japanese Journal of Applied Physics*, 42(4R):1751, 2003.

[151] Ch. Sommerhalter, Th. Glatzel, Th.W. Matthes, A. Jaeger-Waldau, and M.Ch. Lux-Steiner. Kelvin probe force microscopy in ultra high vacuum using amplitude modulation detection of the electrostatic forces. *Applied Surface Science*, 157(4):263–268, 2000.

[152] H. C. Schniepp, K. N. Kudin, J. Li, R. K. Prudhomme, R. Car, D. A. Saville, and I. A. Aksay. Bending properties of single functionalized graphene sheets probed by atomic force microscopy. *ACS Nano*, 2(12):2577–2584, 2008.

[153] K. L. Grosse, M. Bae, F. Lian, E. Pop, and W. P. King. Nanoscale joule heating, peltier cooling and current crowding at graphene-metal contacts. *Nature Nanotechnology*, 6:287–290, 2011.

[154] F. Xia, V. Perebeinos, Y. Lin, Y. Wu, and P. Avouris. The origins and limits of metalgraphene junction resistance. *Nature Nanotechnology*, 6:179–184, 2011.

[155] H. Xu, S. Wang, Z. Zhang, Z. Wang, H. Xu, and L. Peng. Contact length scaling in graphene field-effect transistors. *Applied Physics Letters*, 100(10):103501, 2012.

[156] S. P. Chen, H. L. Chiu, P. H. Wang, and Y. C. Liao. Inkjet printed conductive tracks for printed electronics. *ECS Journal of Solid State Science and Technology*, 4(4):P3026–P3033, 2015.

[157] K. Shin, J. Hong, and J. Jang. Micropatterning of graphene sheets by inkjet printing and its wideband dipole-antenna application. *Advanced Materials*, 23(18):2113–2118, 2011.

[158] M. Mishra, R. K. Joshi, S. Ojha, D. Kanjilal, and T. Mohanty. Role of oxygen in the work function modification at various stages of chemically synthesized graphene. *The Journal of Physical Chemistry C*, 117(38):19746–19750, 2013.

[159] X. Peng, F. Tang, and A. Copple. Engineering the work function of armchair graphene nanoribbons using strain and functional species: a first principles study. *Journal of Physics: Condensed Matter*, 24(7):075501, 2012.

[160] I. Jung, D. Dikin, S. Park, W. Cai, S. L. Mielke, and R. S. Ruoff. Effect of water vapor on electrical properties of individual reduced graphene oxide sheets. *The Journal of Physical Chemistry C*, 112(51):20264–20268, 2008.

[161] X. Wu, M. Sprinkle, X. Li, F. Ming, C. Berger, and W. A. de Heer. Epitaxial-graphene/graphene-oxide junction: An essential step towards epitaxial graphene electronics. *Phys. Rev. Lett.*, 101:026801, 2008.

[162] H. Y. Jeong, J. Y. Kim, J. W. Kim, J. O. Hwang, J. Kim, J. Y. Lee, T. H. Yoon, B. J. Cho, S. O. Kim, R. S. Ruoff, and S. Choi. Graphene oxide thin films for flexible nonvolatile memory applications. *Nano Letters*, 10(11):4381–4386, 2010.

[163] S. H. M. Jafri, K. Carva, E. Widenkvist, T. Blom, B. Sanyal, J. Fransson, O. Eriksson, U. Jansson, H. Grennberg, O. Karis, R. A. Quinlan, B. C. Holloway, and K. Leifer. Conductivity engineering of graphene by defect formation. *Journal of Physics D: Applied Physics*, 43(4):045404, 2010.

[164] M. R. Islam, D. Joung, and S. I. Khondaker. Schottky diode via dielectrophoretic assembly of reduced graphene oxide sheets between dissimilar metal contacts. *New Journal of Physics*, 13(3):035021, 2011.

[165] D. Joung, A. Chunder, L. Zhai, and S. I. Khondaker. Space charge limited conduction with exponential trap distribution in reduced graphene oxide sheets. *Applied Physics Letters*, 97(9):093105, 2010.

[166] S. Wang, R. Wang, X. Wang, D. Zhang, and X. Qiu. Nanoscale charge distribution and energy band modification in defect-patterned graphene. *Nanoscale*, 4:2651–2657, 2012.

[167] I. Jung, D. A. Dikin, R. D. Piner, and R. S. Ruoff. Tunable electrical conductivity of individual graphene oxide sheets reduced at low temperatures. *Nano Letters*, 8(12):4283–4287, 2008.

[168] E. Koren, N. Berkovitch, O. Azriel, A. Boag, Y. Rosenwaks, E. R. Hemesath, and L. J. Lauhon. Direct measurement of nanowire schottky junction depletion region. *Applied Physics Letters*, 99(22):223511, 2011.

[169] D. C. Marcano, D. V. Kosynkin, J. M. Berlin, A. Sinitskii, Z. Sun, A. Slesarev, L. B. Alemany, W. Lu, and J. M. Tour. Improved synthesis of graphene oxide. *ACS Nano*, 4(8):4806–4814, 2010.

[170] D. Yang, A. Velamakanni, G. Bozoklu, S. Park, M. Stoller, R. D. Piner, S. Stankovich, I. Jung, D. A. Field, C. A. Ventrice Jr., and R. S. Ruoff. Chemical analysis of graphene oxide films after heat and chemical treatments by X-ray photoelectron and micro-Raman spectroscopy. *Carbon*, 47(1):145–152, 2009.

[171] J. Campos-Delgado, Y. A. Kim, T. Hayashi, A. Morelos-Gmez, M. Hofmann, H. Muramatsu, M. Endo, H. Terrones, R. D. Shull, M. S. Dresselhaus, and M. Terrones. Thermal stability studies of CVD-grown graphene nanoribbons: Defect annealing and loop formation. *Chemical Physics Letters*, 469(13):177–182, 2009.

[172] J. Li, K. N. Kudin, M. J. McAllister, R. K. Prud'homme, I. A. Aksay, and R. Car. Oxygen-driven unzipping of graphitic materials. *Phys. Rev. Lett.*, 96:176101, 2006.

[173] R. Larciprete, S. Fabris, T. Sun, P. Lacovig, A. Baraldi, and S. Lizzit. Dual path mechanism in the thermal reduction of graphene oxide. *Journal of the American Chemical Society*, 133(43):17315–17321, 2011.

[174] F. Schwierz. Electronics: Industry-compatible graphene transistors. *Nature*, 472:41–42, 2011.

[175] G. Giovannetti, P. A. Khomyakov, G. Brocks, V. M. Karpan, J. van den Brink, and P. J. Kelly. Doping graphene with metal contacts. *Phys. Rev. Lett.*, 101:026803, 2008.

[176] S. M. Song, J. H. Bong, and B. J. Cho. Work function tuning of metal/graphene stack electrode. *Applied Physics Letters*, 104(8):083512, 2014.

[177] R. Yang, S. Wu, D. Wang, G. Xie, M. Cheng, G. Wang, W. Yang, P. Chen, D. Shi, and G. Zhang. Fabrication of high-quality all-graphene devices with low contact resistances. *Nano Research*, 7(10):1449–1456, 2014.

[178] A. Di Bartolomeo, S. Santandrea, F. Giubileo, F. Romeo, M. Petrosino, R. Citro, P. Barbara, G. Lupina, T. Schroeder, and A. Rubino. Effect of back-gate on contact resistance and on channel conductance in graphene-based field-effect transistors. *Diamond and Related Materials*, 38:19–23, 2013.

[179] D. W. Yue, C. H. Ra, X. C. Liu, D. Y. Lee, and W. J. Yoo. Edge contacts of graphene formed by using a controlled plasma treatment. *Nanoscale*, 7:825–831, 2015.

[180] S. M. Song and B. J. Cho. Contact resistance in graphene channel transistors. *Carbon Letters*, 14(3):162–170, 2013.

[181] W. Li, C. A. Hacker, G. Cheng, Y. Liang, B. Tian, A. R. Hight Walker, C. A. Richter, D. J. Gundlach, X. Liang, and L. Peng. Highly reproducible and reliable metal/graphene contact by ultraviolet-ozone treatment. *Journal of Applied Physics*, 115(11):114304, 2014.

[182] W. Li, Y. Liang, D. Yu, L. Peng, K. P. Pernstich, T. Shen, A. R. Hight Walker, G. Cheng, C. A. Hacker, C. A. Richter, Q. Li, D. J. Gundlach, and X. Liang. Ultraviolet/ozone treatment to reduce metal-graphene contact resistance. *Applied Physics Letters*, 102(18), 2013.

[183] W. S. Leong, C. T. Nai, and J. T. L. Thong. What does annealing do to metal–graphene contacts? *Nano Letters*, 14(7):3840–3847, 2014.

[184] A. Hsu, H. Wang, K. K. Kim, J. Kong, and T. Palacios. Impact of graphene interface quality on contact resistance and RF device performance. *IEEE Electron Device Letters*, 32(8):1008–1010, 2011.

[185] A. Venugopal, L. Colombo, and E. M. Vogel. Contact resistance in few and multilayer graphene devices. *Applied Physics Letters*, 96(1):013512, 2010.

[186] B. Huang, M. Zhang, Y. Wang, and J. Woo. Contact resistance in top-gated graphene field-effect transistors. *Applied Physics Letters*, 99(3):032107, 2011.

[187] Y. Dan, Y. Lu, N. J. Kybert, Z. Luo, and A. T. Charlie Johnson. Intrinsic response of graphene vapor sensors. *Nano Letters*, 9(4):1472–1475, 2009.

[188] Z. Cheng, Q. Zhou, C. Wang, Q. Li, C. Wang, and Y. Fang. Toward intrinsic graphene surfaces: A systematic study on thermal annealing and wet-chemical treatment of sio$_2$-supported graphene devices. *Nano Letters*, 11(2):767–771, 2011.

[189] M. Ishigami, J. H. Chen, W. G. Cullen, M. S. Fuhrer, and E. D. Williams. Atomic structure of graphene on SiO_2. *Nano Letters*, 7(6):1643–1648, 2007.

[190] C. Casiraghi. Doping dependence of the Raman peaks intensity of graphene close to the Dirac point. *Phys. Rev. B*, 80:233407, 2009.

[191] A. Das, S. Pisana, B. Chakraborty, S. Piscanec, S.K. Saha, U.V. Waghmare, K.S. Novoselov, A.K. Geim, A.C. Ferrari, and A.K. Sood. Monitoring dopants by Raman scattering in an electrochemically top-gated graphene transistor. *Nature Nanotechnology*, 3:210–215, 2008.

[192] S. Pisana, M. Lazzeri, C. Casiraghi, K.S. Novoselov, A.K. Geim, A.C. Ferrari, and F. Mauri. Breakdown of the adiabatic bornoppenheimer approximation in graphene. *Nat. Mater.*, 6:198–201, 2007.

[193] A. C. Ferrari. Raman spectroscopy of graphene and graphite: Disorder, electron–phonon coupling, doping and nonadiabatic effects. *Solid State Communications*, 143(12):47–57, 2007.

[194] N. J. Lee, J. W. Yoo, Y. J. Choi, C. J. Kang, D. Y. Jeon, D. C. Kim, S. Seo, and H. J. Chung. The interlayer screening effect of graphene sheets investigated by Kelvin Probe Force Microscopy. *Applied Physics Letters*, 95(22):222107, 2009.

[195] J. A. Robinson, M. LaBella, M. Zhu, M. Hollander, R. Kasarda, Z. Hughes, K. Trumbull, R. Cavalero, and D. Snyder. Contacting graphene. *Applied Physics Letters*, 98(5):053103, 2011.

[196] K.S. Krishnan and N. Ganguli. Large anisotropy of the electrical conductivity of graphite. *Nature*, 144:667, 1939.

[197] W. Zhu, T. Low, V. Perebeinos, A. A. Bol, Y. Zhu, H. Yan, J. Tersoff, and P. Avouris. Structure and electronic transport in graphene wrinkles. *Nano Letters*, 12(7):3431–3436, 2012.

[198] V. E. Calado, G. F. Schneider, A. M. M. G. Theulings, C. Dekker, and L. M. K. Vandersypen. Formation and control of wrinkles in graphene by the wedging transfer method. *Applied Physics Letters*, 101(10):103116, 2012.

[199] Kontaktierung und elektrische Charakterisierung von funktionalisiertem Graphen mit unterschiedlichen C/O verhaeltnissen. *Master Project, University of Duisburg-Essen, Faculty of Engineering*, 2011.

List of Figures

List of Tables

List of symbols and abbreviations

α_0	Polarizability
ΔE_F	Fermi level shift
Δf	Frequency shift
Δz	Cantilever deflection
$\Delta\theta$	Phase shift
$\hat{a}_1, \hat{a}_2$	Basis vectors of the direct lattice
$\hat{a}_1^*, \hat{a}_2^*$	Basis vectors of the reciprocal lattice
$\hat{i}, \hat{j}, \hat{k}$	Unit vectors of the xyz-coordinate system
$\hbar$	Reduced Planck constant
μ	Charge carrier mobility
ν_0	Laser frequency
ν_m	Vibration/rotational frequency
$\overrightarrow{F}_{ts}^{min}$	Valley force at which $\vec{F}_{rep}$ begins to be relevant
$\vec{F}_{2\omega_{ac}}$	Spectral component of $\vec{F}_{el}$, sensitive to capacitance
$\vec{F}_{\omega_{ac}}$	Spectral component of $\vec{F}_{el}$, dependent of the CPD
$\vec{F}_{attr}$	Attractive forces
$\vec{F}_{dc}$	Spectral component of $\vec{F}_{el}$ which contributes to topography
$\vec{F}_{el}$	Electrostatic forces

$\vec{F}_{mag}$ Magnetic force

$\vec{F}_{rep}$ Repulsive forces

$\vec{F}_{ts}$ Tip-sample forces

$\partial\vec{F}_{el}/\partial z$ Electrostatic force gradient

ϕ Work function

ρ_c Contact resistivity

ρ_s Sheet resistivity

σ Conductivity

$\sigma_{rep}, \sigma_{attr}$ Proportional constants of the repulsive and attractive force

$\tilde{\nu}$ Wavenumber

$\tilde{f}_0$ Perturbed mechanical resonant frequency

$\tilde{k}_0$ Perturbed spring constant

Υ Hopping energy between inequivalent carbon atoms

ζ Substrate gate capacitance

A Cantilever′s amplitude

a Graphene interatomic distance

A_0 Cantilever′s free amplitude

A_d,A_s FGS drain and source contact area

A_{sp} Set point amplitude

A_T FGS channel total area

c Speed of light in vacuum

C_{gd}, C_{gs} Drain and source gate capacitance

d Tip-sample distance

e	Elementary charge
E_0	Electric field amplitude of the laser radiation
E_F	Fermi level
E_k	Electronic band structure energy
E_{vac}	Vacuum energy
f_0, ω_0	Mechanical resonant frequency, $\omega_0 = 2\pi f_0$
$f_0^{'}, \omega_0^{'}$	Piezoelectric dither frequency, $\omega_0^{'} = 2\pi f_0^{'}$
f_1, ω_1	Second mechanical resonant frequency, $\omega_1 = 2\pi f_1$
f_{ac}, ω_{ac}	AC modulation signal frequency, $\omega_{ac} = 2\pi f_{ac}$
f_{max}	Maximum frequency of oscillation
f_{Ref}	Reference frequency of the LIA
f_T	Cutoff frequency
g_{ds}	Drain conductance
g_m	Transconductance
h	FGS channel height
I_{ds}	Drain-source current
k	Spring constant
$K, K^{'}, \Gamma$	First-Brillouin zone points
k_{LIA}	Scaling factor of the LIA
k_x, k_y	Wave vectors of the reciprocal lattice
l	Channel′s device length
l_T	FGS total length
n	Charge carrier density

P Photon induced electric dipole moment

q Displacement of atoms during vibration/rotation

R_{2p} Two-terminal resistance

R_{4p} Four-terminal resistance

R_c Resistance at the contact

R_g Gate resistance

R_i Intrinsic resistance of the transistor

R_s Resistance at the channel

s_{Ref} Reference signal of the LIA

V_{ac} AC modulation signal amplitude

V_{CPD} Contact potential difference voltage

$V_{drop}(x)$ Voltage drop of a device at position x

V_{ds} Drain-source voltage

v_F Fermi velocity

V_{gs} Gate-source voltage

V_k Kelvin voltage

$V_k^{0V}(x)$ Kelvin voltage of a device without bias voltage at position x

$V_k^{ds}(x)$ Kelvin voltage of a device under bias voltage at position x

V_{sig} LIA output value (r.m.s) of the measured signal

w Channel′s device width

X, Y In-phase and quadrature outputs of the LIA

4p Four-point (probe method)

AFM Atomic Force Microscopy

AM- Amplitude Modulation

BLG Bi-Layer Graphene

C/O Carbon-to-Oxygen ratio

CCD Charge-Coupled Device

CPD Contact Potential Difference

CVD Chemical Vapor Deposition

FGS_x Functionalized Graphene Sheet of C/O = x

FLG Few Layers Graphene

FM- Frequency Modulation

GNR Graphene Nanoribbon

GO Graphene Oxide

HEMT High Electron-Mobility Transistor

KPFM Kelvin Probe Force Microscopy

LIA Lock-In Amplifier

MLG Multi Layer Graphene

PMMA Polymethyl methacrylate

QPD Quadrant Photo Diode

SLG Single Layer Graphene

TLM Transmission Line Method

Acknowledgments

Here I would like to acknowledge everyone involved in the realization of this Ph.D. thesis. First of all, I thank Prof. Dr. rer. nat. Gerd Bacher, head of the WET workgroup, along with the support of the Mexican government through the *Consejo Nacional de Ciencia y Tecnologia* (CONACyT), which allowed me to investigate along world renowned scientists in the exciting fields of Atomic Force Microscopy and Graphene. Thanks to this opportunity, not only I have collected scientific knowledge over the years, but a great deal of experience and good memories. I thank Prof. Dr. Thomas Schröder from Brandenburg university of technology Cottbus-Senftenberg and IHP Microelectronics, for his willingness to be the co-supervisor of this work.

Also my greatest gratitude to Dr.-Ing. Wolfgang Mertin who was with me in every step of the way even before the beginning of my Ph.D. studies. Always with its door open ready not only for the discussion of results but also to hear and help in any way possible. To everyone in the WET work group: colleagues with which I have cherish memories, specially in our annual meetings and Christmas parties, thank you guys for all the good times and talks. Our technicians and secretaries, the ones still active and the ones already enjoying their well deserved retirement, thank you for all your work and cooperation. Also to all students which came and go in the WET and share with us work and effort, specially to the students with which I had the opportunity to work with. Overcoming the learning curve at the beginning of every project is always a struggle, which was diminished with the help of Sasa Vinaji. As well, our partners from Princeton University and AMO GmbH from whom we receive exceptional and fascinating samples, which I had the opportunity to analyze. Also to my friends, the ones back home and those around the world you were and will be always on my mind wherever I go.

To Hanna and the Schäfer family which have given me a home here in Germany. And finally I would like to thank the love, support and patience of all my family through this five years, although separated by distance you were always close to me. *Apa, ama gracias por su apoyo y paciencia, gracias por todo, los amo.*

Erklärung

Hiermit versichere ich, dass ich die vorliegende Arbeit selbstständig verfasst und ohne unzulässige Hilfe Dritter und ohne Benutzung anderer als der angegebenen Hilfsmittel angefertigt habe. Die verwendeten Hilfsmittel und alle wörtlich oder inhaltlich übernommenen Stellen sind unter Angabe der Quelle gekennzeichnet.

Die Arbeit wurde bisher weder im Inland noch im Ausland in gleicher oder ähnlicher Form einer anderen Prüfungsbehörde vorgelegt.

Der Doktorgrad eines Doktors der Naturwissenschaften (Dr. rer. nat.) wird gemäß §1 Satz 2 der Promotionsordnung angestrebt.

Duisburg, den 28 Oktober 2016

Carlos Alvarado Chavarin